ELECTROKINETIC TRANSPORT, TRAPPING, AND SENSING IN INTEGRATED MICRO- AND NANOFLUIDIC DEVICES

Michelle L. Kovarik

Submitted to the faculty of the University Graduate School
in partial fulfillment of the requirements
for the degree
Doctor of Philosophy
in the Department of Chemistry
Indiana University
October 2009

Accepted by the Graduate Faculty, Indiana University, in partial fulfillment of the requirements for the degree of Doctor of Philosophy.

Doctoral Committee

_____
Stephen C. Jacobson, PhD.

_____
David E. Clemmer, PhD.

_____
Bogdan Dragnea, PhD.

_____
Amar H. Flood, PhD.

September 10, 2009

Dedicated to Sr. Mary Ethel Parrott and Sr. Judith Averbeck, SND,
who first introduced me to scientific research,

and to Prof. R. Scott Martin and Prof. Dana M. Spence,
who encouraged me to pursue it

ACKNOWLEDGMENTS.

I gratefully acknowledge the many people who have contributed to this work, foremost of which is my advisor, Prof. Stephen Jacobson. I appreciate both the guidance and the independence he has given me throughout the course of my graduate career. I also thank my committee members, Profs. Clemmer, Dragnea, and Flood, for their encouragement and assistance, and Prof. Lane Baker for his gift of tracked membranes and much useful advice concerning them.

I have been lucky to work with many talented scientists and professionals during my time here. I thank especially my co-workers and collaborators: Sam Sudhoff who worked on lithographic isolation of nanopores; Kaimeng Zhou who performed nanopore current studies and contributed to many insightful discussions; and Dr. Pam Bonner-Brown, Dr. Dave Kysela, Dr. Cecile Berne, and Prof. Yves V. Brun for their contributions to the bacterial chemotaxis and motility experiments, which would have been impossible without their expertise. I also thank Electronic Instrument Services, Mechanical Instrumentation Services, and the department glass shop, for all their help.

For their support and patient encouragement, I am grateful to my family, to my fellow group members, and to the many friends I've made here, especially Brigitte Robinson, Laura Sharon, Maggie Donoghue, and Jeremiah Marden.

Finally, I thank the funding sources which provided financial support for my studies. These include the Indiana University Women in Science Program, the National Science Foundation Graduate Research Fellowship Program, and Merck Research Laboratories. The work discussed here has been funded by various agencies, including Indiana University, the Indiana METACyt Initiative of IU, funded in part through a major grant from the Lilly Endowment, Inc., NSF CHE-0750295, and NSF CHE-0832651.

Michelle L. Kovarik

ELECTROKINETIC TRANSPORT, TRAPPING, AND SENSING IN INTEGRATED MICRO- AND NANOFLUIDIC DEVICES

Microfluidics is rapidly becoming a mature field, and improved fabrication methods now routinely produce sub-micrometer features. As device dimensions shrink, physical phenomena that are negligible at larger length scales become more important, and by integrating nanofluidic elements with microchannels, new analytical techniques can be developed based on the unique behavior of matter at the nanoscale. This work addresses the fabrication, operation, and application of in-plane nanochannels and out-of-plane nanopores in lab-on-a-chip devices.

In planar nanofluidic devices, we demonstrate a method to produce micro- and nanoscale features simultaneously with a single UV exposure step and evaluate flow control and sample dispensing with nanofluidic cross structures. Modification of the pinched injection method makes it applicable to variable-volume, attoliter-scale injections, including the smallest volume electrokinetically-controlled injections to date.

As an alternative approach, track-etch nanopore membranes are explored as out-of-plane nanofluidic components. The random distribution of pores in these membranes is overcome by lithographic and microchannel-based methods to isolate and address specific pores. Microfluidic isolation improves mass transport to the pore(s), provides easy coupling of electrical potentials, and facilitates additional sample processing steps up- and downstream.

These integrated microchannel-nanopore devices are used for diffusion-based dispensing, electrokinetic trapping, and resistive pulse sensing. In a high pore density device, diffusion-based dispensing establishes a stable chemical gradient for bacterial chemotaxis assays. For lower pore density devices, the nanopores are the most resistive components in the fluidic circuit, and application of an electric potential produces localized regions of high electric field strength and field gradient. These high field regions are applied to electrokinetic trapping of particles and cells in multiple-pore devices and to single particle detection by resistive pulse sensing in devices with a single isolated pore.

To better understand factors influencing ion current in single nanoscale conduits, we systematically examine ion current rectification as a function of pore diameter, ionic strength, and pH to improve understanding of ion current through nanopores and to characterize preferred operating parameters for sensing applications. These results are applied to detection of virus capsids, and future work is proposed to investigate capsid assembly.

Stephen C. Jacobson, PhD.	David E. Clemmer, PhD.
Bogdan Dragnea, PhD.	Amar H. Flood, PhD.

TABLE OF CONTENTS.

LIST OF FIGURES AND TABLES.

Chapter 2. Simultaneous fabrication of 3D micro- and nanoscale features.

Chapter 3. Nanofluidic circuits for attoliter-scale dispensing.

Chapter 4. Photolithographic isolation of single track-etch nanopores.

Chapter 5. A microchannel - nanopore device for bacterial chemotaxis assays.

Chapter 6. Electrokinetic trapping on integrated microchannel - multiple nanopore devices.

Chapter 7. Electrokinetic trapping and current-based sensing integrated microchannel - single nanopore devices.

CHAPTER 1. Applications of integrated micro- and nanofluidics.[1]

1.1. Introduction to nanofluidics.

Advances in microfabrication and miniaturized analysis technologies have resulted in increasingly sophisticated microfluidic systems, which are beginning to fulfill the promise of true "labs-on-a-chip" or "micro total analysis systems" by integrating multiple processing steps on a single device.[2] Furthermore, new and improved fabrication techniques have placed the nanoscale regime within reach, even for laboratories with limited fabrication facilities.[3] These advances are allowing scientists to explore fluidic systems containing ever-smaller conduits, with some approaching molecular length scales.

Incorporation of biological and synthetic nanoscale conduits in fluidic devices holds great promise for new analytical applications, as there are forces and phenomena at these length scales that are absent or negligible in larger microchannels.[4] Double layer overlap and the resulting ion permselectivity; localized enhancement of electric fields; and the increased influence of diffusion, surface-to-volume ratio, surface charge, and entropy are all critical considerations in designing these devices. The unique behavior of matter at the nanoscale will result in new applications as the area of nanofluidics receives greater attention. There are already a number of examples of how nanoscale components improve routine processing steps and add new functionality to microfluidic devices. The sections of this chapter represent the basic functions performed during chemical analysis: sample preparation, fluid handling and sample injection, separation, and detection, with the goal of demonstrating how nanofluidic components benefit each of these steps. This

chapter, along with the dissertation as a whole, focuses on devices containing one or more nanochannels or nanopores, typically defined as fluidic features with at least one dimension of 100 nm or less. Discrete features up to 0.5 μm are discussed here, as opposed to nanoporous monoliths[5] or membranes with tortuous paths.[6]

Some of the earliest work in nanofluidics used native and engineered protein pores in lipid bilayers to characterize a wide range of molecules, including polymers, nucleic acids, divalent metal ions, and organic molecules by resistive pulse sensing.[7] Protein pores provide excellent reproducibility with respect to their dimensions and internal chemistry combined with ease of preparation, since the pores self-insert into the bilayer from solution. However, lipid bilayers on-chip are relatively fragile and difficult to fabricate compared to the glass, polymer, and semiconductor substrates typical for microfluidic applications. As a result, many groups are pursuing emerging nanofabrication methods to produce nanopores and nanochannels in hard and soft materials. These nanoconduits are formed by a variety of methods, including track-etching polymer membranes,[8] sacrificial layer deposition,[9] electron beam lithography,[10] and etching photolithographically defined microchannels to nanometer-scale depths.[11] The variety of available fabrication methods results in flexible device design in which the chemistry and geometry of the nanoconduit are controllable, and nanofluidic elements are incorporated in either an in-plane or an out-of-plane fashion.

1.2. Sample preparation.

The goal of micro total analysis systems is to provide sample-in, answer-out capability. A critical and often challenging aspect of these systems is effective sample

preparation, which can include filtration, cell lysis, protein digestion, preconcentration, labeling, and other processing steps. Many of these steps, which are often performed off-chip, have been achieved by integrating nanoscale elements on microfluidic devices, leading to improved performance and increased automation.

The simplest sample preparation step is size-based filtration, which removes particulates from samples before their introduction on-chip. This step can be integrated on microfluidic devices, however, by incorporating track-etch nanopore membranes on the bottoms of reservoirs for on-chip filtration of samples and buffers. This technique eliminates channel clogging and reduces undesirable hydrodynamic flow from unbalanced fluid levels in the reservoirs.[12] On-chip filtration is also performed by sandwiching a track-etch membrane between two microchannels in a multilayer fluidic device. This technique is advantageous because either the filtrate, which passes through the membrane, or the retentate, which is retained in the microchannel, can be analyzed.[13] Both modes have been evaluated by placing a polycarbonate membrane containing 10 nm pores between two poly(dimethylsiloxane) channels. In one analysis, filtrate containing glutathione is separated from matrix interferents, such as proteins in plasma or red blood cell lysate, prior to detection. In a different application, the retentate, containing a PCR product, is concentrated at the membrane surface for subsequent analysis while smaller primer DNA strands are washed away.

The high surface-to-volume ratio of nanostructured materials is also useful for sample preconcentration. Insulin is selectively preconcentrated by microfluidic patterning of immobilized Fab on a track -etch nanopore membrane, followed by MALDI mass spectrometric analysis.[14] Although the actual concentration and detection steps of this

analysis are not performed on-chip, the use of microfluidic patterning of nanopore membranes could be scaled up to create arrays of immobilized antibodies for multiplexed sensing. In addition to antibodies, a wide range of chemical functionalities can be grafted onto track-etch polymer membranes and their inner pore surfaces for use in other preconcentration schemes, protein digestion, or labeling reactions.

Electrokinetic sample preconcentration is possible at the intersection of micro- and nanochannels due to unique ion transport phenomena in these regions.[5] Applying electric fields across these junctions causes unbalanced ion flux, or concentration polarization, across the nanochannel ultimately resulting in analyte concentration at the anodic and/or cathodic ends of the nanochannel. There are several reported examples of electrokinetically induced concentration polarization caused by double layer overlap. In this case, co-ions, which are typically anions since most device materials have a negative surface charge, are excluded from the nanochannel. The result is selective transport of cations through the nanochannel, resulting in preconcentration on the cathodic side from unbalanced cation flux.[15] Anions at the cathodic side are trapped at the entrance of the nanochannel due to electrostatic exclusion and concentrate with the cations to maintain local electroneutrality. An ion depletion region forms on the anodic side of the nanochannel, as cations are removed through the nanochannel and anions travel to the anode without being replaced. This depletion region leads to sample concentration near the anodic side of the nanochannel as well, due to stacking of analyte ions at the boundary of the depletion region.[16] This preconcentration effect has been applied to improve the dynamic range and sensitivity of a bead-based immunoassay.[17] Recent work in the Jacobson laboratory has demonstrated that concentration polarization also occurs in

the absence of double layer overlap.[8] In this case, ion depletion develops because a large proportion of the current through the nanopore is carried by counterions, resulting in their depletion on the anodic side. This illustrates that electrokinetic preconcentration can be performed on devices using larger pores or higher ionic strengths than would be possible if double layer overlap were required.

Electrophoretic and dielectrophoretic concentration of particles and cells is also possible using conical nanopores integrated on microfluidic devices, as discussed in Chapter 5.[18] Because nanoscale components are usually the most resistive elements on integrated devices, electric potentials dropped across nanopores or nanochannels result in high electric field strengths and field gradients from modest applied voltages. The resulting electrophoretic and dielectrophoretic forces are used to trap particles or cells at the small diameter opening of conical nanopores for concentration prior to analysis. These devices could be used for selective preconcentration of specific cell types based on their differing dielectrophoretic responses. Cell lysis may also be possible by harnessing the high local electric field strengths associated with nanoscale conduits.

1.3. Fluid handling: Sample injection, transport, and mixing.

Improved performance on microfluidic systems compared to traditional capillary separations is often attributed to decreased dispersion during sample injection due to channel interconnects with minimal dead volumes, and miniaturized devices have been applied to a number of problems which require precise fluid handling. Nanofluidic components will push this trend to even smaller volumes. While unique transport phenomena and diffusion in nanochannels present challenges to nanoscale fluid handling,

Chapter 3 discusses electrokinetic dispensing of volumes as small as ~50 aL,[19] and simple pressure gating has been used to pump, filter, and trap analytes in elastomeric nanochannels.[20]

Whereas single nanochannels are capable of manipulating and injecting ultra-small sample volumes, nanofluidic arrays, which have voltage-switchable gating, present an attractive injection scheme for microfluidic separations.[21] Injections are implemented on multilayer devices by sandwiching a nanopore membrane between two device layers, adding functionality without a significant increase in footprint. Separating device layers with track-etch nanopore membranes prevents uncontrolled mixing and facilitates voltage-gated injections between layers. Unbiased sample injection is performed using large pores, e.g., 200 nm diameter, while molecular weight-based filtration is combined with injection by using smaller pores, e.g., 15 nm diameter. Additionally, nanopore membranes have been used for post-separation valving to extract peaks of interest from the separation channel into another layer of the device for further analysis.[21]

Electrokinetic gating and transport control are also possible with nanofluidic transistors. These devices take advantage of electric fields from nearby electrodes, which are separated from the nanochannel by a thin dielectric layer. Electric fields from these electrodes penetrate the entire depth of a nanochannel, allowing gate electrodes positioned above the nanochannels to control ion transport in the device. For example, in a device with negative surface charge, application of a negative voltage enriches cations, which are the primary charge carriers, and increases conductance. A positive gate potential has the opposite effect. This has been used to control the concentration and transport of dyes,[22] DNA,[23] and the protein avidin[24] on nanofluidic devices. A pH- and

ionic strength-controlled transistor has also been recently demonstrated.[25] In this case, the effect of a gate electrode is produced by patterning the internal surface chemistry of an hourglass-shaped nanopore to control ion transport by changing the surface charge. This system could be incorporated in a multilayer microfluidic device for electrostatic, chemically-controlled gating.

Several examples of steric gating of nanochannels and pores are also reported. In these cases, the channel surface is modified with a macromolecular coating, e.g., DNA or polymer brushes, which controls transport through the nanoconduit. Some of these systems are voltage-gated, as in the case of conical nanopores modified with DNA, which offer controllable ion permselectivity.[26] When a positive potential is applied to the small diameter side of the conical pore, the DNA strands are drawn out of the pore, resulting in an "on" state. When the potential is reversed, DNA is drawn into the tip, blocking the pore and creating the "off" state. Similar steric gating is achievable through chemical switching as well. Nanoporous alumina membranes modified with adsorbed surfactants gate the transport of small molecules, such as methyl viologen and fluorescein,[27] and simulations suggest that polymer brushes can be used for steric gating as well, by using solvent composition to control the coil-to-globule transition of the polymer.[28] None of these steric-based systems is integrated on-chip to date, and the chemically-gated examples have limited temporal resolution compared to electrokinetic switching. However, for applications that require chemical rather than electrokinetic switches, they provide alternative gating mechanisms.

Nanofluidic components also provide electrically-controlled, pressure-driven fluid flow for applications which require fluid transport through field-free regions, e.g., for

efficient transport of cells without electroporation or lysis. When electroosmotic flow is directed from a microchannel through a nanoconduit, not all of the electroosmotically pumped fluid from the microchannel passes through the nanochannel to the cathode, due to the different electroosmotic flow properties of the nanochannel. The result is superambient or subambient pressure at the microchannel-nanochannel junction, inducing bulk fluid flow in the field-free region of the microchannel downstream of the nanoconduit, a phenomenon called electroosmotically induced hydraulic pumping.[29] This mechanism could be useful for portable devices because it generates pressure-driven flow without an external pump.

Some applications require not only solution transport, but controlled mixing or prevention of mixing of one or more liquid streams. While laminar flow in microchannels minimizes mixing, nanopore membranes or nanochannel arrays further reduce convective flow between the microchannels they connect due to the fourth power dependence of pressure driven flow on the lateral dimensions of the channel. This means that different solution compositions are maintained on opposite sides of a nanofluidic connection with only diffusive mixing, even with a substantial pressure difference between the two sides. This effect has been harnessed for diffusive sensing of calcium ions, bacterial cells, and enzyme activity.[30] For these applications, elimination of convective flow at each array intersection ensures that only solutions directly across the membrane from each other react, without substantial mass transfer across the membrane. Stable pH gradients between two device layers are obtained by combining this effect with double layer overlap.[31]

In contrast to the above examples, some applications, especially those involving on-chip reactions, require fast and efficient mixing of solutions on-chip. A well-defined three-dimensional nanochannel network fabricated within a microchannel provides efficient passive mixing.[32] This mixer performs well at higher fluid velocities and over shorter distances than previously reported random nanoporous mixers. Enhanced mixing is also observed for gated injections through nanopore membranes and has been used in a chip-based lead sensor.[33] Electrically actuated injection through a nanopore membrane has also been used to mix sample solution with an electrospray buffer prior to mass spectrometry, with the added benefit that the injected sample is partially desalted by injection through the nanopore membrane.[34] This work suggests that electrophoretic separation could be performed in one device layer, followed by quantitative transfer of an analyte plug across the membrane for mixing with electrospray buffer, ionization, and mass spectrometric analysis.

1.4. Separation.

Integrated micro- and nanofluidic devices are advancing the field of separations through improved performance of some traditional separations and by development of separation mechanisms based on entropy and other effects which dominate at the molecular length scale.[35] One of the earliest promises of micro- and nanofabrication was uniform, regular stationary phases for liquid separations to simplify device fabrication and minimize dispersion due to random packing.[36] More recently, there have been several examples of nanopillar arrays used for biomolecule separations based on Ogston sieving,

reptation, and entropic recoil.[37,38] Employing discrete nanochannels in separation systems offers several advantages as well.

Devices incorporating alternating deep (1.8 μm to 300 nm) and shallow (55 to 73 nm) regions elucidate and refine what have previously been considered gel-based separation mechanisms. In gels and nanofluidic devices, the characteristic length scale of the separation space approaches that of individual molecules, resulting in separation by entropic trapping or Ogston sieving.[39] In entropic trapping, long molecules, such as 5 to 160 kbp DNA, pass through the channel and are entropically trapped at the entrances to the shallow regions. Escape from the trap requires that a critical number of base pairs enters the nanoscale constriction, so that the rest of the molecule is pulled in and through to the next deep region. Because longer DNA molecules have a larger radius of gyration, they present a larger surface area to the entropic trap, increasing the probability that the requisite number of base pairs will enter the shallow region. The result is a higher mobility for larger DNA molecules, yielding an entropy-based separation.[40] For smaller analytes, such as short strands of DNA, the radius of gyration is smaller than the characteristic channel dimension, and Ogston sieving becomes the dominant separation mechanism. In this technique, the elution order is from smallest analyte to largest, with analyte mobility proportional to the fraction of the nanoscale constriction accessible to the molecule. This effect permits separation of SDS-protein complexes and short (50 - 766 bp) DNA strands.[41]

Both entropic trapping and Ogston sieving are observed in gel electrophoresis; however, in discrete nanofluidic devices, the separation matrix is precisely fabricated to pinpoint the transition between these two mechanisms. One example is a planar device

for continuous flow separation which has alternating rows of shallow and deep channels. The shallow nanoscale channels are blocked at regular intervals by solid pillars that support the device structure. The versatility of this device structure is evident from the number of separation schemes demonstrated, including entropic trapping separation of λ-DNA – Hind III digest, Ogston sieving of PCR markers, and separation of proteins by Ogston sieving at high ionic strength and by electrostatic sieving at low ionic strengths.[42] In this device, sample is introduced in the upper left corner, and electric fields are applied in both the x and y directions. Analytes with higher mobilities are more likely to jump across the shallow regions as they traverse the array, undergo greater deflection, and exit the array further to the right. The switch between entropic trapping and Ogston sieving is identified by examining the deflection angle as a function of DNA length. Deflection and mobility decrease with increasing strand length up to ~1 kbp, indicating an Ogston sieving mechanism. For ≥2 kbp, deflection and mobility increase with chain length, corresponding to the entropic trapping regime. This result demonstrates the ability of integrated micro- and nanoscale devices to perform gel-free separations of a wide range of biomolecule sizes simply by tuning device dimensions or ionic strength to adjust the separation mechanism.

In open channel chromatographic separations, mass transfer improves significantly with reduced channel dimensions due to the efficiency of diffusion over nanometer-scale distances. The major obstacle to nanoscale liquid chromatography is the enormous pressure drop required to produce optimum fluid velocities using traditional pressure-driven pumping. Shear-driven flows, however, provide high fluid velocities in nanoscale channels by means of a moving wall, which drags the bulk fluid in the nanochannel along

with it. Using shear-driven flow, dyes[43] and peptides[44] are chromatographically separated in less than 1 s in 120 nm deep nanochannels modified with C8, C12, and C18 coatings. To date, samples contained only two to four components, but nevertheless demonstrate potential for nanoscale liquid chromatography.

Some electrophoretic separations also benefit from reduced channel dimensions due to the effects of double layer overlap. Double layer overlap in nanochannels results in a parabolic, rather than plug-like, electroosmotic flow profile and a subsequent decrease in the radially averaged electroosmotic flow velocity.[45] This phenomenon is exploited to perform a nanochannel version of hydrodynamic chromatography, in which analytes are separated based on size, due to different sampling of the radially varying electroosmotic flow. Using 320 nm deep channels and 0.2 mM background electrolyte, 100 bp and 1000 bp dsDNA are resolved under free solution conditions. In this separation the larger DNA strand elutes first because the smaller DNA strand, with its smaller radius of gyration, can more closely approach the lower velocity region near the channel walls, reducing its average velocity.[46] The same effect resolves a DNA ladder ranging from 10 – 100 bp in a 100 nm channel at 1 mM buffer concentration.[47] The elution order is reversed at higher ionic strengths where double layer overlap is not present. Interestingly, a large-to-small elution order was observed for 1560 nm deep channels, which do not exhibit double layer overlap at any of the background electrolyte concentrations tested. This elution order is attributed to additional negative charge from the fluorescein-5-isothiocyanate label, which contributes more to the charge-to-hydrodynamic drag ratio of short DNA strands than to longer strands. These results indicate that in nanoscale separation systems the

effects of double layer overlap and ionic strength require careful consideration and present additional variables that can be tuned to improve resolution.

Double layer overlap and the resulting parabolic flow allow ion separations based on valence. In an array of high aspect ratio nanochannels, anionic Alexa 488 elutes before neutral Rhodamine B because Alexa 488 is repelled from the negatively charged nanochannel walls and is preferentially confined to the faster flow rate in the center of the nanochannels.[48] Rhodamine B is expected to sample all radial velocities evenly, as well as to experience some adsorption to the nanochannel walls. The elution order is reversed when the separation is performed in a microchannel. Carboxyl fluorescein (-2) and BODIPY (-1) separate similarly in a single nanochannel.[49] In this case, the elution order is the same for a 40 nm deep channel and a 2 μm deep channel; however, the distance between bands decreases in the nanochannel due to the increased average velocity of carboxyl fluorescein, which spends more time in the faster moving flow in the center of the nanochannel than BODIPY does. The valence and mobility of each analyte are calculated by comparing the analyte velocity in each channel.

1.5. Detection.

For some detection methods, such as absorbance, the decreased pathlengths and sample volumes analyzed in micro- and nanofluidics are problematic. Other methods, such as electrochemistry and fluorescence, scale well with decreasing device dimensions, and in many cases, reduced detection volumes even improve sensitivity. For example, the efficiency of diffusive transport in nanochannels makes them ideal for redox cycling because the oxidation product rapidly diffuses across the nanochannel depth to the

opposite electrode for reduction.[50] Another potential advantage in nanofluidic systems is that the detection volume approaches the scale of individual molecules. As a result, integrated micro- and nanofluidic systems are ideally suited for applications that require single molecule detection. The limited volume of a nanoconduit makes it appropriate for single molecule fluorescence studies at biologically relevant concentrations and for resistive pulse sensing.

When fluorescent molecules are confined in nanochannels, the detection volume is limited so that individual molecules are observed from a bulk solution of relatively high concentration. Nanochannels with 500 nm by 500 nm cross-sections have been used to detect individual quantum dot conjugates,[51] and even smaller channels have been used to perform both single molecule detection and fluorescence correlation spectroscopy of Alexa Fluor 488-5-dUTP.[52] Compared to a traditional open solution measurement, the signal-to-noise ratio in the nanochannel device nearly doubles as a result of reduced Raman scattering from solvent molecules and from consistent excitation of analyte molecules, which are confined by the channel walls to the center of the illumination. An improved signal-to-noise ratio, combined with the ability to use a pseudo-one-dimensional model, means that shorter analysis times are required to perform autocorrelation in the nanochannel device. An additional advantage is that every molecule passing through the detection volume contributes to the analysis. This capability, combined with extremely low volumetric flow rates, means that these devices are ideal for analyzing small volume samples. Single fluorescent molecules have also been detected as they transit an opaque aluminum/silicon nitride membrane as the opacity of the membrane eliminates background fluorescence from the sample above the

membrane.[53] Nanopores such as these could be incorporated into multilayer microfluidic devices for on-chip detection.

Because single molecule measurements examine each analyte molecule individually, nanofluidic detection elements sometimes eliminate or relax the demand for physical separation of sample components prior to detection. A 1 μm wide, 270 nm deep nanochannel has been used to observe photon bursts from individual stained DNA fragments.[54] Because the intensity of the photon burst is proportional to the length of the DNA fragment, histograms of the single molecule data reconstruct the size distribution of a DNA ladder without the need for separation. Additionally, the frequency of each burst size provides the relative concentration of each fragment. Restriction mapping of DNA is also performed without separating the resulting fragments.[55] In this case, single λ-phage DNA molecules are confined in 100-200 nm diameter channels, and reactions with three different restriction enzymes are recorded in real time. The lengths of the resulting fragments are determined by fitting the fluorescence intensity data after the fragments have diffused apart. Single molecule mobility measurements, demonstrated in submicron channels using nucleic acid fluorescent labels, present a similar possibility of extracting information typically obtained from an electrophoretic separation without the need for physical separation of sample components.[56]

Nanopores and channels are also used for on-chip resistive pulse sensing, a single molecule detection method which measures the change in current when a particle enters an aperture connecting two conducting solutions.[7] The most commonly known example is Coulter counting, but all applications rely on the basic principle that if a particle displaces a sufficient fraction of electrolyte solution, a measurable change in the pore

resistance and a corresponding change in current are produced. With a sufficiently small aperture, single porphyrin molecules are detectable,[57] and nanopore resistive pulse sensing has been suggested as a next generation DNA sequencing technique.[58] As mentioned above, protein pores were among the first nanoconduits used for resistive pulse sensing,[7] and although fabrication is challenging, lipid bilayers with protein pores can be integrated in microfluidic devices. This has been accomplished by using external pressure to thin a lipid solution down to a bilayer,[59] exploiting the material properties of poly(dimethylsiloxane) to extract excess solvent,[60] and painting a lipid solution onto an aperture through an access hole in the device.[61] The latter device has been used to sense the interaction of polyethylene glycol chains with an α-hemolysin protein channel.

Due to the technical difficulty of fabricating robust protein pore sensors on-chip, devices incorporating artificial nanochannels have also been developed. A quartz nanochannel, 400 nm in depth, has been used to detect colloid particles as small as 87 nm,[10] and a similar poly(dimethylsiloxane) device has been used to detect λ-phage DNA[62] and 510 nm streptavidin modified particles.[63] In the latter device, both an inhibition and a sandwich immunoassay are demonstrated, and diameter changes as small as 1.6 nm are detectable.

Related detection methods which rely on changes in nanochannel conductance have also been developed. Using a nanogap detector inside a nanofluidic channel, a 1.1 kbp DNA strand is linearized and detected as it passes between two 45 nm wide, 18 nm thick metal nanowire electrodes.[64] Linearization of the DNA inside the nanochannel minimizes noise from random motion of the DNA strand outside the sensing element. Another detection method is based on the change in conductance caused by multiple analyte

molecules binding to nanochannel walls. Streptavidin binding to a biotinylated nanochannel surface is detectable using either passive[9] or electrokinetic[65] analyte transport. Because streptavidin is negatively charged, binding actually increases the nanochannel conductance, and in general for these techniques, the output signal depends on both analyte size and charge. Additionally, sophisticated current-based sensing applications have been demonstrated using single nanopores bathed in bulk solution,[66] and multiple pores can be used simultaneously to increase sensitivity without significantly increasing signal complexity.[67] Integration of these sensors with microchannel architectures will allow label-free single molecule detection to be combined with the precise fluid handling and highly efficient separations possible on microfluidic devices. Preliminary efforts to integrate individual nanopores in microfluidic devices for single molecule and particle sensing are outlined in Chapter 7.

1.6. Outlook.

The properties of nanofluidic channels translate into unique technologies for integrated micro- and nanofluidic devices. Nanoscale elements can be applied to a wide range of analytical tasks, from sample preparation to detection. The appropriate choice of nanofluidic components depends on the volume and properties of the sample to be analyzed, including analyte size, charge, and hydrophobicity, in addition to the information to be obtained from the sample. At present most applications involving integrated micro- and nanofluidic devices are developed in laboratories which also specialize in fundamental studies of nanofluidics. This is to be expected as many phenomena related to nanofluidics are as yet not completely understood, and successful

application of nanofluidic devices requires careful consideration of multiple interconnected variables, including device dimensions, double layer thickness, ionic strength, and surface properties. We expect that this technology, like microfluidics before it, will soon become accessible to non-specialists, perhaps starting with polymer nanopore membranes, which can be purchased with the nanofluidic elements pre-fabricated. As a deeper understanding of the relevant effects is obtained, new and more sophisticated applications for nanochannels in micro total analysis systems will be possible. This dissertation reflects the fact that at present this field is an exciting mix of fundamental investigations and preliminary applications.

1.7. References.

1. This chapter reproduced in part with permission from Kovarik, M. L. and Jacobson, S. C. Nanofluidics in lab-on-a-chip devices. *Anal. Chem.* **2009**, *81*, 7133-7140. Copyright 2009 American Chemical Society.
2. West, J., Becker, M., Tombring, S. & Manz, A. Micro Total Analysis Systems: Latest Achievements. *Anal. Chem.* **2008**, *80*, 4403-4419.
3. Gates, B. D., Xu, Q., Stewart, M., Ryan, D., Willson, C. G. & Whitesides, G. M. New approaches to nanofabrication: molding, printing, and other techniques. *Chem. Rev.* **2005**, *105*, 1171-1196.
4. Schoch, R. B., Han, J. & Renaud, P. Transport phenomena in nanofluidics. *Rev. Mod. Phys.* **2008**, *80*, 839-883.
5. Höltzel, A. & Tallarek, U. Ionic conductance of nanopores in microscale analysis systems: Where microfluidics meets nanofluidics. *J. Sep. Sci.* **2007**, *30*, 1398-1419.
6. de Jong, J., Lammertink, R. G. H. & Wessling, M. Membranes and microfluidics: a review. *Lab Chip* **2006**, *6*, 1125-1139.
7. Bayley, H. & Cremer, P. S. Stochastic sensors inspired by biology. *Nature* **2001**, *413*, 226-230.
8. Zhou, K., Kovarik, M. L. & Jacobson, S. C. Surface-charge-induced ion depletion and sample stacking near single nanopores in microfluidic devices. *J. Am. Chem. Soc.* **2008**, *130*, 8614-8616.
9. Karnik, R., Castelino, K., Fan, R., Yang, P. & Majumdar, A. Effects of biological reactions and modifications on conductance of nanofluidic channels. *Nano. Lett.* **2005**, *5*, 1638-1642.

10. Saleh, O. A. & Sohn, L. L. Quantitative sensing of nanocolloids using a microchip Coulter counter. *Rev. Sci. Instr.* **2001**, *72*, 4449-4451.
11. Han, J. & Craighead, H. G. Entropic trapping and sieving of long DNA molecules in a nanofluidic channel. *J. Vac. Sci. Technol. A* **1999**, *17*, 2142-2147.
12. Noblitt, S. D., Kraly, J. R., VanBuren, J. M., Hering, S. V., Collett, J., J.L. & Henry, C. S. Integrated membrane filters for minimizing hydrodynamic flow and filtering in microfluidic devices. *Anal. Chem.* **2007**, *79*, 6249-6254.
13. Long, Z., Liu, D., Ye, N., Qin, J. & Lin, B. Integration of nanoporous membranes for sample filtration/preconcentration in microchip electrophoresis. *Electrophoresis* **2006**, *27*, 4927-4934.
14. Kim, B. Y., Swearingen, C. B., Ho, J.-a. A., Romanova, E. V., Bohn, P. W. & Sweedler, J. V. Direct immobilization of Fab' in nanocapillaries for manipulating mass-limited samples. *J. Am. Chem. Soc.* **2007**, *129*, 7620-7626.
15. Pu, Q., Yun, J., Temkin, H. & Liu, S. Ion-enrichment and ion-depletion effect of nanochannel structures. *Nano. Lett.* **2004**, *4*, 1099-1103.
16. Wang, Y.-C., Stevens, A. L. & Han, J. Million-fold preconcentration of proteins and peptides by nanofluidic filter. *Anal. Chem.* **2005**, *77*, 4293-4299.
17. Wang, Y.-C. & Han, J. Pre-binding dynamic range and sensitivity enhancement for immuno-sensors using nanofluidic preconcentrator. *Lab Chip* **2008**, *8*, 392-394.
18. Kovarik, M. L. & Jacobson, S. C. Integrated nanopore/microchannel devices for ac electrokinetic trapping of particles. *Anal. Chem.* **2008**, *80*, 657-664.
19. Kovarik, M. L. & Jacobson, S. C. Attoliter-scale dispensing in nanofluidic channels. *Anal. Chem.* **2007**, *79*, 1655-1660.
20. Huh, D., Mills, K. L., Zhu, X., Burns, M. A., Thouless, M. D. & Takayama, S. Tuneable elastomeric nanochannels for nanofluidic manipulation. *Nat. Mater.* **2007**, *6*, 424-428.
21. Kuo, T.-C., Cannon, D. M. J., Chen, Y., Tulock, J. J., Shannon, M. A., Sweedler, J. V. & Bohn, P. W. Gateable nanofluidic interconnects for multilayered microfluidic separation systems. *Anal. Chem.* **2003**, *75*, 1861-1867.
22. Oh, Y.-J., Gamble, T. C., Leonhardt, D., Chung, C.-H., Brueck, S. R. J., Ivory, C. F., Lopez, G. P., Petsev, D. N. & Han, S. M. Monitoring FET flow control and wall adsorption of charged fluorescent dye molecules in nanochannels integrated into a multiple internal reflection infrared waveguide. *Lab Chip* **2008**, *8*, 251-258.
23. Karnik, R., Fan, R., Yue, M., Li, D., Yang, P. & Majumdar, A. Electrostatic control of ions and molecules in nanofluidic transistors. *Nano. Lett.* **2005**, *5*, 943-948.
24. Karnik, R., Castelino, K. & Majumdar, A. Field-effect control of protein transport in a nanofluidic transistor circuit. *Appl. Phys. Lett.* **2006**, *88*, 123114.
25. Kalman, E. B., Vlassiouk, I. & Siwy, Z. Nanofluidic bipolar transistors. *Adv. Mater.* **2008**, *20*, 293-297.
26. Harrell, C. C., Kohli, P., Siwy, Z. & Martin, C. R. DNA-nanotube artificial ion channels. *J. Am. Chem. Soc.* **2004**, *126*, 15646-15647.
27. Schmuhl, R., van den Berg, A., Blank, D. H. A. & ten Elshof, J. E. Surfactant-modulated switching of molecular transport in nanometer-sized pores of membrane gates. *Angew. Chem. Int. Ed.* **2006**, *45*, 3341-3345.

28. Huang, J. L., Wang, Y. & Laradji, M. Flow control by smart nanofluidic channels: a dissipative particle dynamics simulation. *Macromolecules* **2006**, *39*, 5546-5554.
29. Alarie, J. P.; et al. In *Micro Total Analysis Systems 2001*, Proceedings of the 5th International Conference on Micro Total Analysis Systems, Monterey, CA, Oct 21−25, 2001; Ramsey, J. M. and van den Berg, A., Eds.; Kluwer Academic Publishers: Dordrecht, The Netherlands, 2001; 131− 132.
30. Ismagilov, R. F., Ng, J. M. K., Kenis, P. J. A. & Whitesides, G. M. Microfluidic arrays of fluid-fluid diffusional contacts as detection elements and combinatorial tools. *Anal. Chem.* **2001**, *73*, 5207-5213.
31. Fa, K., Tulock, J. J., Sweedler, J. V. & Bohn, P. W. Profiling pH gradients across nanocapillary array membranes connecting microfluidic channels. *J. Am. Chem. Soc.* **2005**, *127*, 13928-13933.
32. Jeon, S., Malyarchuk, V., White, J. O. & Rogers, J. A. Optically fabricated three dimensional nanofluidic mixers for microfluidic devices. *Nano. Lett.* **2005**, *5*, 1351-1356.
33. Chang, I.-H., Tulock, J. J., Liu, J., Kim, W.-S., Cannon, D. M. J., Lu, Y., Bohn, P. W., Sweedler, J. V. & Cropek, D. M. Miniaturized lead sensor based on lead-specific DNAzyme in a nanocapillary interconnected microfluidic device. *Environ. Sci. Technol.* **2005**, *39*, 3756-3761.
34. Iannacone, J. M., Jakubowski, J. A., Bohn, P. W. & Sweedler, J. V. A multilayer poly(dimethylsiloxane) electrospray ionization emitter for sample injection and online mass spectrometric detection. *Electrophoresis* **2005**, *26*, 4684-4690.
35. Eijkel, J. C. T. & van den Berg, A. The promise of nanotechnology for separation devices - from a top-down approach to nature-inspired separation devices. *Electrophoresis* **2006**, *27*, 677-685.
36. He, B., Tait, N. & Regnier, F. Fabrication of nanocolumns for liquid chromatography. *Anal. Chem.* **1998**, *70*, 3790-3797.
37. Cabodi, M., Turner, S. W. P. & Craighead, H. G. Entropic recoil separation of long DNA molecules. *Anal. Chem.* **2002**, *74*, 5169-5174.
38. Kaji, N., Tezuka, Y., Takamura, Y., Ueda, M., Nishimoto, T., Nakanishi, H., Horiike, Y. & Baba, Y. Separation of long DNA molecules by quartz nanopillar chips under a direct current electric field. *Anal. Chem.* **2004**, *76*, 15-22.
39. Viovy, J.-L. Electrophoresis of DNA and other polyelectrolytes: Physical mechanisms. *Rev. Mod. Phys.* **2000**, *72*, 813-872.
40. Han, J. & Craighead, H. G. Separation of long DNA molecules in a microfabricated entropic trap array. *Science* **2000**, *288*, 1026-1029.
41. Fu, J., Mao, P. & Han, J. Nanofilter array chip for fast gel-free biomolecule separation. *Appl. Phys. Lett.* **2005**, *87*, 263902.
42. Fu, J., Schoch, R. B., Stevens, A. L., Tannenbaum, S. R. & Han, J. A patterned anisotropic nanofluidic sieving structure for continuous-flow separation of DNA and proteins. *Nat. Nanotechnol.* **2007**, *2*, 121-128.
43. Clicq, D., Vervoort, N., Vounckx, R., Ottevaere, H., Buijs, J., Gooiijer, C., Ariese, F., Baron, G. V. & Desmet, G. Sub-second liquid chromatographic separations by means of shear-driven chromatography. *J. Chrom. A* **2002**, *979*, 33-42.

44. Vankrunkelsven, S., Clicq, D., Cabooter, D., De Malsche, W., Gardeniers, J. G. E. & Desmet, G. Ultra-rapid separation of an angiotensin mixture in nanochannels using shear-driven chromatography. *J. Chrom. A* **2006**, *1102*, 96-103.
45. Rice, C. L. & Whitehead, R. Electrokinetic flow in a narrow cylindrical capillary. *J. Phys. Chem.* **1965**, *69*, 4017-4024.
46. Ramsey, J. M.; et al. In *Micro Total Analysis Systems 2002*, Proceedings of the 6th International Conference on Micro Total Analysis Systems, Nara, Japan, Nov 3−7, 2002; Baba, Y., Eds.; Kluwer Academic Publishers: Dordrecht, The Netherlands, 2002; Vol. 1, 314− 316.
47. Pennathur, S., Baldessari, F., Santiago, J. G., Kattah, M. G., Steinman, J. B. & Utz, P. J. Free-solution oligonucleotide separation in nanoscale channels. *Anal. Chem.* **2007**, *79*, 8316-8322.
48. Garcia, A. L., Ista, L. K., Petsev, D. N., O'Brien, M. J., Bisong, P., Mammoli, A. A., Brueck, S. R. J. & Lopez, G. P. Electrokinetic molecular separation in nanoscale fluidic channels. *Lab Chip* **2005**, *5*, 1271-1276.
49. Pennathur, S. & Santiago, J. G. Electrokinetic transport in nanochannels. 2. Experiments. *Anal. Chem.* **2005**, *77*, 6782-6789.
50. Wolfrum, B., Zevenbergen, M. & Lemay, S. Nanofluidic redox cycling amplification for the selective detection of catechol. *Anal. Chem.* **2008**, *80*, 972-977.
51. Stavis, S. M., Edel, J. B., Samiee, K. T. & Craighead, H. G. Single molecule studies of quantum dot conjugates in a submicrometer fluidic channel. *Lab Chip* **2005**, *5*, 337-343.
52. Foquet, M., Korlach, J., Zipfel, W., Webb, W. W. & Craighead, H. G. Focal volume confinement by submicrometer-sized fluidic channels. *Anal. Chem.* **2004**, *76*, 1618-1626.
53. Chansin, G. A. T., Mulero, R., Hong, J., Kim, M. J., deMello, A. J. & Edel, J. B. Single-molecule spectroscopy using nanoporous membranes. *Nano. Lett.* **2007**, *7*, 2901-2906.
54. Foquet, M., Korlach, J., Zipfel, W., Webb, W. W. & Craighead, H. G. DNA fragment sizing by single molecule detection in submicrometer-sized closed fluidic channels. *Anal. Chem.* **2002**, *74*, 1415-1422.
55. Riehn, R., Lu, M., Wang, Y.-M., Lim, S. F., Cox, E. C. & Austin, R. H. Restriction mapping in nanofluidic devices. *Proc. Natl. Acad. Sci.* **2005**, *102*, 10012-10016.
56. Stavis, S. M., Edel, J. B., Li, Y., Samiee, K. T., Luo, D. & Craighead, H. G. Single-molecule mobility and spectral measurements in submicrometer fluidic channels. *J. Appl. Phys.* **2005**, *98*, 044903.
57. Heins, E. A., Sizy, Z. S., Baker, L. A. & Martin, C. R. Detecting single porphyrin molecules in a conically shaped synthetic nanopore. *Nano. Lett.* **2005**, *5*, 1824-1829.
58. Mukhopadhyay, R. DNA sequencers: the next generation. *Anal. Chem.* **2009**, *81*, 1736-1740.
59. Suzuki, H., Tabata, K. V., Noji, H. & Takeuchi, S. Highly reproducible method of planar lipid bilayer reconstitution in polymethyl methacrylate microfluidic chip. *Langmuir* **2006**, *22*, 1937-1942.

60. Malmstadt, N., Nash, M. A., Purnell, R. F. & Schmidt, J. J. Automated formation of lipid-bilayer membranes in a microfluidic device. *Nano. Lett.* **2006**, *6,* 1961-1965.
61. Hromada, L. P., Nablo, B. J., Kasianowicz, J. J., Gaitan, M. A. & DeVoe, D. L. Single molecule measurements within individual membrane-bound ion channels using a polymer-based bilayer lipid membrane chip. *Lab Chip* **2008**, *8,* 602-608.
62. Saleh, O. A. & Sohn, L. L. An artificial nanopore for molecular sensing. *Nano. Lett.* **2003**, *3,* 37-38.
63. Saleh, O. A. & Sohn, L. L. Direct detection of antibody-antigen binding using an on-chip artificial pore. *Proc. Natl. Acad. Sci.* **2003**, *100,* 820-824.
64. Liang, X. & Chou, S. Y. Nanogap detector inside nanofluidic channel for fast real-time label-free DNA analysis. *Nano. Lett.* **2008**, *8,* 1472-1476.
65. Schoch, R. B., Cheow, L. F. & Han, J. Electrical detection of fast reaction kinetics in nanochannels with an induced flow. *Nano. Lett.* **2007**, *7,* 3895-3900.
66. Gyurcsanyi, R. E. Chemically-modified nanopores. *TrAC* **2008**, *27,* 627-639.
67. Ervin, E. N., White, R. J. & White, H. S. Sensitivity and signal complexity as a function of the number of ion channels in a stochastic sensor. *Anal. Chem.* **2009**, *81,* 533-537.

CHAPTER 2. Simultaneous fabrication of 3D micro- and nanoscale features.[1]

2.1. Introduction to 3D fabrication and nanofabrication techniques.

Integrated micro- and nanofluidic devices require fabrication of features that span a wide size range. Techniques which produce three-dimensional features are of interest because they allow seamless coupling of fluidic connections of varying scale. Standard lithographic techniques can produce multilevel features; however, multiple layers of photoresist are required, and each layer must be processed individually to create structures with three-dimensional (3D) topography.[2] Alternative methods usually rely on a special photomask or exposure technique. For example, grayscale lithography uses photomasks with variable optical density to produce 3D features in a single layer of positive tone resist. This technique is effective for positive tone resists because the photosensitive layer is exposed from the top down to the substrate surface. Application to negative tone resists has been more limited because of the requirement that the resist be exposed at the substrate surface for adhesion. This condition can be met by applying the photoresist directly to the mask surface and exposing the layer through a grayscale substrate.[3] However, this method necessitates the consumption of an expensive grayscale mask as the substrate.

Techniques such as electron beam (e-beam) lithography,[4] two-photon lithography,[5] and focused ion beam (FIB) milling[6] can directly write 3D structures. Varying exposure during e-beam patterning in a negative tone resist yields 3D structures, with lower doses resulting in smaller features. Similarly, two-photon lithography produces high resolution, free-standing 3D structures by rastering a high energy, pulsed laser through a negative

tone resist layer. To form features in a variety of materials, not just resists, FIB milling can be used as a sculpting tool. All of these methods are scanning techniques which produce features serially. Consequently, they typically lack the high throughput advantage achievable by optical lithography, which can expose many patterns and large areas in parallel. An optical method for fabricating 3D microfluidic devices in a single lithographic step has been demonstrated where overexposure of a negative tone resist by diffracted light created features≥ 10 μm.[7] This technique allows multilevel features to be created in a single exposure with a UV flood source but cannot produce features with arbitrary spacing or extending over an entire range of heights in a single layer due to nonlinear response.

An alternative optical method for creating 3D structures stems from work in the Jacobson laboratory in which the chemically amplified negative tone resist SU-8[8] was used to map the light intensity transmitted through nanoapertures in metal films.[9] The surfaces of the polymer replicas represent the isointensity surfaces corresponding to the exposure threshold of the resist, and therefore, maps of the electromagnetic radiation at the surface are developed. Feature dimensions correlate to the aperture dimensions and exposure energy with small apertures and low exposures producing smaller features than large apertures and high exposures. Recently, this mapping technique has been extended to imaging two-photon processes in close proximity to bow-tie structures.[10] Similarly, plasmonic nanolithography has produced features with sub-diffraction limit resolution by taking advantage of plasmon-enhanced transmission through arrays of nanoapertures in a metal film.[11] All three methods use SU-8, which has several advantages for creating maps in close proximity to nanostructures. SU-8 exhibits a negligible change in its optical

properties (transmission and refractive index) during exposure, primarily because cross-linking of the resist occurs after exposure during the post-exposure bake. Also, polymeric features with large aspect ratios and high resolution can be formed. The minimum feature size (or resolution) appears to be limited by diffusion of the photocatalyst and is ~25 nm for standard resist processing.[12]

We have applied the resist mapping technique to create structures with micro- and nanoscale dimensions simultaneously. Two-dimensional photomasks with nano- and microscale aperture widths were coated with SU-8 which, in turn, was exposed to UV light through the mask, thermally processed, and developed. The 3D topography of the resulting polymer features corresponded to the photomask dimensions and exposure energy. Because photomasks can be designed with arbitrary patterns, nanoscale features were easily coupled to microscale features by creating them in the same photoresist layer with a single exposure.

2.2. Methods.

Photomask Fabrication. To produce the photomasks, soda-lime glass substrates coated with 120 nm chromium (Telic) were spin-coated (PWM32-PS-R790; Headway Research) with 200 nm of 950 kDa poly(methylmethacrylate) in anisole (PMMA; MicroChem Corp.). Mask patterns were drawn in Design CAD software (IMSI) and written by e-beam lithography (Nano Pattern Generation System; JC Nabity Lithography Systems) performed on a scanning electron microscope (SEM; LEO 1430; Carl Zeiss SMT). Figure 2-1a is a schematic illustrating the mask design, which was the same for all experiments. In the CAD software file, region 1 was defined as 5 μm wide, region 2 as 1

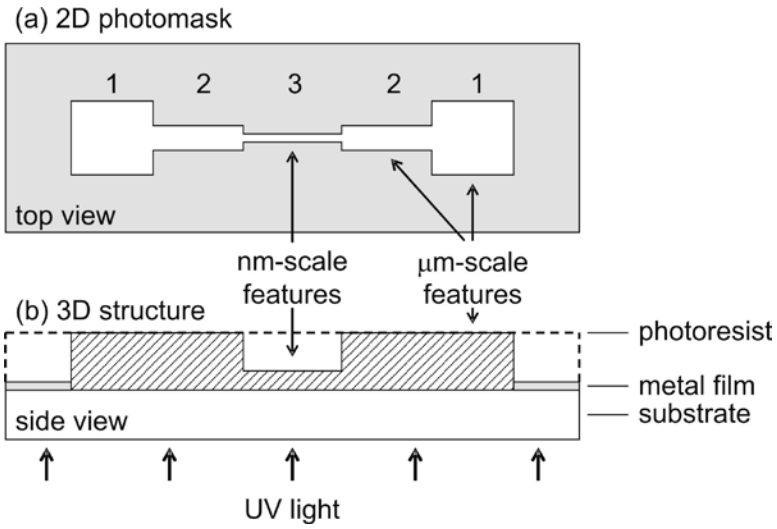

Figure 2-1. Schematics of (a) a two-dimensional photomask in a metal film and (b) cross-section through the center of the resulting micro- and nanoscale polymer feature following UV exposure and post-exposure processing. The dimensions of the features were controlled by the mask dimensions and exposure energy. The schematics are not to scale.

μm wide, and region 3 as a line produced by a single pass of the electron beam. Regions 1 and 2 were 20 μm long, and region 3 was 30 μm long. The widths in each region were varied by adjusting the exposure energy with typical exposures of 250-400 $\mu C/cm^2$ for regions 1 and 2 and 12-16 nC/cm for region 3. These exposures are given as the incident energy divided by the line spacing and by the center-to-center spacing of the dwell points for areas (regions 1 and 2, $\mu C/cm^2$) and the incident energy divided by the center-to-center spacing of the dwell points for lines (region 3, nC/cm). Total e-beam exposure time was 70-100 s per pattern, depending on exposure energy. Following exposure, samples were developed in a 3:1 mixture of isopropanol and methyl isobutyl ketone (MicroChem Corp.) for 2 min. The chromium film was then wet chemically etched with a 1:1 mixture of CE-8001-N and CE-8002-A chromium etchants (Transene) for 1 min. After etching was completed, the PMMA film was removed by sonicating the mask in acetone for 1 min.

Feature Polymerization. After preparing the mask, standard photolithography of SU-8, as described in Section A1, was used to produce the 3D features. Films (10.5 μm thick) of SU-8 2010 (MicroChem Corp.) were spin-coated directly onto the Cr masks, and after thermal processing substrates were placed SU-8 side down on the stage of a mask aligner/exposure system (205S; Optical Associates Inc.), and the SU-8 was exposed through the photomask and an additional 360 nm bandpass filter (45 nm bandwidth; Edmunds Industrial Optics). The exposure system was operated at 10 mW/cm^2 for 365 nm, and exposure energies of 100, 150, 200, and 400 mJ/cm^2 were evaluated. Processing was then completed according to standard protocols. The exposure process and resulting feature are illustrated in Figure 2-1b. Photomasks were reused several times by sonicating

the samples in Remover PG (MicroChem Corp.) for 10 min to remove polymerized features.

Scanning Electron Microscopy. Images of the photomasks and polymer features were taken using the SEM. Prior to imaging, the samples were sputter coated with 10 nm of gold (Polaron E5100; Quorum Technologies) to minimize charging of dielectrics. A 15 kV accelerating voltage and 50 pA probe current were used for imaging. Dimensions of the photomasks and polymer features were obtained from the images using the SEM software. For feature heights, images were obtained at an 81º tilt of the sample stage, and software tilt correction of -9º was used to account for the difference from 90º.

2.3. Results and discussion.

Figure 2-2a shows an SEM image of a photomask after e-beam lithography and wet chemical etching of the chromium film. Mask widths for each region were typically 5-5.5 μm for region 1, 0.8-1.3 μm for region 2, and 350-700 nm for region 3. By using a design with constant dimensions and varying the electron beam exposure, masks with a range of widths for each region, especially region 3, were fabricated. Because the e-beam patterns were transferred to the metal film by isotropic wet chemical etching, the minimum feature width was limited to twice the film thickness plus the initial linewidth written in the PMMA film by the electron beam. The narrowest e-beam linewidths were ~100 nm wide, resulting in apertures ~350 nm wide after etching. Anisotropic processes such as reactive ion etching could produce narrower features in the metal film, further decreasing the minimum feature size for this technique.

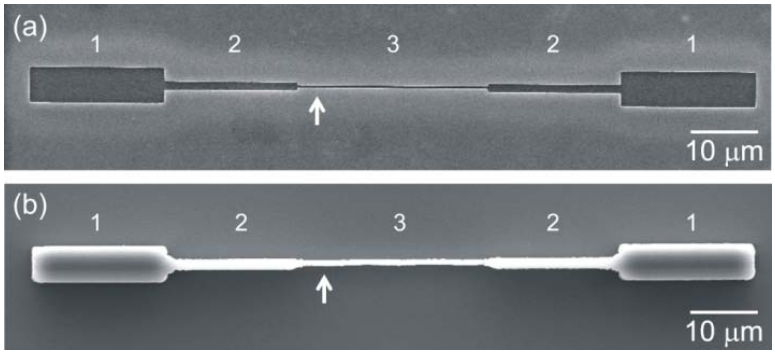

Figure 2-2. Scanning electron microscope (SEM) images of top views of (a) an etched photomask pattern and (b) the resulting polymerized SU-8 feature. In (a) the photomask widths were (1) 5.4 µm, (2) 1.2 µm, and (3) 370 nm. In (b) the SU-8 feature widths at the top were (1) 5.5 µm, (2) 1.6 µm, and (3) 680 nm. Regions 1 and 2 were 20 µm long, and region 3 was 30 µm long. The arrows denote the areas shown in Figure 2-5.

During photomask fabrication, several etchants were evaluated to determine the best etch conditions. A mixture of equal parts CE-8002-A and CE-8001-N etchants (Transene) provided a good combination of controlled etch rate, surface wetting, and minimal photoresist blistering. Both CE-8002-A and CE-8001-N etch slowly with respective rates of 15-20 Å/s and 22-25 Å/s, and the 1:1 mixture of the two etchants etched at a similar rate of ~22 Å/s. CE-8002-A is a ceric ammonium/acetic acid solution and contains a wetting agent to aid in etching fine features, such as region 3 in the mask design. Unfortunately, etching in 100% CE-8002-A etchant resulted in damage to the film in regions outside the intended mask design. Acetic acid is known to damage or remove PMMA films,[13] and these mask defects may have been due to blistering of the PMMA. This effect was reduced by mixing the CE-8002-A with CE-8001-N, which uses nitric acid instead of acetic acid but lacks the needed wetting agent.

Figure 2-2b shows the top view of a 3D photopolymerized SU-8 feature, and Figure 2-3a is an image of the same feature at a 65º tilt. The SU-8 feature was produced using an exposure of 150 mJ/cm^2 and showed 3D topography. Light transmission was limited by the narrow portion of the mask (region 3), resulting in the short central part of the feature. Wide apertures (regions 1 and 2) allowed the SU-8 to be polymerized completely through the resist layer, yielding taller features. The SU-8 features were 5.4 μm wide and 10.5 μm tall in region 1, 1.2 μm wide and 10.5 μm tall in region 2, and 370 nm wide and 3.3 μm tall in region 3. These widths were measured at the bottom of the features. At the top, the SU-8 features were slightly wider with widths of 5.5 μm, 1.6 μm, and 680 nm for regions 1, 2, and 3, respectively. This widening is likely due to diffraction of light off the rough mask edges during exposure. In regions 1 and 2, sidewall angles were estimated to be

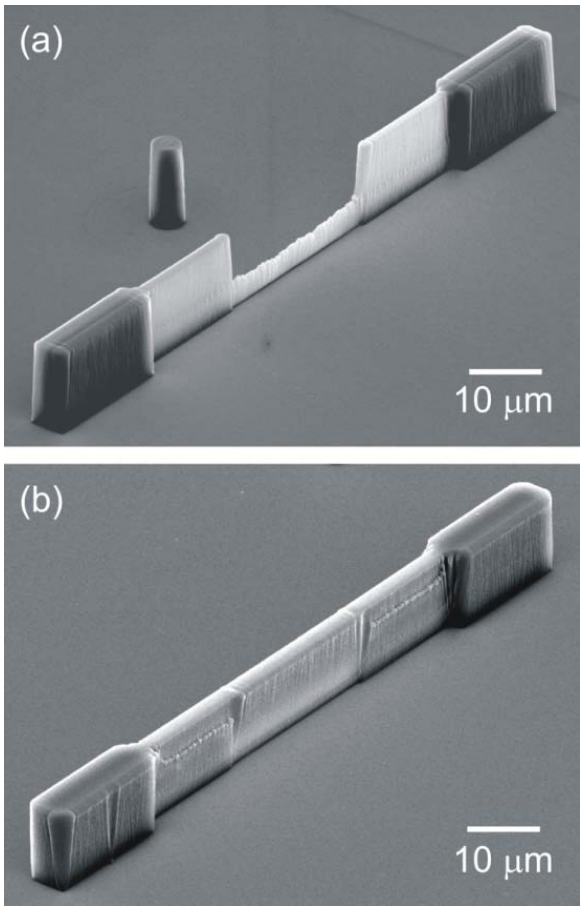

Figure 2-3. SEM images at a 65° tilt of features produced from (a) 150 mJ/cm ^{2} and (b) 400 mJ/cm^2 exposures. Region 3 was 370 nm wide in (a) and 490 nm wide in (b). Figures 2-2b and 2-3a show the same structure. The cylindrical feature in Figure 2-3a resulted from the e-beam resting at that location during the mask writing process.

between 89.7º and 87.3º, respectively, corresponding to an average aspect ratio of 40 for the sidewall. In addition to mask width, feature height was dependent on UV exposure energy. Figure 2-3b shows a feature produced from a similar mask with a width of 490 nm in region 3 and an exposure of 400 mJ/cm^2. The result was a high aspect ratio structure of uniform height (10.5 μm). By increasing the total exposure energy, even the SU-8 in the narrow region 3 received sufficient exposure to polymerize through the entire film thickness. The features seen in Figure 2-3 demonstrate the potential of this technique to produce features with 3D topography or structures with a high aspect ratio by simply changing the exposure.

Figure 2-4 further illustrates the dependence of feature height on exposure energy and shows the variation of feature height with photomask width for exposures of 100, 150, 200, and 400 mJ/cm^2. Thirty mask patterns with varying linewidths were fabricated, and measurements of the photomask widths and polymer feature heights were made in regions 2 and 3. The feature height increased with mask width until reaching the film thickness (~10.5 μm). For the highest exposure (400 mJ/cm^2), the entire pattern was exposed through the thickness of the resist layer (see Figure 2-3b). In this case, feature height was independent of mask width and equal to the film thickness for all but the narrowest line width. Several masks were used for multiple exposures by removing the polymerized features after analysis and repeating the polymerization step, and the repeatability of the feature height was less than 7% relative standard deviation.

In Figure 2-4, the increase in feature height with mask width can be approximated by a line having a slope of 20 for the 100 and 150 mJ/cm^2 exposures, i.e., a 2 μm increase in feature height for a 100 nm increase in mask width. The slope steepness helped explain

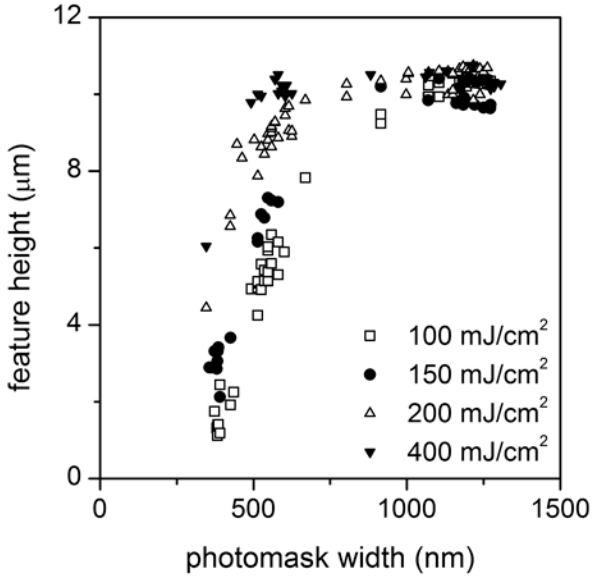

Figure 2-4. Variation of the feature height with photomask width for exposures of 100, 150, 200, and 400 mJ/cm^2. The photomask widths and polymer feature heights were obtained from SEM images. The heights were taken at 81º tilt of the sample stage and tilt corrected -9º to account for the difference from 90º.

the roughness seen at the top of region 3 of Figure 2-3a, where small variations in mask widths were translated into proportional differences in feature height. This effect was less apparent in the wider regions 1 and 2 where the roughness represented a smaller percentage of the mask width and the feature height was limited by the resist thickness. While any roughness should be minimized, the feature roughness observed demonstrated the sensitivity of this technique for mapping transmission intensity.

The roughness in the polymer features was further analyzed by evaluating the variation in the photomask width and comparing to the variation in the corresponding polymer feature height. In region 3 (see Figure 2-2), two photomask widths (380 and 570 nm) and two exposures (100 and 150 mJ/cm^2) were compared. Twenty-four measurements at 200 nm intervals were made along each photomask and polymer feature. Examples of images from which these measurements were taken are shown in Figure 2-5, and the results of the measurements are summarized in Table 2-1. On average, the variation in the feature height was approximately ten times larger than the variation in the mask width. Moreover, the relative standard deviations for the mask widths and polymer feature heights were comparable and both ranged from 2-3%. Again, these data demonstrated the ability of photoresist to map small variations in the photomask dimensions. A direct comparison of these values with the slopes determined in Figure 2-4, however, was not possible. The standard deviations for the photomask measurements approached the resolution of the SEM measurements (pixel size = 11 nm) and were overestimated as a result.

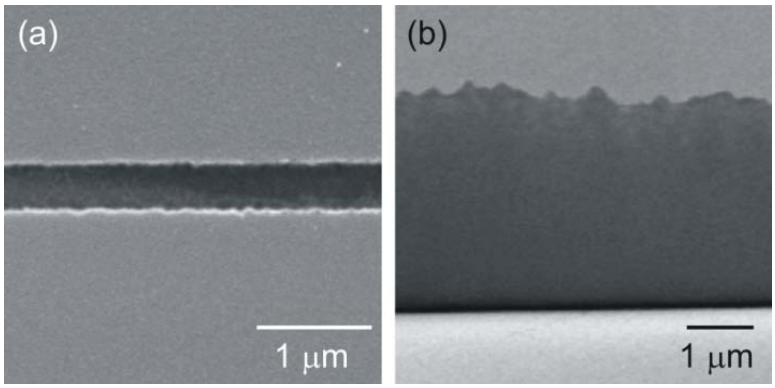

Figure 2-5. SEM images from region 3 showing (a) a top view of the photomask and (b) side view of the SU-8 feature. The images are enlarged views of the areas marked by arrows in Figure 2-2. For (b), the image was taken at an 81º sample stage tilt to show feature height.

Table 2-1. Average photomask widths and feature heights for exposures of 100 and 150 mJ/cm^2.

Feature	Exposure (mJ/cm^2)	Photomask Width			Feature Height		
		average (nm)	σ (nm)	RSD	average (μm)	σ (μm)	RSD
a	150	380	10	2.7%	3.41	0.10	3.0%
b	150	570	14	2.5%	7.15	0.20	2.8%
c	100	570	14	2.5%	6.10	0.10	1.9%

2.4. Conclusions and future directions.

By exploiting the transmission properties of patterned apertures, the technique presented can easily produce structures with 3D topography and high aspect ratio structures by adjusting the mask width and exposure. Presently, the minimum SU-8 feature dimensions are limited by the photomask fabrication, but masks with features below 100 nm should be achievable. E-beam lithography is capable of producing features down to ~10-30 nm. These patterns can then be transferred to an underlying metal film with minimal broadening using an anisotropic technique such as reactive ion etching or FIB milling. This method will allow sub-100 nm features to be easily coupled to micrometer-scale structures in a single exposure step.

The minimum feature height achievable by this method will ultimately be limited by one or more considerations. Bethe's theory of diffraction by small holes predicts that transmission scales as the fourth power of the radius, resulting in a rapid decrease in transmission as aperture diameter decreases.[14] This drop-off in transmission, however, can be partially offset by adjusting the polarization of the radiation with respect to the aperture geometry. For example, transmission through a subwavelength rectangular aperture is much higher for light polarized along the minor axis than for polarization along the major axis.[15] In addition to the decrease in transmission for smaller apertures, the chemical properties of SU-8 will also limit the smallest feature which will adhere to a given substrate, and a probabilistic boundary will be imposed by diffusion of a single photoacid catalyst within the SU-8 film. Further experimental work will therefore be required to determine the minimum feature size achievable by this method.

Because of the robustness of the SU-8, these polymer features can be used as molds for micro- and nanofluidic channels and in optical sensing applications. Despite the advantages of this technique, however, devices in subsequent chapters were fabricated using multiple fabrication steps and multiple device layers. While this added to fabrication time, it permitted greater flexibility in device design because the dimensions of individual layers could be varied quickly and easily.

2.5. References.

1. This chapter reproduced in part with permission from Kovarik, M. L. and Jacobson, S. C. Fabrication of three-dimensional micro- and nanoscale features with single-exposure photolithography. *Anal. Chem.* **2006**, *78*, 5214-5217. Copyright 2006 American Chemical Society.
2. Madou, M. *Fundamentals of Microfabrication* (CRC Press, Boca Raton, FL, 2002).
3. Afromowitz, M. A. Method for fabricating 3-D structures with smoothly-varying topographic features in photo-sensitized epoxy resists. U.S. 6,635,412. 6,635,412. 2003.
4. Wong, W. H. & Pun, E. Y. B. SU8C resist for electron beam lithography. *Proc. SPIE* **2001**, *4345*, 873-880.
5. Sun, H.-B. & Kawata, S. Two-photon photopolymerization and 3D lithographic microfabrication. *Adv. Polym. Sci.* **2004**, *170*, 169-273.
6. Reyntjens, S. & Puers, R. A review of focused ion beam applications in microsystem technology. *J. Micromech. Microeng.* **2001**, *11*, 287-300.
7. Toepke, M. W. & Kenis, P. J. A. Multilevel microfluidics via single-exposure photolithography. *J. Am. Chem. Soc.* **2005**, *127*, 7674-7675.
8. Shaw, J. M., Gelorme, J. D., LaBianca, N. C., Conley, W. E. & Holmes, S. J. Negative photoresists for optical lithography. *J. Res. Develop.* **1997**, *41*, 81-94.
9. Amarie, D. A., Rawlinson, N. D., Schaich, W. L., Dragnea, B. & Jacobson, S. C. Three-dimensional mapping of the light intensity transmitted through nanoapertures. *Nano. Lett.* **2005**, *5*, 1227-1230.
10. Sundaramurthy, A., Schuck, P. J., Conley, N. R., Fromm, D. P., Kino, G. S. & Moerner, W. E. Toward nanometer-scale optical photolithography: utilizing the near-field of bowtie optical nanoantennas. *Nano. Lett.* **2006**, *6*, 3550369.
11. Srituravanich, W., Fang, N., Cheng, S., Luo, Q. & Zhang, X. Plasmonic nanolithography. *Nano. Lett.* **2004**, *4*, 1085-1088.
12. Stewart, M. D., Tran, H. V., Schmid, G. M., Stachowiak, T. M., Becker, D. J. & Willson, C. G. Acid catalyst mobility in resist resins. *J. Vac. Sci. Technol. B* **2002**, *20*, 2946-2952.

13. Chavez, K. L. & Hess, D. W. Removal of resist materials using acetic acid. *J. Electrochem. Soc*. **2003**, *150*, G284-G291.
14. Bethe, H. A. Theory of diffraction by small holes. *Phys. Rev.* **1944**, *66*, 163-182.
15. Jin, E. X. & Xu, X. Obtaining subwavelength optical spots using nanoscale ridge apertures. *J. Heat Transfer* **2007**, *129*, 37-43.

CHAPTER 3. Nanofluidic circuits for attoliter-scale dispensing.[1]

3.1. Introduction to fluid handling on nanofluidic devices.

As nanofluidic devices are developed for practical applications, researchers are determining which lessons from the microscale extrapolate to the nanometer regime. To date, few studies have been made which explore the behavior of nanofluidic intersections.[2,3] While some aspects of microchannel transport are expected to transfer directly to operation of smaller channels, nanochannels can exhibit phenomena such as double layer overlap, diffusion, and entropic forces that are either insignificant or absent in larger microchannels.[4] In order to investigate the effect of these and other phenomena on nanochannel fluid control, we have investigated attoliter-scale sample injections on an in-plane integrated micro- and nanochannel device. Fabrication of integrated micro- and nanoscale devices permits easy electrical control and fluid introduction the nanoconduits, and the nanochannels can be used to control sample dispensing.

Previous to this work, injections of this scale had been made only on lipid-based systems, where lipid nanochannels were used to transport aL to fL volumes between vesicles. Directed transport is achieved by increasing surface tension in one vesicle by mechanical deformation and simultaneously decreasing the surface tension in an adjacent vesicle by addition of excess membrane material, resulting in net flow of lipid membrane and contents between the two.[2,5] These systems exhibit control of extremely small volumes but lack the temporal response of electrically-driven fluid transport.

We have developed a hybrid glass-poly(dimethylsiloxane) (PDMS) device to effect attoliter-scale dispensing. Figure 3-1 shows a schematic and cross-section of the device used for these experiments. Glass microchannels provided fluid and electrical access to a

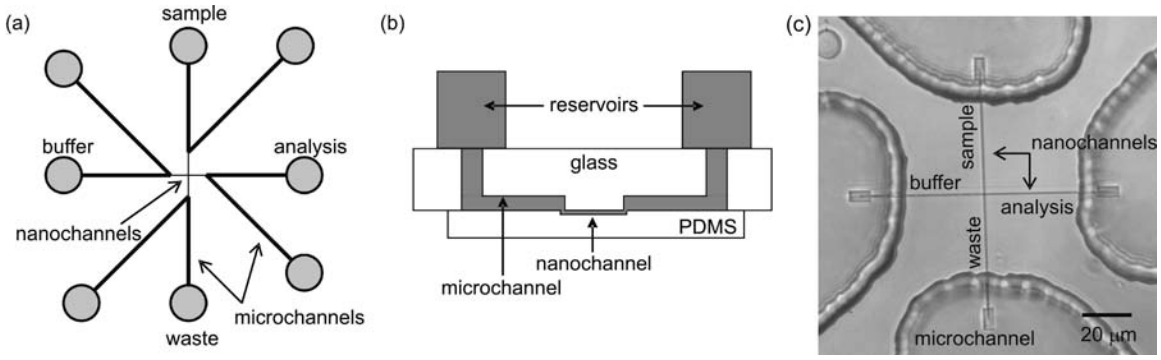

Figure 3-1. (a) Schematic of an assembled nanofluidic device. Microchannels were fabricated in a glass substrate and used for fluid access and application of voltages for electrokinetic transport. Nanochannels for fluid dispensing were fabricated in a PDMS layer which was reversibly sealed over the microchannels. (b) Cross-section of the device through the horizontal arm of the nanochannels. (c) Bright field image of an assembled device. PDMS and glass substrates were aligned and reversibly sealed so that the nanochannel cross overlapped slightly with glass microchannels to provide fluid and electrical access. Reservoir and channel labels in (a) and (c) reflect the modified pinched injection scheme. (a) and (b) are not to scale.

nanoscale cross design fabricated in PDMS. Figure 3-1c shows an optical micrograph of a fully assembled device with the PDMS nanochannels sealed to overlap with the glass microchannels.

3.2. Methods.

To fabricate the nanochannels, we used electron beam (e-beam) lithography to form nanochannel masters in the negative tone resist SU-8. Glass substrates (25 x 25 x 1 mm) were prepared as in Section A1 with the following exceptions. No SU-8 adhesion layer was used, and the SU-8 2010 (MicroChem Corp.) for patterning was diluted to 25% by volume in cyclopentanone prior to spin-coating to produce a thinner resist layer. The SU-8 spin cycle consisted of a 5 s spread cycle at 500 rpm followed by 30 s at 3000 rpm. E-beam lithography was performed on a LEO 1430 scanning electron microscope (SEM; Zeiss SMT, Inc.) equipped with a Nano Pattern Generation System (JC Nabity Lithography Systems). The nanocross pattern consisted of 50 μm long channels terminated by 5 x 10 μm contact pads for alignment with the microchannel connections. The nanochannels were written with a single pass of the electron beam (exposure energy = 0.19 nC/cm), and the contact pads were written by a raster scan (exposure energy = 2.2 $\mu C/cm^2$). The exposure energies used were much lower than those described for PMMA in Chapter 2 due to the higher sensitivity of the SU-8 resist.[6] After processing, SU-8 masters were silanized overnight in a desiccator containing ~300 μL of (tridecafluoro-1,1,2,2-tetrahydrooctyl)-1-trichlorosilane (United Chemical) to promote release of the cured replicas.[7] PDMS (Sylgard 184, Dow Corning) replicas were prepared as described in Section A2.

The second piece of the device was formed in glass and contained four V-shaped microchannels. Borosilicate glass substrates (B270) were processed according to standard lithographic techniques as described in Section A3. Microchannel dimensions were determined using a stylus profiler (Dektak 6M, Veeco), and each branch of the V-shaped channel was ~1 cm long, 10 μm deep, and 70 μm wide at the top. After fabrication of the glass substrate with microchannels and PDMS substrate with nanochannels, the two pieces were cleaned, aligned using an optical microscope, and reversibly sealed together. After alignment and sealing, each nanochannel was ~40 μm long from the cross intersection to the corresponding microchannel. The resulting device contained channels in two layers (Figure 3-1b).

In capillaries and microfluidic devices, electrokinetic transport typically requires application of thousands of volts in order to generate high field strengths and practical fluid velocities. However, in these experiments, voltages were supplied directly from an analog output board (PCI-6713, National Instruments) without amplification and applied through platinum wire electrodes placed in the reservoirs at the ends of the V-shaped microchannels. Approximately 98% of the applied voltage was dropped across the PDMS nanochannels due to their small cross-sectional area relative to the microchannels. Since the nanochannels were typically 40 μm long, even low applied voltages resulted in high field strengths in the nanochannels. The currents in each of the four fluidic channels were monitored, and each monitoring circuit used an AD621B instrument amplifier (Analog Devices) to measure the voltage drop across a 10 MΩ resistor which was placed in series between the analog output board and fluid reservoir. Because the equivalent resistance of the assembled fluidic device was in the gigaohm range, the voltage drop across the 10

MΩ resistor was minimal (2-3%). All voltages are reported as nominal values, which do not include the drop across the current monitoring circuit.

To monitor flow and dispensing operations within the nanochannels, we used fluorescence detection with disodium fluorescein as a probe. An inverted optical microscope (TE-2000U, Nikon) microscope was configured for epifluorescence and equipped with a 40x XLWD objective and HQ FITC filter cube (Chroma Technology Corp.). For imaging experiments, a metal halide lamp (X-Cite 120, EXFO) was used for excitation, the fluorescence signal was detected with a CCD camera (Cascade 512B, Photometrics), and images were captured and processed using IPLab software (BD Biosciences). For measurements at a single point, the same microscope was used. The 488 nm line of an argon ion laser (Melles Griot) was attenuated to 0.5 mW with neutral density filters and focused to a point in the analysis channel (25 or 30 μm downstream from the cross intersection). The fluorescence signal was spatially filtered through a 150 μm pinhole, detected with a photomultiplier tube (PMT; H5783-01, Hamamatsu), amplified by a low-noise current preamplifier (SR570, Stanford Research Systems), recorded with LabView (National Instruments), and analyzed in Origin Pro 7.5 (OriginLab).

For the dispensing experiments, the buffer contained 10 mM sodium tetraborate (Sigma-Aldrich) and 1 mM sodium dodecyl sulfate (SDS; Sigma-Aldrich). SDS was added to the buffer to help wet the nanochannels and increase the electroosmotic mobility. Samples of 0.1 and 1 mM disodium fluorescein (Sigma-Aldrich) in the borate buffer were used to evaluate dispensing for detection at a single point and imaging, respectively. All solutions were filtered with a 0.2 μm nylon syringe filter (Pall) before

use. The buffer and sample solutions were loaded into the reservoirs, the solutions were drawn into the microchannels by applying vacuum, and the nanochannels filled by capillary action.

3.3. Results and discussion.

Two devices were used to conduct these studies and are referred to below as device A and device B. The SU-8 master used to fabricate chips for device A had nanochannel patterns 380 ± 10 nm high and 400 ± 10 nm wide. Figure 3-2a-c shows the SU-8 master used to mold the PDMS nanochannels used for device A. SEM images showed that the PDMS chips were not exact replicas of the SU-8 masters (Figure 3-2d). However, multiple castings using the same master produced nanochannels in the PDMS with repeatable dimensions. The PDMS channels had trapezoidal cross-sections that were 130 ± 10 nm deep with an average width of 580 ± 40 nm. Relaxation of the cured PDMS or poor wetting of the PDMS on the SU-8 feature[8] may have caused the replicas to be broader and shallower than the master. Increased cure time (24 h at 70 ºC) was tested as a possible means of minimizing channel deformation in the PDMS replicas but did not have an appreciable effect on the channel dimensions or geometry. A similar but slightly larger SU-8 master was used to fabricate nanochannels for device B. The device B channel patterns were 430 ± 20 nm high and 620 ± 40 nm wide in SU-8 and resulted in PDMS channels that were 130 ± 20 nm deep and had an average width of 670 ± 25 nm.

Two electrokinetic dispensing schemes were investigated, the modified pinched and gated injections, both capable of delivering variable volumes to the analysis channel. Figure 3-3 shows the load and inject modes for the modified pinched injection. During

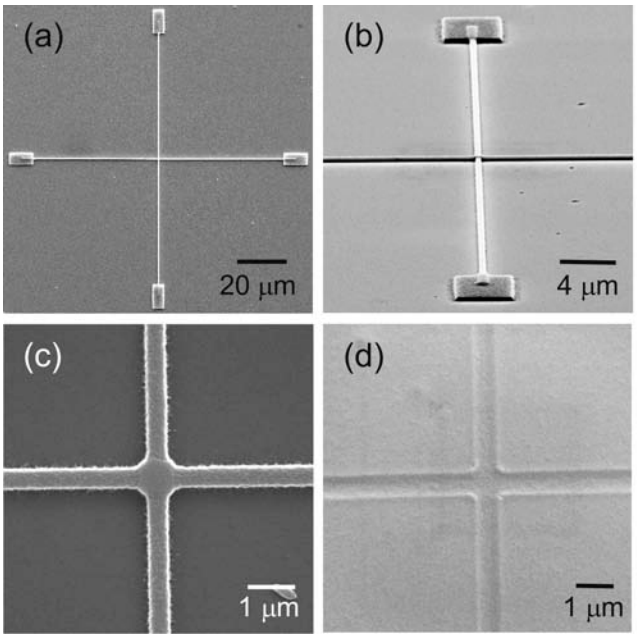

Figure 3-2. (a) Scanning electron microscope (SEM) image of a cross channel master fabricated in SU-8 by electron beam lithography. Channels were 50 μm long and were terminated by 5 μm by 10 μm connection regions for overlap with the glass microchannel chip. (b) SEM image of the same master taken at an 81º tilt. (c) Enlarged view of the intersection of the channel mold. Channel molds were 400 ± 10 nm wide and 380 ± 10 nm high. (d) SEM image of the cross intersection on a PDMS replica of the master seen in (a) – (c). Replica channels were 130 ± 10 nm deep and had an average width of 580 ± 40 nm. The SU-8 master shown here was used to mold the nanochannels in device A.

loading, sample was confined to the cross by streams flowing toward the intersection from both the buffer and analysis channels (load mode in Figure 3-3a). In a typical pinched injection, the voltages applied to the analysis and sample channels are lowered to inject the sample volume in the cross intersection into the analysis channel.[9] In order to inject variable volumes, this valving scheme was modified to include a period of additional sample injection. During the injection, the voltages at both the buffer and sample reservoirs were left high, so that additional sample was injected into the analysis channel for a fixed period of time, e.g., 1 to 100 ms (inject mode in Figure 3-3b). For the image in Figure 3-3b, a long inject time (~1 s) was used in order to capture the image. The injection was terminated by lowering the sample reservoir voltage so that buffer swept the injected plug down the analysis channel (run mode). Due to the speed with which the analysis channel was cleared of sample, the run mode is not pictured in Figure 3-3. After the sample plug reached the end of the channel, load mode was re-established. The applied voltage (V) in Figure 3-3 was the same at the designated reservoirs and ranged from 2 to 10 V to vary the analyte velocity for these experiments. Injections in this study were easily performed at a frequency of 5 Hz, despite letting the previous plug exit the analysis channel before the subsequent plug was injected. This was possible because the short length of the analysis channel (40 μm) and high linear velocities quickly cleared sample from the analysis channel.

As a first test, standard pinched injections were performed on devices A and B. For these injections, the injection volume was assumed to be equal to the volume of the intersection. The intersection volume was 42 aL for device A and 58 aL for device B. These injections were highly repeatable on both devices; relative standard deviations

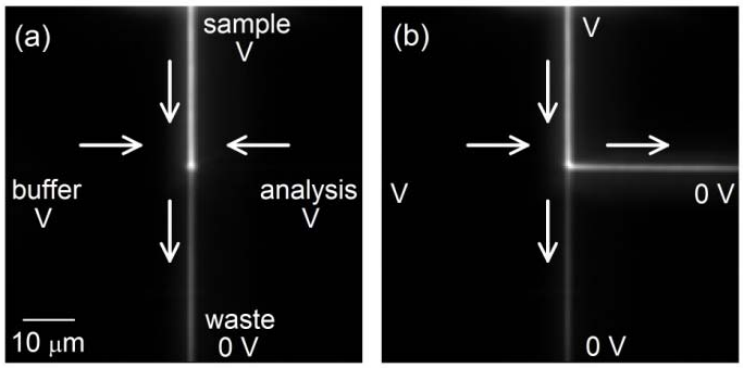

Figure 3-3. Fluorescence images of the (a) load and (b) inject modes for modified pinched injections on device B. (a) To transport and confine sample to the cross intersection in load mode, 10 V were applied to the buffer, sample, and analysis reservoirs, and the waste reservoir was grounded. (b) In inject mode, the analysis reservoir was grounded to route sample down the analysis channel. To dispense a discrete sample plug (run mode not shown), the sample reservoir was then grounded to allow buffer to sweep the sample plug down the analysis channel. Arrows indicate the direction of flow.

(RSDs) of the peak area (n = 10) were 2.6% for device A and 1.9% for device B when 5 V was the applied voltage. Figure 3-4 shows injection profiles for a standard pinched injection and four modified pinched injections on device B. The solid line represents a standard pinched injection in which no additional injection time was applied. Modified pinched injections were also performed during which the sample reservoir was left at 5 V for 1, 3, 5, and 10 ms to increase the injected volume. These injections corresponded to volumes ranging from 58 aL for the standard pinched injection to 2.1 fL for the 10 ms injection, and the peak areas were linear with injection time (R^2 = 0.9999). The 5 V modified pinched injections showed good repeatability with RSDs ranging from 0.8% to 2.7% for peak area and from 2.2% to 4.0% for peak height (n = 10 for each injection time).

Figure 3-5 demonstrates the repeatability of a 670 aL modified pinched injection and shows ten 3 ms injections (peak area RSD = 2.7%, peak height RSD = 2.2%). For the data shown in Figures 3-4 and 3-5, velocity increased linearly with field strength (R^2 = 0.9999), and the electrokinetic mobility, μ_{ek}, was 3.7×10^{-4} $cm^2V^{-1}s^{-1}$. This agreed well with an estimated value of 3.3×10^{-4} $cm^2V^{-1}s^{-1}$, calculated by assuming an electrophoretic mobility, μ_{ep}, of -3.7×10^{-4} $cm^2V^{-1}s^{-1}$ for fluorescein[10] and an electroosmotic mobility, μ_{eo}, of 7×10^{-4} $cm^2V^{-1}s^{-1}$ for PDMS channels filled with high pH buffer containing > 0.7 mM SDS.[11] Modified pinched injections were also made using applied voltages of 2.5 and 10 V to determine if field strength influenced dispensing behavior. With 2.5 and 10 V applied, the field strengths in the analysis channel during injection were 320 and 1280 V/cm, respectively, and corresponded to analyte velocities of 1.2 and 4.7 mm/s. Both the linearity and the repeatability of these injections were comparable to those of the 5 V

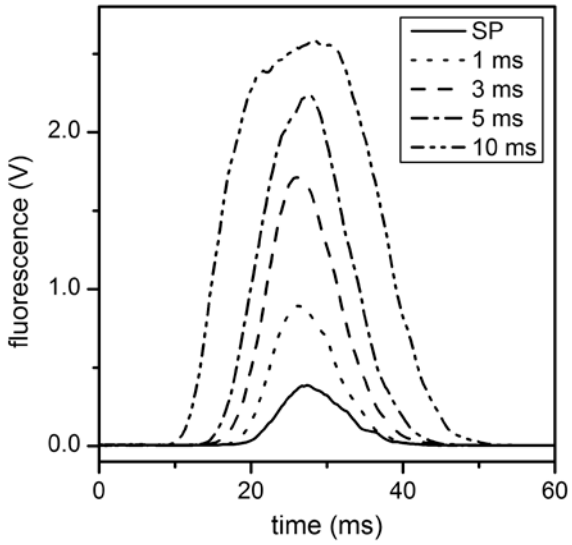

Figure 3-4. Injection profiles for a standard pinched (SP) injection and 1, 3, 5, and 10 ms modified pinched injections corresponding to injected volumes of 0.058, 0.26, 0.67, 1.1, and 2.1 fL, respectively. The injections were performed on device B, the applied voltage was 5 V, and the detection point was 30 μm from the cross intersection in the analysis channel.

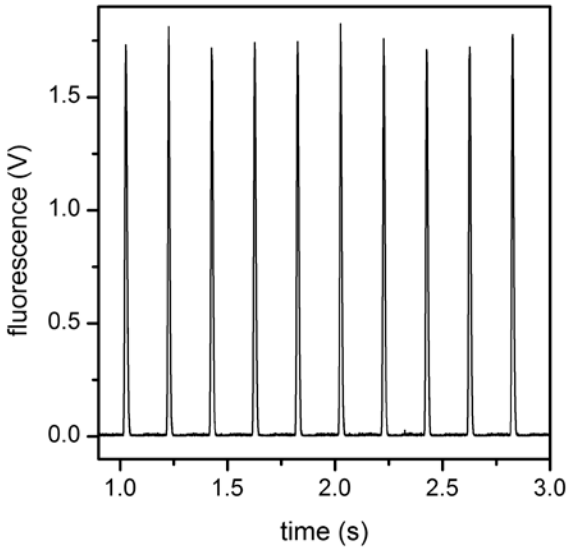

Figure 3-5. Ten 3 ms modified pinched injections made on device B with 5 V applied. The injection volume was 670 aL, the repetition rate was 5 Hz, and the detection point was 30 μm from the cross intersection in the analysis channel.

injections described above. In addition, with 10 V applied, the largest volume injections were 4.1 fL for the 10 ms injection.

While the data shown in Figures 3-4 and 3-5 showed a consistent relationship between velocity and field strength, the nanofluidic devices periodically did not function as predicted due to stabilization of the nanochannels and PDMS/glass interface. To investigate these variations, experiments were performed in which a series of 100 ms modified pinched injections were made on device B for applied voltages of 2, 4, 6, 8, and 10 V at 30 min intervals. The variation in analyte velocity, the ratio of analysis channel current to total current, and the equivalent resistance of the fluidic device were evaluated. After an initial drop, analyte velocity stabilized to < 3% RSD after approximately 1 h and remained stable for the duration of the experiment (~1 h). The ratio of analysis channel current to total current through the device also showed a similar trend over time. This ratio was indicative of the electric field in the analysis channel relative to the entire chip, and therefore, reflected the change in velocity. Finally, the equivalent resistance of the chip decreased in discrete, irregular steps over the course of the experiment before leveling off.

These data suggested that the PDMS channels and the PDMS/glass interface required time to stabilize after bonding and filling with buffer. Subtle changes in the relative channel resistances caused the field strength and velocity in the analysis channel to vary. After 1.0 h, the nanochannels and interface stabilized, as reflected by the leveling off of the velocity and currents. In general, current monitoring capability allowed ready identification of any changes in behavior or device failure during the dispensing

experiments. Although infrequent, device failure was observed when the PDMS/glass interface delaminated and was easily detected by a sharp increase in the current.

In addition to the modified pinched injections discussed above, a gated injection scheme[9] was evaluated. Figure 3-6 shows fluorescence images of the load and inject modes for the gated valve. During loading, voltages were applied at the buffer and sample reservoirs, and the waste and analysis reservoirs were grounded (Figure 3-6a). To inject a sample plug, the voltage at the buffer reservoir was lowered to match that at the sample reservoir. Additionally, the waste reservoir voltage was raised to minimize change in the analysis channel field strength between loading and injection (Figure 3-6b). Figure 3-6 shows gated valve operation with 10 V at the buffer reservoir and 4.5 V at the sample reservoir during load mode and 4.5 V at the sample, buffer, and waste reservoirs during inject mode.

Gated injections were made at a repetition rate of 5 Hz with injection times of 1, 3, 5, and 10 ms on devices A and B with similar results for both. Overall, the gated injections were less repeatable than the modified pinched injections with RSDs for peak areas ranging from 1.0% to 7.4%. Elevated baselines were observed during gated valve operation, indicating that analyte molecules were leaking into the analysis channel during loading mode. Figure 3-6a illustrates that during load mode sample reached the cross intersection, entered the waste channel, and was diluted by buffer flow. This was evident from the decrease in fluorescence intensity in the waste channel compared to the sample channel. In a microfluidic device, this typically prevents sample from leaking into the analysis channel during sample loading.

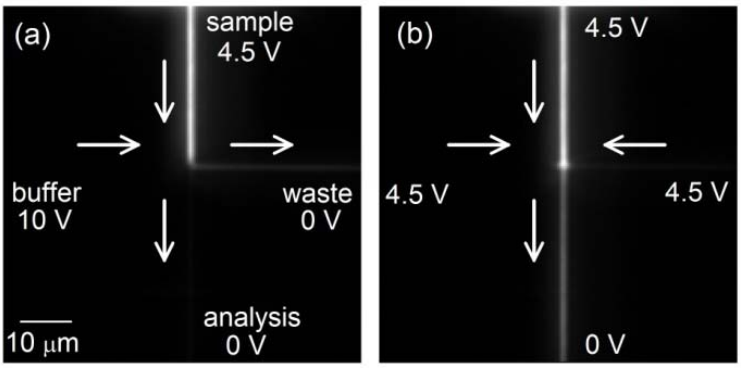

Figure 3-6. Fluorescence images of the (a) load and (b) inject modes for gated injections on device B. (a) In load mode, the sample was transported through the cross intersection to the waste reservoir by applying voltages to the buffer and sample reservoirs and grounding the waste and analysis reservoirs. (b) To make an injection, the voltage at the buffer reservoir was lowered to allow sample to enter the analysis channel, and the voltage at the waste reservoir was simultaneously raised to maintain a similar field strength in the analysis channel during the injection. Arrows indicate direction of flow.

Consequently, we attributed the leak to the relative time scales of electrokinetic transport and diffusion in the nanochannels. A conservative estimate of the time required for an analyte molecule to electrokinetically traverse the cross intersection was equal to the channel width divided by the analyte velocity. Assuming the analyte molecule had to traverse a channel width of 670 nm (device B), had an electrokinetic mobility of 3.7×10^{-4} $cm^2V^{-1}s^{-1}$, and was traveling in an electric field of 300 V/cm, the velocity and transit time were 1.1 mm/s and 0.60 ms, respectively. Similarly, the time for a molecule to diffuse from the sample stream to the buffer stream can be approximated by[12]

$$t_{diff} = \frac{d^2}{2D} \tag{3.1}$$

where d is the channel width and D is the diffusion coefficient of fluorescein (4.25×10^{-6} cm^2/s).[13] The estimated time to diffuse was 0.53 ms. Because diffusion in the nanochannels occurred on the same time scale or even faster than electrokinetic transport, diffusional leaking between the sample and buffer streams was possible. As a result, normal operation of a gated valve in the nanochannels was problematic.

3.4. Conclusions and future directions.

We have demonstrated precise attoliter-scale fluid dispensing in a nanochannel cross chip using a modified pinched injection. This device had extremely low power requirements, running with applied voltages up to 10 V and currents typically around 10 nA. The modified pinched injection scheme was used for repeatable, variable volume electrokinetic injections, while experiments with gated valving highlighted the importance of diffusion on this scale. Injected volumes as small as ~40 aL were obtained using a standard pinched injection, making these devices suitable for analyses of single

organelles. Recently, electrophoretic separation of the contents of individual mitochondria has been reported.[14] Each mitochondrion is approximately 0.5 μm in diameter and holds about 10 aL of sample. Lysis, injection, and separation of mitochondrial contents on a nanofluidic device would result in a significant improvement in signal-to-noise by reducing fluorescence background and minimizing the volume available for diffusion.

Results from these experiments could be further improved by using a substrate material other than PDMS. Casting the nanochannels in PDMS limited the lower bound for channel dimensions because commercially available PDMS (Sylgard 184) does not replicate features smaller than ~250 nm well.[15] Although casting was reproducible, the PDMS channels in Figure 3-2 were not exact replicas of the original SU-8 master. Using an alternative polymer, such as h-PDMS or a photocurable perfluoropolyether (PFPE), to form nanochannels can minimize or eliminate these issues. h-PDMS is a high-modulus derivative of PDMS[15] which has been used for imprint lithography with molecular scale resolution.[16] An α-,ω-methacryloxy functionalized PFPE has been used to replicate 140 nm wide, 50 nm deep features with 70 nm spacing,[17] and PFPEs have the additional advantages of high modulus, good releasing properties, and compatibility with organic solvents and hydrophobic analytes.

Work on nanochannels fabricated with these polymers is on-going in the Jacobson laboratory and has led to reduced device dimensions. The modified pinched valving scheme presented demonstrated the capability of nanofluidic devices for precise manipulation of attoliter fluid volumes on short time scales and should be applicable to even smaller channels. These devices represent the state-of-the-art in planar nanofluidics,

but nanofluidic elements can also be incorporated out of the plane of microfluidic devices. The remainder of the work presented in this dissertation deals with out-of-plane nanofluidic devices due to the reproducibility and relative ease of their fabrication. Additionally, out-of-plane nanofluidic interconnects permit multilayer devices to be fabricated, potentially adding functionality without increasing device footprint.

3.5. References.

1. This chapter reproduced in part with permission from Kovarik, M. L. and Jacobson, S. C., Attoliter-scale dispensing in nanofluidic channels, *Anal. Chem.* **2007**, *79*, 1655-1660. Copyright 2007 American Chemical Society.
2. Karlsson, R., Karlsson, A. & Orwar, O. A nanofluidic switching device. *J. Am. Chem. Soc.* **2003**, *125*, 8442-8443.
3. Riehn, R., Austin, R. H. & Sturm, J. C. A nanofluidic railroad switch. *Nano. Lett.* **2006**, *6*, 1973-1976.
4. Eijkel, J. C. T. & van den Berg, A. Nanofluidics: what is it and what can we expect from it? *Microfluid Nanofluid* **2005**, *1*, 249-267.
5. Karlsson, R., Karlsson, M., Karlsson, A., Cans, A.-S., Bergenholtz, J., Akerman, B., Ewing, A. G., Voinova, M. & Orwar, O. Moving-wall-driven flows in nanofluidic systems. *Langmuir* **2002**, *18*, 4186-4190.
6. Pépin, A., Studer, V., Decanini, D. & Chen, Y. Exploring the high sensitivity of SU-8 resist for high resolution electron beam patterning. *Microelectron. Eng.* **2004**, *73-74*, 233-237.
7. Duffy, D. C., Schueller, O. J. A., Brittain, S. T. & Whitesides, G. M. Rapid prototyping of microfluidic switches in poly(dimethyl siloxane) and their actuation by electro-osmotic flow. *J. Micromech. Microeng.* **1999**, *9*, 211-217.
8. Kang, H., Lee, J., Park, J. & Lee, H. H. An improved method of preparing composite poly(dimethylsiloxane) moulds. *Nanotechnology* **2006**, *17*, 197-200.
9. Jacobson, S. C., Hergenroder, R., Koutny, L. B., Warmack, R. J. & Ramsey, J. M. Effects of injection schemes and column geometry on the performance of microchip electrophoresis device. *Anal. Chem.* **1994**, *66*, 1107-1113.
10. Manz, A., Effenhauser, C. S., Burggraf, N., Harrison, D. J., Seiler, K. & Fluri, K. Electroosmotic pumping and electrophoretic separations for miniaturized chemical analysis systems. *J. Micromech. Microeng.* **1994**, *4*, 257-265.
11. Badal, M. Y., Wong, M., Chiem, N., Salimi-Moosavi, H. & Harrison, D. J. Protein separation and surfactant control of electroosmotic flow in poly(dimethylsiloxane)-coated capillaries and microchips. *J. Chrom. A* **2002**, *947*, 277-286.
12. Giddings, J. C. *Unified separation science* (Wiley-Interscience, New York, 1991).

13. Culbertson, C. T., Jacobson, S. C. & Ramsey, J. M. Diffusion coefficient measurements in microfluidic devices. *Talanta* **2002**, *56*, 365-373.
14. Allen, P. B., Doepker, B. R. & Chiu, D. T. High-throughput capillary-electrophoresis analysis of single mitochondria. *Anal. Chem.* **2009**, *81*, 3784-3791.
15. Schmid, H. & Michel, B. Siloxane polymers for high-resolution, high-accuracy soft lithography. *Macromolecules* **2000**, *33*, 3042-3049.
16. Hua, F., Sun, Y., Gaur, A., Meitl, M. A., Bilhaut, L., Rotkina, L., Wang, J., Geil, P., Shim, M. & Rogers, J. A. Polymer imprint lithography with molecular-scale resolution. *Nano. Lett.* **2004**, *4*, 2467-2471.
17. Rolland, J. P., Hagberg, E. C., Denison, G. M., Carter, K. R. & De Simone, J. M. High-resolution soft lithography: Enabling materials for nanotechnology. *Angew. Chem. Int. Ed.* **2004**,

CHAPTER 4. Photolithographic isolation of single track-etch nanopores.

4.1. Introduction to track-etch nanopores and their applications.

In-plane nanofluidic systems, such as the one discussed in Chapter 3, are useful because of the ease with which the systems can be assembled and imaged. However, out-of-plane devices, in which the nanofluidic element is positioned orthogonal to the substrate, are also of interest, particularly because they are compatible with multilayer devices. Nanopore membranes are well-suited to incorporation in these devices, since they can easily be placed between microfluidic device layers to provide nanoscale fluidic connections.

We have chosen to pursue track-etch membranes for integration in fluidic devices. When compared to other nanoporous materials, track-etch membranes have a number of advantages, including adjustable pore diameter and geometry, arbitrary pore density, uniform pore dimensions and orientation, and applicability to a wide variety of materials.[1] Tracks can be produced in most dielectric materials by exposing them to energetic fission fragments or heavy ions. The resulting damage tracks are selectively etched to leave nanopores with diameters as small as 10 nm. Conical pores can be produced by etching the membrane from one side while bathing the opposite side in a neutralizing stop solution.[2] Additionally, chemical modification of track-etch pores can increase their selectivity for transport and/or sensing. A wide variety of thiol chemistries are available by using electroless plating to coat the pore walls with gold,[3] and the hydrophobicity of poly(ethylene terephthalate) (PET) pores can be modified by alkylation of the carboxylic acid groups on hydrolyzed pore walls.[4]

One disadvantage of track-etch membranes, however, is that damage tracks are randomly dispersed across the membrane surface, making isolating and addressing individual pores for chemical modification or single particle sensing difficult. As one strategy to overcome this difficulty, we have demonstrated the use of photolithography to isolate individual and small ensembles of track-etch nanopores in PET membranes. Figure 4-1 shows a schematic of the patterning process. Lithographically defined arrays were used to expose pores in pre-defined locations with single pores successfully isolated in >30% of all cases with a success rate defined by Poisson statistics.

4.2. Methods.

Tracked polycarbonate and PET membranes with 10^6 tracks/cm^2 were obtained from GSI, Darmstadt DE and etched for 2 h to form conical nanopores as described in Section A4. Etched membranes were placed on 25 mm × 25 mm glass substrates and spin-coated with SU-8 2010 photoresist on the base side of the pores (Microchem Corp.). Transparency photomasks were obtained from the Photoplot Store. Each photomask was 25 mm × 25 mm and consisted of a 10 × 10 array of opaque squares with edges of 12, 25, or 70 μm. In the following discussion, the masks and the resulting patterns are referred to by the edge-length of the square patterns. Because SU-8 is a negative tone photoresist, the masks were designed to be opaque in areas where access to the underlying membrane was desired. For the 70 μm square photomask, a 3 μm thick SU-8 layer was used; and for the 12 and 25 μm patterns, a 6 μm layer was used. The SU-8 layer was then processed as described in Section A1 with exposure energies ranging from 100 – 200 mJ/cm^2 depending on the dimensions of the photomask and the desired pattern size. The smaller

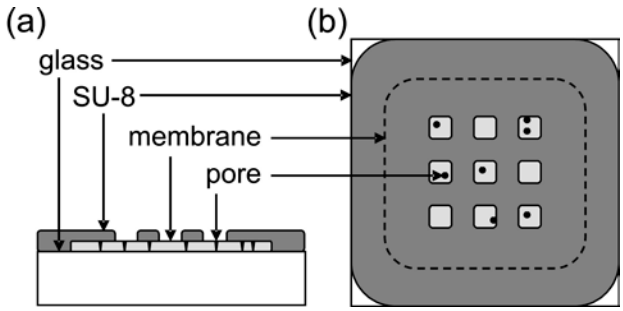

Figure 4-1. (a) Cross-sectional and (b) top schematic views of the process used to isolate track-etch pores photolithographically. Track-etch membranes were placed on glass substrates, spin-coated with SU-8 photoresist, exposed to UV light, and developed to transfer an array pattern to the SU-8 layer.

patterns required lower exposure energies to avoid over- exposure at the corners. Before developing of the SU-8 photoresist, the membranes were gently removed from the glass support.

Patterned membranes were sputter-coated with ~10 nm of gold and characterized using a scanning electron microscope (SEM; LEO 1430, Zeiss SMT, Inc.) to determine the number of pores isolated as well as the size and uniformity of the squares in each array. SEM images of the patterns were imported into IPLab software (BD Biosciences) to determine the area of each square.

4.3. Results and discussion.

Initially, both polycarbonate and PET membranes were considered for patterning. We had previously used electron-beam lithography to pattern commercially available, high pore density (10^8 pores/cm^2) polycarbonate membranes (GE Osmonics). Commercial membranes have the advantages of being readily available, relatively inexpensive, and pre-etched to pore diameters down to 10 nm; however, the high pore densities required a patterning technique with higher resolution than our UV exposure system provided. Using electron beam lithography, we successfully isolated 100 nm pre-etched pores in 740 nm diameter apertures in a poly(methylmethacrylate) (PMMA) film (900 kDa, MicroChem Corp.). Figure 4-2 shows SEM and atomic force microscope (MFP-3D; Asylum Research) images of a single aperture in a PMMA film containing two nanopores. While electron beam lithography was successful for isolating pores in high pore density membranes, patterns were written serially and substantial technical expertise was required to produce the patterns. Photolithographic patterning is preferable because a

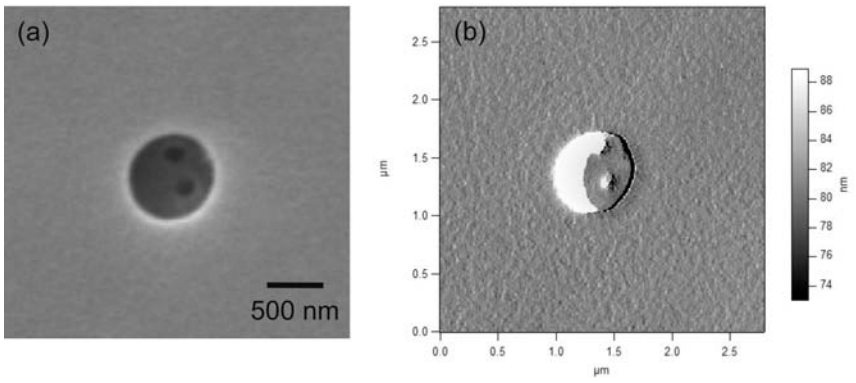

Figure 4-2. (a) SEM image of a single 740 nm hole written in PMMA which isolated two pores in a polycarbonate membrane. (b) AFM amplitude trace of the same feature at the same scale.

large area can be patterned in a single exposure, and we evaluated UV photolithographic pore isolation with lower track density membranes, e.g., 10^6 /cm^2.

Nanopores were etched into tracked polycarbonate and PET membranes as described in Section A4. After 2 h of etching, conical nanopores were formed which were ~200 nm in diameter at the tip and ~1.5 μm at the base. Polycarbonate membranes etched in-house were incompatible with the Nano PG developer used for SU-8 processing and with solvents commonly used with other photoresists. PET membranes were more chemically robust than polycarbonate membranes and withstood exposure to the SU-8 solvent, cyclopentanone, and the Nano PG developer, propylene glycol monomethyl ether acetate containing proprietary surfactants. As a result, all subsequent lithographic patterning experiments were performed with PET membranes.

The 12, 25, and 70 μm photomasks, corresponding to 144, 625, and 4900 μm^2 opaque regions, resulted in open areas in the SU-8 film of 89 ± 10 (n = 97), 369 ± 89 (n = 99), and 4134 ± 264 μm^2 (n = 20). One 10 × 10 array pattern was evaluated for each edge-length, and these arrays resulted in 97 – 99 openings with the remaining 1-3 openings being over-exposed or damaged. SEM images of part of an array produced with the 70 μm photomask and a close-up of one open square are shown in Figure 4-3. Figure 4-3a demonstrates the capability of this technique to pattern large areas rapidly, as the field of view shown is several millimeters on a side. As seen in Figure 4-3b, the corners of the openings were rounded and the open areas in the SU-8 film were smaller than the photomask patterns due to scattering of light around the edges of the photomask, especially at the corners of the square designs. The roughness along the edges of the squares likely results from the edge roughness of the photomask. Figure 4-4a,c shows

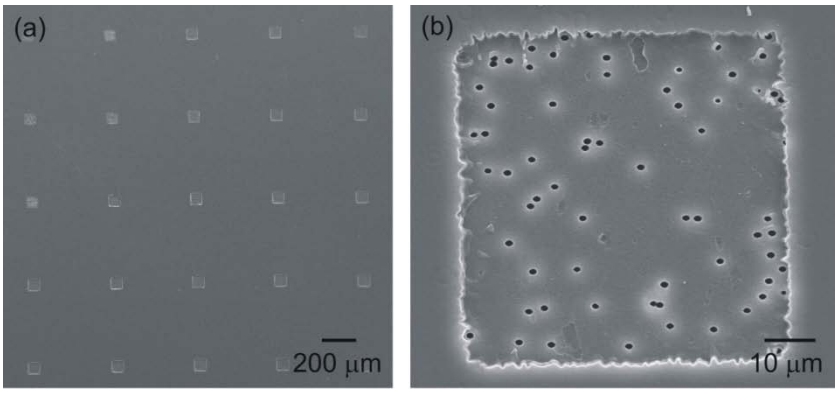

Figure 4-3. SEM images of a PET membrane patterned by photolithography. (a) 5 x 5 array produced using the 70 µm mask and a 3 µm thick SU-8 film. (b) Enlarged image of one of the squares containing 64 individual conical pores.

SEM images of the smaller patterns with a single pore isolated in an 85 μm^2 opening and 5 pores exposed in a 390 μm^2 opening.

Due to the random distribution of pores on the membrane surface, the probability of isolating a single pore in a given area was governed by Poisson statistics. Based on Poisson statistics, the probability, P, of an event occurring k times in a given area or time is defined as

$$P = \frac{e^{-\lambda}\lambda^{k}}{k!} \tag{4.1}$$

where λ is the average number of events that occur in the time-interval or area.[5] For these experiments, λ, the average number of pores in a given area, was calculated using the overall pore density of the membranes, 10^6 pores/cm^2. Application of Equation 4.1 shows that the maximum success rate for isolation of a single pore is 37% for the optimal pattern size, a 10 μm x 10 μm square. Zero pores are predicted in 37% of the square openings, and two pores in 18%. The actual distributions of pores isolated in the 12 and 25 μm photomask patterns are given in Figure 4-4b,d. The expected distributions given by Poisson statistics are also shown. For the 12 and 25 μm photomasks the actual and expected distributions agreed well. For the larger 70 μm patterns, the distributions were broader and consequently were not necessarily reflected in the observed distributions for the small arrays used.

The average number of pores in each opening was 0.8, 3, and 53 for the 12, 25, and 70 μm square openings, respectively. For the 12 μm openings, a total of 34 openings out of 99 contained an individual isolated nanopore, i.e. 34.3%. Photomasks could easily be designed with large arrays of openings to create enough redundancy that this 34% success rate would be sufficient for many applications. The number of pores in each array

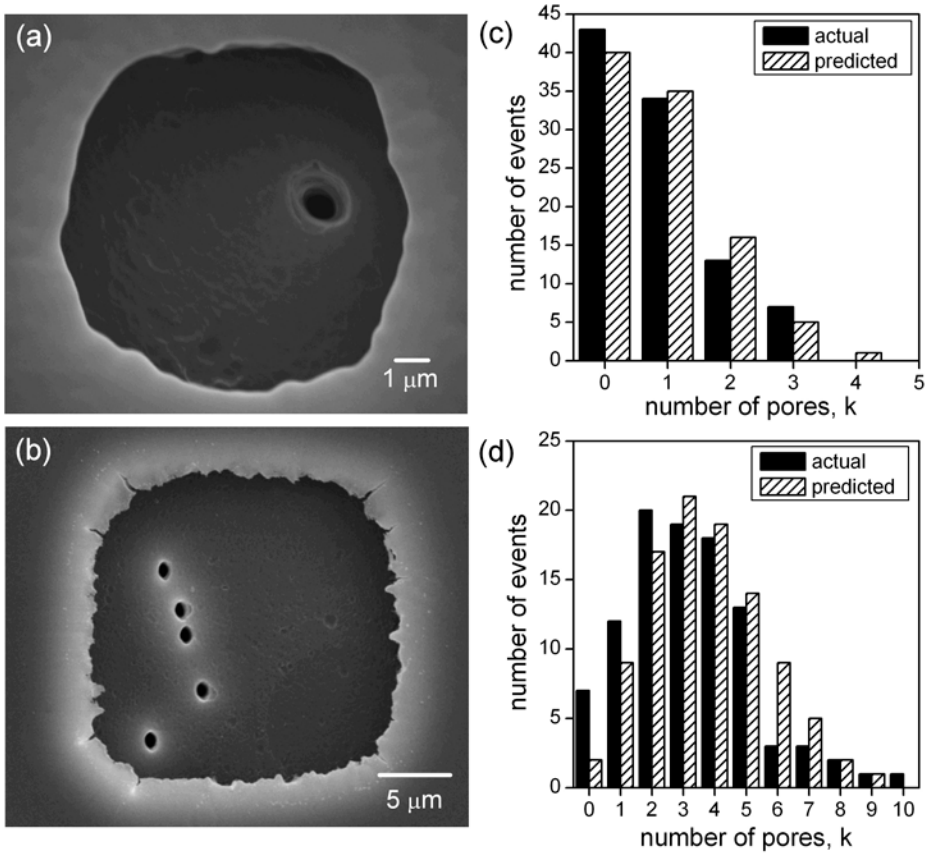

Figure 4-4. SEM images of (a) 12 μm and (b) 25 μm pattern openings in an SU-8 film which have exposed 1 and 5 pores, respectively. Actual and expected pore distributions for each sample are given in (c) and (d). The distribution in (c) corresponds to the sample containing the pattern shown in (a) and includes n = 97 square openings. Panel (d) corresponds to (b) and includes n = 99 square openings.

element was easily determined by inspection by either SEM or inverted optical microscopy. Such an inspection or a local current measurement could be used to determine which openings contain a single pore suitable for use as a sensor.

4.4. Conclusions and future directions.

Photolithographic patterning of track-etch membranes opens up the possibility of massively parallel analyses using nanopores. Although direct-write techniques, such as ion-beam milling,[6] can be used to create pores at arbitrary locations, UV photolithography is a far less time-intensive means of achieving a similar result. The feasibility of lithographic pore isolation has been demonstrated here; however, some improvements are required before this method can be applied to fluidic devices. Cross-linked SU-8 photoresist is brittle, and the resist films typically cracked during handling so that the patterned regions of the membrane were not electrically isolated from regions under the SU-8 film. In the time since this work was performed, a less brittle epoxide-based photoresist has been developed as an alternative to SU-8.[7] The 1002F resin has only two epoxide groups per monomer, compared to eight residues per SU-8 monomer. As a result, 1002F photoresist produces softer and more flexible films after cross-linking than SU-8 does. An additional benefit of this material is reduced auto-fluorescence compared to SU-8 for excitation wavelengths above 400 nm, making the 1002F resin preferable for applications involving fluorescence detection.

Electrical isolation of nanopores in specific locations will make it possible to address a given nanopore using nano- and microfluidic architectures. Each pore could be chemically modified on an individual basis to create an array of pores with a variety of

chemical functionalities with the eventual goal of a high-throughput, automated nanopore analysis device. Prior to pursuing such a device, we have chosen to characterize small ensembles of pores and individual pores isolated directly by microfluidic channels. These efforts are described in Chapters 5-7.

4.5. References.

1. Fischer, B. E. & Spohr, R. Production and use of nuclear tracks: imprinting structure on solids. *Rev. Mod. Phys.* **1983**, *55*, 907-948.
2. Apel, P. Y., Korchev, Y. E., Ziwy, Z., Spohr, R. & Yoshida, M. Diode-like single-ion track membrane prepared by electro-stopping. *Nucl. Instrum. Methods Phys. Rev. Sect. B* **2001**, *184*, 337-346.
3. Jirage, K. B., Hulteen, J. C. & Martin, C. R. Effect of thiol chemisorption on the transport properties of gold nanotubule membranes. *Anal. Chem.* **1999**, *71*, 4913-4918.
4. Maekawa, Y., Suzuki, Y., Maeyama, K., Yonezawa, N. & Yoshida, M. Chemical modification of the internal surfaces of cylindrical pores of submicrometer size in poly(ethylene terephthalate). *Langmuir* **2006**, *22*, 2832-2837.
5. Freund, J. E. & Walpole, R. E. *Mathematical Statistics* (Prentice-Hall, Englewood Cliffs, NJ, 1987).
6. Li, J., Stein, D., McMullan, C., Branton, D., Aziz, M. J. & Golovchenko, J. A. Ion-beam sculpting at nanometre length scales. *Nature* **2001**, *412*, 166-169.
7. Pai, J.-H., Wang, Y., Salazar, G. T., Sims, C. E., Bachman, M., Li, G. P. & Allbritton, N. L. Photoresist with low fluorescence for bioanalytical applications. *Anal. Chem.* **2007**, *79*, 8774-8780.

CHAPTER 5. A microchannel – nanopore device for bacterial chemotaxis assays.

5.1. Introduction to bacterial chemotaxis and prior art microfluidic assays.

Swimming bacteria sense changes in the concentration of chemicals in their environment and respond with distinct changes in swimming behavior. This process is termed chemotaxis and allows bacteria to bias the random walk of their motion in order to accumulate in favorable environments and disperse from less favorable environments. The flagellum-mediated motion of a bacterium alternates between straight runs, during which the flagellum (or flagella) rotates clockwise or counterclockwise depending the microorganism, and turns, during which the flagellum reverses its rotation direction.[1,2] Switching of flagellar rotation reorients the cell in a new direction and results in tumbles for most bacteria, such as *Escherichia coli,* or brief reversals in swimming direction for others, such as *Caulobacter crescentus*.[3] In *E. coli* and many other bacteria, binding of chemoattractant molecules to receptors on the cell surface suppresses flagellar switching, allowing the bacterium to travel up a chemical gradient toward higher attractant concentrations.[4,5]

The chemotactic ability of some bacteria has also been shown to help them approach and degrade toxic compounds in the environment,[6,7] and *C. crescentus* is a candidate of choice for bioremediation purposes. This microorganism is often found in nutrient-limited[8] and contaminated habitats[9,10] and is highly resistant to heavy metals such as uranium,[11] mercury,[12] zinc, copper, or cadmium.[13] *C. crescentus* has been engineered as a uranium biosensor[14] and for effective cadmium removal in water.[15] Development of

miniaturized instrumentation to assay for this behavior is appealing because the small volumes required limit the amount of hazardous material handled during the assay.

Microfluidic systems are well-suited to studies of bacterial chemotaxis because of their precise fluid handling and micrometer to millimeter length scale. Microchannel plumbing can readily establish reproducible and often complex chemical gradients in space and time,[16-18] and the size scale of typical microchannels allows researchers to track the paths of individual cells in a reasonable field of view. To date, several microfluidic platforms have been reported for studies of microbial chemotaxis,[19-26] aerotaxis,[27] and thermotaxis.[28] In two cases, results from microfluidic devices demonstrated an organism's sensitivity to chemoattractant concentrations several orders of magnitude below the detection limit identified with traditional assays.[19,20]

An additional benefit of microfluidic instrumentation is the relative rapidity of these assays compared to more traditional methods. Although the first study of chemotaxis in *C. crescentus* was published more than twenty years ago,[29] the exact biochemical mechanism and the full array of chemoattractants are still unknown. Microfluidic assays could be a tremendous resource in characterizing the chemotaxis pathway and a wide array of potential chemoattractants because gradients are rapidly established and chemotactic behavior observed in real-time. In contrast, traditional chemotactic assays require hours or days.[19,20]

Microfluidic devices designed for bacterial chemotaxis assays can generally be classified into two groups, those that rely on flow to develop a chemical gradient and those based solely on diffusion. Flow-based typically use a T-shaped intersection to introduce plain media or buffer from one branch and chemoattractant from the

other.[19,21,22] The two laminar streams meet at the T-intersection, and a gradient is established as chemoattractant diffuses laterally across the channel. Diffusive gradients may be created laterally,[23] as with the T-intersection, or axially,[20,24] and one class of diffusion-based devices uses a porous membrane to control mass transport of chemoattractant in the device. Two generations of a source-sink device have been demonstrated using a nitrocellulose membrane[25] and an agar film.[26] These chips consist of three parallel channels patterned in a porous substrate. The leftmost channel is filled with chemoattractant and acts as a source, and the rightmost channel is filled with buffer and acts as a sink. Diffusion of chemoattractant through a silicon nitride membrane has also been applied to studies of neutrophil chemotaxis. Chemoattractant diffuses from a lower chamber through 2 μm diameter holes in the membrane, creating point sources which attract the cells.[30]

Diffusion across a nanopore membrane is an attractive means of gradient formation because diffusive transport is based on a physical property of the analyte and is therefore stable and reproducible for a given temperature. Track-etch nanopore membranes have been used previously to control mass transport in microfluidic devices.[31,32] In this work, we demonstrate the potential for an integrated microchannel-nanopore device to screen for chemotaxis in *C. crescentus* by examining the trajectories of individual cells. The device design used is shown in Figure 1 and consisted of two poly(dimethylsiloxane) (PDMS) channels in separate device layers, placed orthogonally to one another and bridged by a commercially-available track-etch nanopore membrane. A diffusive "patch" of chemoattractant formed at the intersection as the test substance diffused from the sample channel into the cell channel through the nanopore membrane. Gradient formation

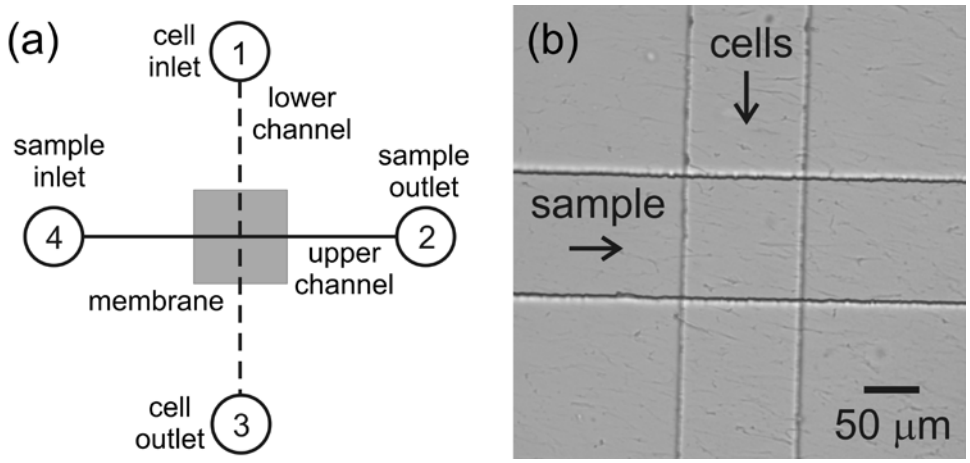

Figure 5-1. (a) Schematic of the microchannel-nanopore device. (b) White light image of the intersection of the two microchannels bridged by a track-etched membrane with 10 nm diameter pores. The vertical cell channel is in the lower layer, and the horizontal sample channel is in the upper layer.

in this device was characterized by fluorescence microscopy, and the design was validated by studying the response of wild type and a chemotaxis-impaired mutant of *C. crescentus* to a known chemoattractant, xylose.[29]

5.2. Methods.

Device fabrication. Multilayer microfluidic devices for the chemotaxis assays were assembled from poly(dimethylsiloxane) (PDMS) microchannels and polycarbonate track-etch nanopore membranes (GE Osmonics). SU-8 masters were prepared and characterized as described in Section A1. The masters consisted of a single straight line, 110 ± 2 μm wide, 19.1 ± 0.1 μm high, and 1 cm long. PDMS channels were cast from these masters and assembled with a polycarbonate track-etch membrane with 10 nm diameter cylindrical pores as described in Section A2. Prior to assembly the nanopore membrane was soaked in ethanol for 15 min to remove its hydrophilic polyvinylpyrrolidone coating; this step was required to eliminate visible wetting of the membrane outside the microchannels. The pore density of $6 \times 10^8/cm^2$ resulted in an average pore-to-pore spacing of 0.4 μm, 72600 ± 270 pores at the intersection, and a porosity of 0.05%. Four 6.2 mm tall, 4 mm i.d. glass reservoirs were affixed over the access holes using a small amount of PDMS as adhesive, and the assembled device was allowed to cure completely at room temperature overnight.

***C. crescentus* Strain Construction and Labeling.** Genome analysis reveals that there are two different chemotaxis operons in *C. crescentus* CB15,[33] from gene CC428 to CC0441 and from gene CC0588 to CC0598. However, only the former has been characterized previously and has been qualified as a "major chemotaxis operon."[3,29,34]

Collaborators in the Brun laboratory (Dept. of Biology, Indiana University) constructed two different mutant strains in each *cheA* of these two operons (genes CC0433 and CC0594), as well as a double mutant of both *cheA* genes to determine their involvement in the chemotactic response of *C. crescentus* to xylose. The clean in-frame deletions of these *cheA* genes were carried out by homologous recombination as previously described.[35] Results of agar swarm plate assays showed that only mutants in *cheA* CC0433 seemed to be impaired in chemotaxis, and therefore the rest of our studies focused on the behavior of the Δ*cheA* CC0433 and the wild type strains.

The two *C. crescentus* strains used in the microfluidic devices were labeled using green fluorescent protein (GFP). Stable insertions of a miniTn*7-gfp* transposon[36] constitutively expressing GFP into the chromosome of each strain were performed by ϕCr30 mediated transduction[37] of the miniTn*7-gfp* from *C. crescentus* AS110[38] into *C. crescentus* CB15 wild type (YB135) and CB15 Δ*cheA* CC0433 (YB4643) to give the GFP-labeled strains *C. crescentus* CB15 WT (YB4789) and CB15 Δ*cheA* (YB5097) used in this work.

Cell culturing and swarmer enrichment. *C. crescentus* has a dimorphic life cycle (Figure 5-2) in which cell division gives rise to two genetically identical but morphologically distinct daughter cells: a non-motile stalked cell capable of cell division and a non-reproductive motile swarmer cell with a single polar flagellum and pili. Because only motile cells are capable of chemotaxis, cultures for these experiments were enriched in swarmer cells using a modified plate releasing technique.[39]

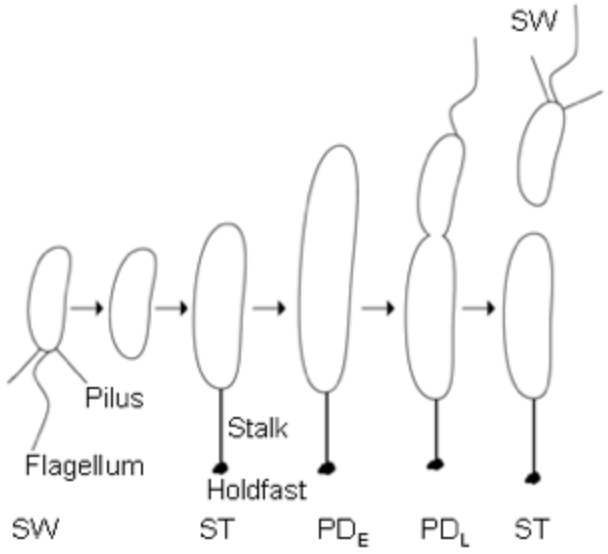

Figure 5-2. Schematic of the *Caulobacter crescentus* life cycle. A swarmer cell (SW) has a flagellum and is motile. Long, thin filaments called pili are located at the same pole and are involved in adhesion of the swarmer cell to surfaces. As the swarmer cell matures, it loses its flagellum, retracts the pili, and develops a stalk at the pole. The stalked cell (ST) produces holdfast, a sticky material at the end of the stalk, which allows the mature stalked cell to adhere permanently to surfaces in favorable environments and form a biofilm. The stalked cell elongates to become an early predivisional cell (PD_E). The late predivisional cell (PD_L) begins constriction and divides to produce two distinct daughter cells, a newborn swarmer cell (SW) and a stalked cell (ST). For these experiments, newborn swarmer cells were collected following release from a biofilm of adhered stalked cells.

Cells were grown overnight in 10 mL of minimal M2 medium supplemented with 0.2% glucose (M2G) at 30 °C with shaking. M2 consists of 12.3 mM Na_2HPO_4, 7.8 mM KH_2PO_4, 9.3 mM NH_4Cl, 0.5 mM $MgSO_4$, 0.5 mM $CaCl_2$, 8 μM EDTA, and 10 μM $FeSO_4 \cdot 7H_2O$.[40] The overnight culture was diluted to an OD_{600} of ~0.1, placed in a sterile 150 mm polystyrene Petri dish, and incubated at room temperature for 16 h (wild type) or 40 h (Δ*cheA* mutant) on a lateral platform shaker at 50 rpm. The increased incubation time for the Δ*cheA* mutant allowed for robust monolayer biofilm formation despite a delay in the initiation of biofilm formation. At the end of this incubation period, the medium was removed from the Petri dish, and the biofilm formed in the Petri dish was thoroughly rinsed with sterile distilled water to remove any unattached cells. Fresh M2G medium (50 mL) was added to the dish, and incubation continued for 4 more hours under the same conditions. Immediately prior to swarmer collection, the plate was rinsed thoroughly with warm (30 °C), oxygenated M2G. A 1 mL aliquot of M2G was then added to the plate, which was placed on a rocker for 5 min. During this 5 min interval newborn swarmer cells were released into the medium. Typically, the enriched culture consisted of 80-95% swarmer cells, which were collected and concentrated by centrifugation at 5000× g for 5 min at 4 °C to a final volume of 100 μL. The cell suspension was kept on ice until the cells were loaded into the microfluidic device.

Chemotaxis assays. Appropriate flow conditions were established by filling the reservoirs with 85, 90, 95 and 100 μL of M2G, starting with the cell outlet (reservoir 3) and proceeding counterclockwise around the device to the sample inlet (reservoir 4). M2G spiked with 10 μM 8-methoxypyrene-1,3,5-trisulfonic acid (MPTS; Sigma-Aldrich) was added to the sample inlet reservoir as a fluorescent tracer. Approximately 5 μL of

concentrated, enriched swarmer cells, prepared as described above, were added to the cell inlet (reservoir 1), and the reservoir levels were adjusted to achieve a flow rate of ~25 μm/s in the cell channel.

An inverted optical microscope (TE-2000U, Nikon, Inc.) equipped for epifluorescence, a CCD camera (9100-13, Hamamatsu Corp.), and IPLab software (BD Biosciences) were used to monitor individual swarmer cells for the chemotaxis assays. FITC and coumarin filter cubes (96320M and 31047v2, Nikon, Inc.) were used to obtain the GFP and MPTS fluorescence signals, respectively. Video data were recorded by streaming 301 frames at a frame rate of 10.9 - 13.9 fps. As a control, videos of cell swimming were recorded in the absence of chemoattractant in the sample channel. After the baseline cell swimming behavior was established, the contents of the sample inlet (reservoir 4) were replaced with a solution of the chemoattractant, xylose, and 10 μM MPTS in M2G. Xylose concentrations of 1.3 μM, 1.3 0μM, 1.3 mM, and 1.3 M were tested. These concentrations corresponded to orders of magnitude variations of the xylose concentration typically used for cell culture, 0.2% (13 mM). The MPTS fluorescence signal at the intersection was checked before and after replacing the sample solution to ensure no major change occurred in the gradient. After allowing a minimum of 2 min for the gradient to form, videos were obtained of the cell response to the chemoattractant.

Data analysis. A combination of freely-available ImageJ software and custom-written MATLAB programs (The MathWorks, Inc.) was used to analyze the video data. The ParticleTracker plug-in[41] for Image J was used to obtain trajectory coordinates for each cell. This plug-in required five input parameters to determine the cell trajectories: radius, cut-off, intensity percentile, displacement, and link range. Radius refers to the

size, in pixels, of a single cell and was set to 5 for all videos. The cut-off value discriminates against aggregates on the basis of their 0^{th} and 2^{nd} intensity moments. No aggregates were observed in these experiments, and this value was set to 0 for all analyses. The intensity percentile varied from 0.05% to 1.2%, meaning that particles in the top 0.05% to 1.2% of the intensity range for a given video were identified as cells. This value varied depending on background intensity, cell density, and the presence of adhered cells in the field of view. Displacement refers to the maximum number of pixels a cell can travel between frames and was set to 12-15. The link range is the number of subsequent frames the plug-in examines to find a cell's next position. For example, a link range of 1 means that a cell identified in frame 1 must be found in frame 2 for the trajectory to continue. A link range of 2 means that a cell identified in frame 1 could go unidentified in frame 2, perhaps because the cell had gone out of the focal plane, but be identified in frame 3. Link ranges of 1-3 were used in these analyses, and any trajectories containing spurious links were readily identified and deleted.

A custom MATLAB program was used to extract the relevant statistics about cell motion from the trajectories. To improve data quality, this program first disregarded all trajectories < 100 μm long or for which cell position deviated less than 5 μm from the starting point (i.e., adhered cells). Trajectories were then discriminated as arising from either swimming or non-swimming (dead or non-motile stalked) cells. Cells were identified as non-swimming if ≥ 95% of the total accumulated distance trav eled was in the direction of flow. These trajectories were used to determine the flow rate. Cell trajectories with ≤ 90% of motion in the direction of flow were analyzed as swimming cells, and all trajectories for which 90% to 95% of cell motion was with the flow were not

considered because of difficulty determining which of these tracks corresponded to non-swimming cells and which to swimming cells following the channel wall.

For swimming cell trajectories, the MATLAB program determined the length and duration of each run nested between two turns. To identify turns, the angle formed by each triplet of consecutive points was calculated. A point in the trajectory was considered a turn when the difference between two consecutive angles was $\geq 90^\circ$. Ignoring points where the change in angle with time was $< 90^\circ$ eliminated identification of circling paths as strings of turns. Bacteria follow circular paths when in close proximity to a surface,[42,43] and this behavior was frequently observed during these experiments. Because the chemoattractant concentration in the cell channel was highest at the membrane surface, cell circling may reflect chemotaxis. Future work will investigate whether an increase in circular swim patterns is correlated with the presence of chemoattractant.

C. crescentus swarmer cells have long, thin filaments called pili at their flagellar pole which are involved in cell adhesion to surfaces (see Figure 5-2).[44,45] In these experiments, cells occasionally adhered to the channel, spun around their flagella, released from the surface, and swam away in another direction. Chemotaxis is indicated by a change in direction caused by reversal of the flagellum motor,[4] so to avoid identifying changes in swim direction after release from a surface as turns, cells were required to travel at least 1 μm away from a turn location within 4 frames of the turn. Otherwise, that point was identified as a "false turn" where the cell temporarily adhered to the channel and was not used in any run length or duration calculations.

5.3. Results and discussion.

Gradient tracking with MPTS. Gradient formation and stability were monitored using MPTS, a blue fluorescent, pyrene-based dye with a net charge of -3, which prevented the dye from adsorbing into the PDMS channels. Using this blue dye instead of the more commonly used fluorescein allowed us to track the gradient in real-time during experiments without obscuring the GFP signal from the bacterial cells. Because we found no literature reports of MPTS used in cell-based assays, we conducted agar plate studies which confirmed that MPTS was not cytotoxic, could not be used by *C. crescentus* as a carbon source, and did not interfere with chemotaxis toward xylose (data not shown).

Figure 5-3a shows a fluorescence image of the device intersection with the sample channel filled with 10 μM MPTS in M2G and the cell channel with M2G. The line profile shows the average, background-subtracted fluorescence signal in the cell channel, indicating the patch of chemoattractant encountered by cells at the intersection. While the xylose concentration could not be imaged directly, the diffusion coefficient of MPTS, estimated as 3.3×10^{-6} cm^2/s (that of the hydroxyl analogue, 8-hydroxypyrene-1,3,5-trisulfonic acid)[46] is approximately 45% that of xylose, making MPTS a reasonably good tracer for xylose diffusion.

Gradient formation. Figure 5-3b shows plots of fluorescence versus time for the sample channel and at the intersection for 30 min immediately following introduction of MPTS solution to the sample inlet (reservoir 4). Gradient formation occurred within 30 s after placing the dye solution in the reservoir with the majority of the lag due to the time required for hydrostatic flow to bring solution from the reservoir to the intersection. Once sample solution reached the intersection, we estimate that < 0.5 s was required for xylose

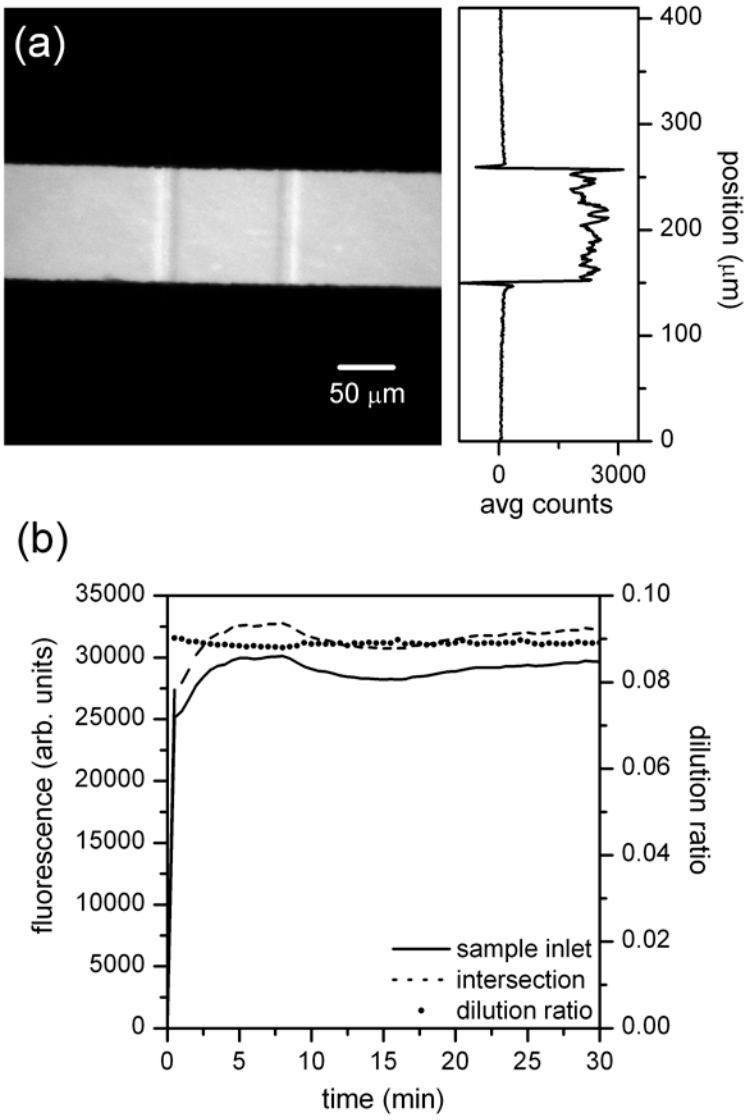

Figure 5-3. (a) Fluorescence image of MPTS at the microchannel intersection. The horizontal sample channel was filled with 10 μM MPTS in M2G, and the vertical cell channel was filled with M2G without dye. The line profile to the right shows the average fluorescence along the length of the cell channel, with the background fluorescence from the membrane and sample channel subtracted. (b) Plots of fluorescence versus time for the sample inlet (solid line) and intersection (dashed line) starting with introduction of the MPTS solution in the sample inlet (reservoir 4) and continuing for 30 min. The background auto-fluorescence of the membrane has been subtracted from both traces. The secondary y-axis shows the dilution ratio: the fluorescence at the intersection in the cell channel (sample channel fluorescence subtracted) divided by the fluorescence in the sample channel.

to penetrate the cell channel depth, based on a bulk diffusion coefficient, D_{xylose},[47] of 7.5 × 10^{-6} cm^2/s and a total diffusion distance of 25 μm (6 μm membrane thickness plus 19 μm channel depth). The ratio of solute to nanopore radius was 0.065,[48] meaning that the apparent diffusion coefficient of xylose through the membrane should be roughly 90% of the bulk diffusion coefficient and contributions of steric hindrance to diffusive transport through the membrane were minimal.[49] While hindered diffusion was likely negligible for a small molecule chemoattractant such as xylose, this effect should be considered when choosing nanopore dimensions for larger putative attractants, e.g., peptides.

Gradient stability. In this integrated microchannel-nanopore device, gradient formation was based on diffusion of chemoattractant through the nanopores. Because the volumetric flow rate from hydrostatic transport scales as the fourth power of the pore radius,[50] decreasing pore diameter dramatically decreases hydrostatic transport through the membrane. For a typical transmembrane pressure of ~1 mm H_2O, we estimate a volumetric flow rate through the membrane of ~20 aL/s into a total intersection volume of 230 pL and a microchannel volumetric flow rate of ~50 pL/s. For 10 nm diameter pores, therefore, hydrostatic flow across the membrane was minimal, and transfer of chemoattractant into the cell channel was controlled primarily by diffusion, rather than by the flow rate, transmembrane pressure, or other operating parameters.

The amount of material transferred across the membrane and into the cell channel was estimated from the fluorescence at the intersection relative to the sample channel fluorescence. Figure 5-3b includes a plot of the dilution ratio (solid black circles, secondary y-axis), which was calculated according to Equation 5.1,

$$dilution\ ratio = \frac{s_{int} - s_{sample}}{s_{sample} - b} \tag{5.1}$$

where s_{int} was the fluorescence signal at the intersection, s_{sample} was the fluorescence in the sample channel, and b was background from membrane auto-fluorescence. The average dilution ratio for 29 devices was 0.09 ± 0.01. Experiments in which a microchannel-nanopore device was filled with varying concentrations of MPTS confirmed that the fluorescence signal was linear with concentration (R^2 = 0.996). We therefore estimate that the average MPTS concentration in the cell channel was approximately 9% of that in the sample channel.

For constant fluid levels in the reservoirs, the dilution ratio was extremely stable, with a relative standard deviation (RSD) of ~0.5% over 30 min. Exchange of the solution in the sample inlet (reservoir 4) during the course of an experiment increased the deviation in the dilution ratio to a RSD of ~13% over 0.5 – 1 h. The RSD for the average dilution ratio was ~16% for n = 29 devices, indicating good repeatability from device to device. Similar devices constructed with membranes containing 50 nm, 1 μm, and 2 μm diameter pores were more susceptible to variation in pressure across the membrane and showed considerably more variability in sample transport over time and from device to device.

Cell swimming in the device. Conditions in the microchannel-nanopore device were chosen to maintain cell viability and motility. The PDMS substrates were only ~1.5 mm thick to allow gas exchange through the PDMS. This permitted the strictly aerobic cells to survive long term in the microchannels; in fact, cell growth and motility can persist for up to 24 h within the microfluidic device. For the chemotaxis and motility studies, the swarmer cells were collected and assayed in their growth medium, M2G, which contained glucose as a carbon source. Finally, gentle hydrostatic flow rates between 15 –

30 μm/s were used so that the *C. crescentus* swarmer cells could easily swim upstream and control their position within the channel.

Figure 5-4 shows representative results for the cell video data, cell tracking plug-in, and MATLAB trajectory analysis. Figure 5-4a shows a composite fluorescence image in which each pixel shown is the maximum value recorded at that position during the video. The distance traveled between frames was much greater for swarmers than for non-swimming cells (straight, bright streaks), demonstrating that the average cell velocity was substantially greater than the flow rate. Figure 5-4b shows the results of the ParticleTracker plug-in for this video with individual trajectories shown in different colors. The similarity of the streaks in Figure 5-4a and the trajectories in Figure 5-4b demonstrate the accuracy of the tracking software. Figure 5-4c shows a MATLAB plot of the white trajectory in Figure 5-4b. A green dot marks the start of the trajectory, a red dot marks the end, and blue dots indicate turns identified by the MATLAB program. This trajectory in particular demonstrates the circular swim patterns followed by some cells and the ability of the program to discriminate this motion from a series of abrupt turns.

Data were collected on several days, and the lengths and durations of all runs were compiled. For each strain and condition, between 162 and 1161 trajectories were analyzed. Of these, ~40% contained at least one run nested between two turns, and the compiled data for each condition included between n = 143 and n = 1050 runs. A summary of the number of runs and average length and duration for each condition is given in Tables 5-1 and 5-2. Due to the large variation in run length and duration and the skew of the data, we have chosen to present the results as histograms, seen in Figure 5-5.

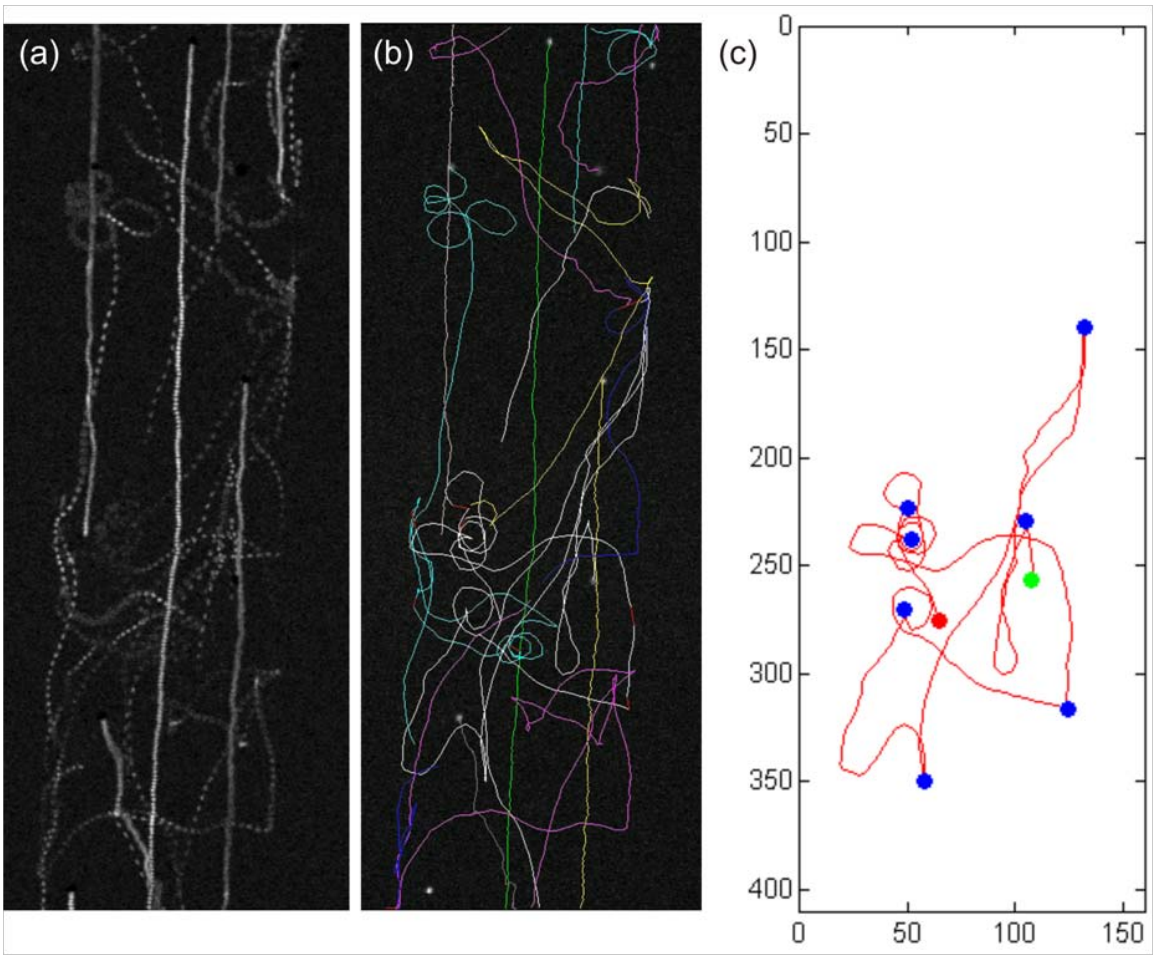

Figure 5-4. (a) A composite fluorescence image of cells in the device obtained using the brightest pixel at each location during a 301 frame video. (b) Trajectories identified by the ParticleTracker plug-in for ImageJ for the video data shown in (a). (c) A MATLAB plot of the white trajectory from (b) with the start, end, and turn locations identified with green, red, and blue dots, respectively. The axis labels in (c) are in micrometers, and the scale is the same for all panels.

Table 5-1. Summary of run length and duration data for the wild type cells (CB15).

Condition	No. Trajectories	No. Traj. w/ Nested Runs	No. Runs	Average		Log-Transformed	
				Length (μm)	Duration (s)	Length	Duration
control	1161	487	1050	68 ± 75	2.0 ± 1.9	1.55 ± 0.56	0.135 ± 0.372
0 μM	228	93	181	63 ± 64	1.8 ± 1.5	1.53 ± 0.56	0.125 ± 0.355
1.3 μM	278	98	143	54 ± 58	1.6 ± 1.2	1.47 ± 0.53	0.090 ± 0.325
130 μM	430	147	259	42 ± 51	1.5 ± 1.4	1.45 ± 0.47	0.053 ± 0.319
13 mM	869	348	771	44 ± 57	1.7 ± 1.6	1.36 ± 0.52	0.084 ± 0.335
1.3 M	162	89	255	55 ± 66	1.5 ± 1.4	1.41 ± 0.58	0.039 ± 0.342

Table 5-2. Summary of run length and duration data for the chemotaxis-impaired mutant (CB15Δ*cheA*).

Condition	No. Trajectories	No. Traj. w/ Nested Runs	No. Runs	Average		Log-Transformed	
				Length (μm)	Duration (s)	Length	Duration
control	677	292	644	41 ± 48	1.4 ± 1.4	1.31 ± 0.31	-0.001 ± 0.124
130 μM	678	299	573	42 ± 57	1.3 ± 1.3	1.35 ± 0.27	-0.031 ± 0.110
13 mM	422	187	581	37 ± 43	1.4 ± 1.4	1.28 ± 0.28	0.003 ± 0.117
1.3 M	361	167	338	47 ± 58	1.4 ± 1.3	1.36 ± 0.32	0.015 ± 0.120

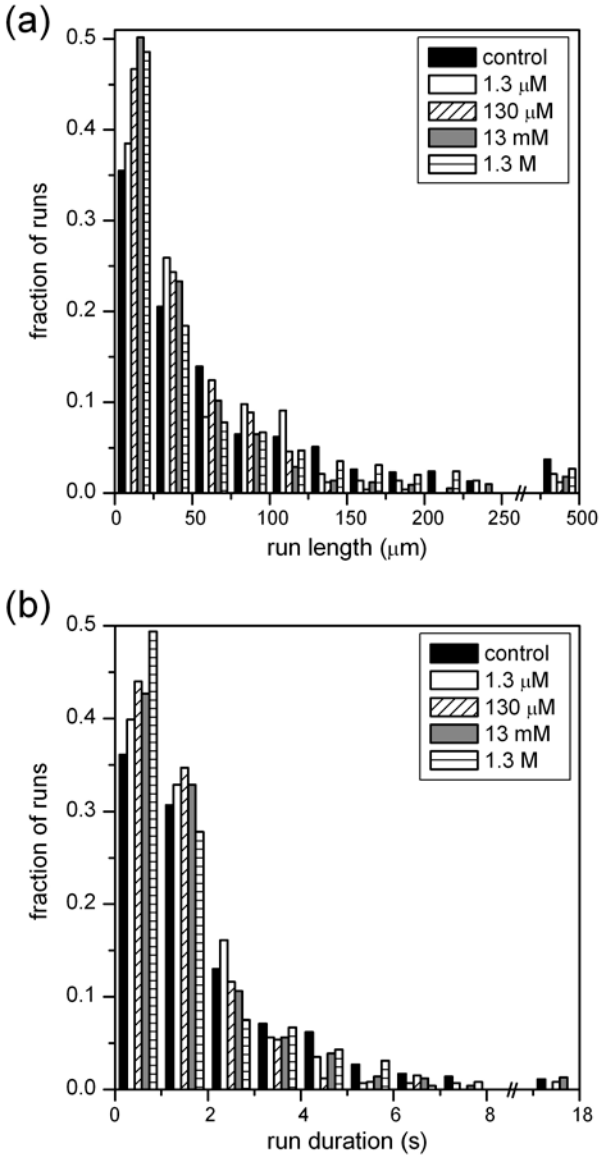

Figure 5-5. Histograms for the wild type cells of (a) run length and (b) run duration distributions for a control, in which the sample channel was filled with M2G, and for xylose concentrations of 1.3 µM, 130 µM, 13 mM, and 1.3 M. For both run length and duration, the 130 µM, 13 mM, and 1.3 M xylose concentrations were statistically different from the control. Note breaks in x-axes: the last bin contains runs with 250 µm < length ≤ 500 µm in (a) and 8 s < duration ≤ 18 s in (b).

Both the run length and run duration distributions have maxima at the minimum bin values and tail at higher values.

Chemotaxis assays with wild type cells. For the wild type cells, the average run length and run duration were 68 μm and 2.0 s, respectively, in the absence of a xylose gradient (see Table 5-1). The turn frequency observed in these experiments was higher than previously reported for *C. crescentus*; for example, one literature report gives an average of ~0.5 turn every 5 s.[29] Previous work has shown that confinement in micrometer-scale channels affects cell motion in *E. coli*,[51,52] and for the experiments reported here, a number of turns occurred when a cell approached the channel wall and then changed direction. This effect may have increased the turn frequency observed.

The distributions of run length and duration for a given xylose concentration are similarly shaped, and the average cell velocity during the runs, ~30 μm/s, was fairly constant with xylose concentration. This suggests than any changes in cell motion with xylose concentration were not due to chemokinesis, a non-directional change in cell motion or velocity in response to a chemical stimulus, which has been observed in closely related bacteria.[53-55]

In the presence of a xylose gradient, the proportion of short ($\leq$ 25 μm and $\leq$ 1 s) runs increased. This is evident in the normalized histograms in Figure 5-5 as increased values in the minimum bins for the xylose-treated runs compared to the control. This is indicative of a chemotactic response as the cells increased the number of rapid course corrections to stay near the patch of xylose at the intersection. The intersection was 110 μm of the 410 μm long field of view, so runs much longer than 110 μm would likely move a cell down the concentration gradient. Because movement down a chemoattractant

gradient increases turn frequency,[4] we would expect the presence of a xylose gradient at the intersection to decrease the proportion of longer runs, as observed. To control for the effects of time spent in the device and the exchange of reservoir contents, experiments were performed in which the sample reservoir was refilled with fresh M2G rather than a xylose solution. These experiments showed no significant change in cell behavior induced by the time spent in the device or the exchange of reservoir contents (unpaired t-tests, $p = 0.75$ for length and 0.76 for duration; data not shown).

To determine whether the change in behavior with xylose treatment seen in Figure 5-5 was statistically significant, a one-way analysis of variance (ANOVA) and a Tukey means comparison were performed in OriginPro 8.0 (OriginLab Corp.). Prior to these statistical analyses, all the data were log-transformed to compensate for the right skew. The ANOVAs showed a statistical difference between the means ($p = 2.1 \times 10^{-11}$ for length and 4.9×10^{-5} for duration), and the means comparison test established that the three highest xylose concentrations tested (130 µM, 13 mM, and 1.3 M) were each statistically different from the control, while the lowest xylose concentration (1.3 µM) was not. The sensitivity of this assay depends on both the response of *C. crescentus* to a given concentration and gradient and on the quantity of data taken. The inherent variability in run length and duration means that many observations are required to detect small changes in behavior. As a result, the absence of a significant difference between the 1.3 µM xylose treatment and the control could occur because of an absence of chemotactic behavior or because a larger number of runs must be measured to detect an effect at this concentration.

Interestingly, statistically significant differences were not observed between the different xylose concentrations, and the histograms in Figure 5-5 show similar changes in swimming behavior for concentrations spanning four orders of magnitude (130 μM to 1.3 M). Bacterial chemotaxis is robust across a wide range of chemoattractant concentrations because of regulatory feedback based on methylation of the chemoreceptors.[5] As a result, cells respond sensitively to the relative steepness of a chemical gradient rather than to the absolute concentration at their location, and an absence of correlation between xylose concentration and swimming behavior is not unexpected if the gradient is similarly shaped for all concentrations. Because the chemical gradient in the microchannel-nanopore device was established along the z-axis and therefore out of the device plane, imaging the gradient directly by epifluorescence was not possible. However, the MPTS data, including Figure 5-3, suggest that material transport in the device was similar over a broad concentration range.

Chemotaxis and motility assays of the Δ*cheA* mutant. The swimming behavior of a chemotaxis-impaired mutant, CB15Δ*cheA*, was also examined as a control. In all bacteria and archae, chemotaxis is regulated by the two-component system CheA-CheY. The CheA protein is a histidine kinase whose phosphorylation state is impacted by interactions with the cytoplasmic end of chemoreceptors, and CheY is the response regulator that transduces the signal to the flagellum and alters its rotation. Deletion of *cheA* allows chemoattractant binding to the receptor outside the cell to occur, but abolishes the subsequent switching of flagellum motor rotation and therefore should impair chemotaxis toward all attractants.[4,5]

Indeed, as seen in Figure 5-6, the chemotaxis-impaired cells showed no significant change in either run length or run duration in the presence of 130 µM, 13 mM, or 1.3 M xylose (one-way ANOVA p-values = 0.11 for length and 0.18 for duration), and a two-way ANOVA demonstrated a statistically significant difference between the wild type response and the mutant response to xylose (interaction p-value = 5.7×10^{-6} for length and 6.1×10^{-3} for duration).

Interestingly, the baseline cell swimming behavior for the Δ*cheA* strain differed markedly from that of the wild type cells. The chemotaxis-impaired cells had an average run length of 41 µm and an average run duration of 1.4 s, compared to 68 µm and 2.0 s for the wild type cells. Figure 5-7 shows histograms of run length and run duration for the wild type and chemotaxis-impaired cells. Similarly to the xylose-treated wild type cells, the chemotaxis-impaired mutant shows a high proportion of short runs compared to the wild type control. In fact, the Δ*cheA* mutant exhibited shorter runs than did the xylose-treated wild type cells, which had average run lengths and durations ranging from 42-55 µm and 1.5-1.7 s, respectively (see Table 5-1).

The mechanism of bacterial chemotaxis is best understood in *E. coli*, a Gram negative bacterium with peritrichous flagella.[4,5] In *E. coli,* a *cheA* deletion promotes straight swimming by reducing the frequency of changes in direction of flagellar rotation.[5] Likewise, a *cheA* deletion in *Vibrio cholerae*, a Gram negative bacterium which has a bidirectional monopolar flagellum, causes smooth swimming by reducing the frequency of flagellum motor switching.[56,57] Similarly, in Gram negative bacteria with a unidirectional monopolar flagellum, such as *Rhodobacter sphaeroides*[58] and *Sinorhizobium meliloti*,[59] a *cheA* deletion also results in a smooth swimming phenotype

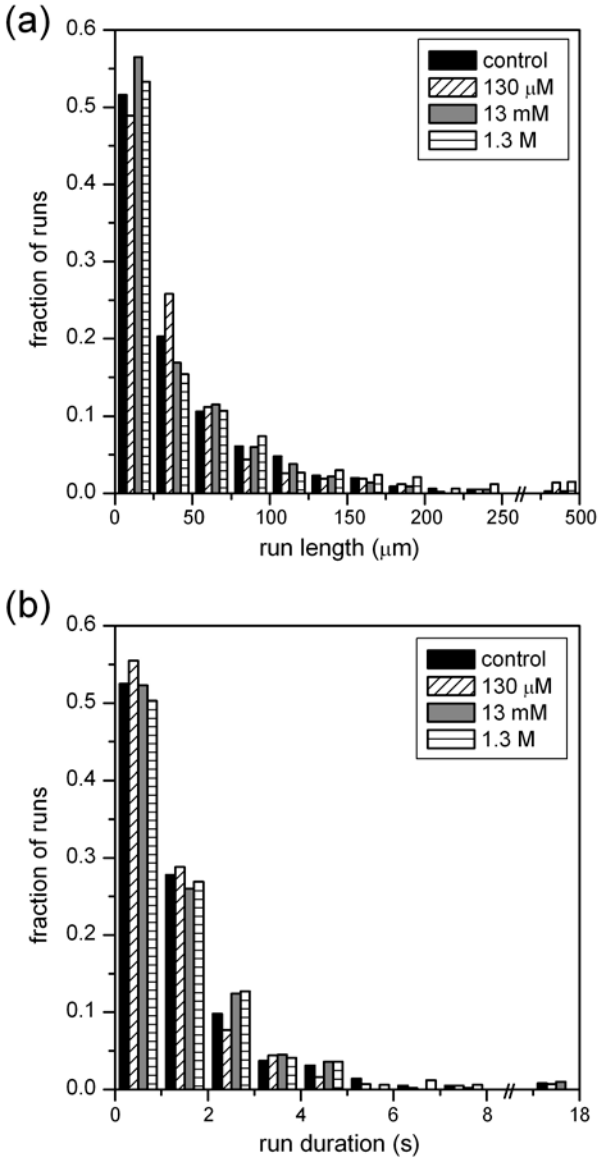

Figure 5-6. Histograms of (a) run length and (b) run duration for the chemotaxis-impaired mutant, CB15Δ*cheA*, in the presence of M2G (control) and 130 μM, 13 mM, and 1.3 M xylose in M2G. No statistically significant differences in either run length or run duration were observed.

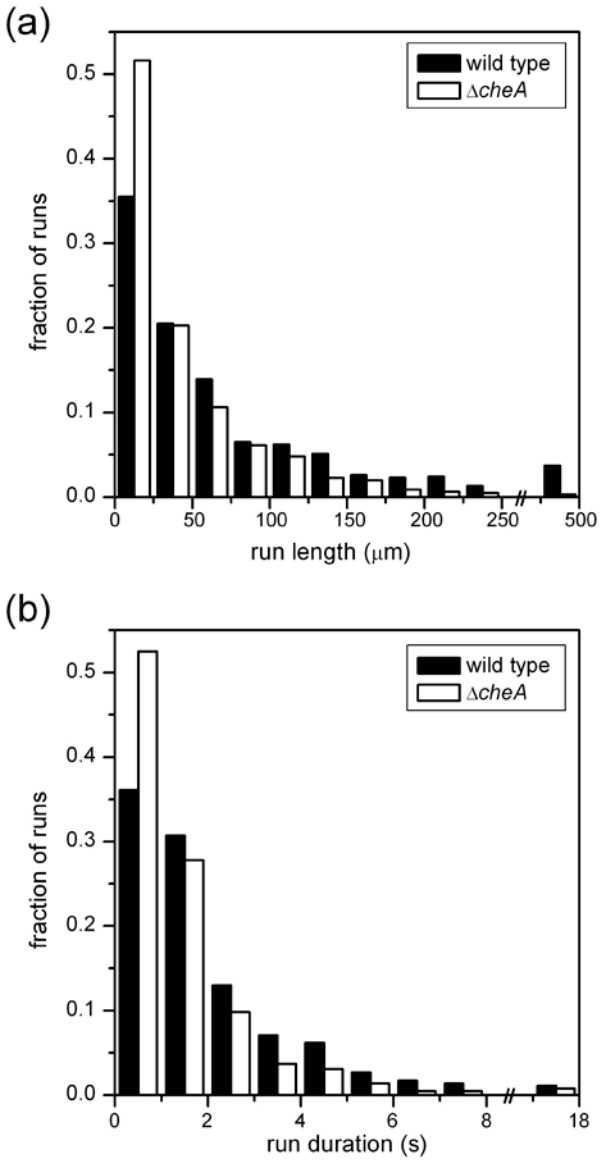

Figure 5-7. Histograms of (a) run length and (b) run duration distributions for wild type cells and for a chemotaxis-impaired mutant (Δ*cheA* in the legend). In both cases the sample channel was filled with M2G. Note breaks in x-axes: the last bin contains runs with 250 μm < length ≤ 500 μm in (a) and 8 s < duration ≤ 18 s in (b).

by reducing the frequency of stops in flagellum rotation. In contrast, in the Gram positive bacterium *Bacillus subtilus,* which has peritrichous flagella, a *cheA* deletion has been observed to increase the frequency of flagellum motor switches.[2,60]

The data in Figure 5-7 indicate that deletion of *cheA* in *C. crescentus* causes an increase in the frequency of switching of the flagellum motor. This observation is surprising given that *C. crescentus* is a Gram negative bacterium, is closely related to both *R. sphaerodies* and *S. meliloti* based on phylogeny, has a bidirectional monopolar flagellum similar to that which powers *V. cholerae* motility, and is only distantly related to *B. subtilis*. This intriguing observation suggests the mechanism underlying chemotaxis in *C. crescentus* may be quite different from what has been previously reported among the Gram negative bacteria. Further genetic and biochemical characterization of the major *C. crescentus* chemotaxis system will be required to evaluate these differences and elucidate both the mechanism and the evolution of chemotaxis in this bacterium.

5.4. Conclusions and future directions.

The observation that the wild type and Δ*cheA* strains exhibit different baseline swimming patterns demonstrates the utility of microfluidic platforms to studies of bacterial motility in general. The micrometer to millimeter dimensions of microchannels matches well with a microscopic field of view and allows individual cells to be monitored over useful time scales (in this case, 10s of seconds). The macroscopic measurements used in some traditional chemotaxis assays[61,62] would not have reflected this difference in the microscopic behavior of the cells.

Analyses of run length and duration for wild type *C. crescentus* swarmer cells found that the proportion of short runs increased with the presence of a chemoattractant, xylose, at the intersection. While traditional chemotaxis assays typically measure an increase in run length and duration as cells move up a concentration gradient, the results of these experiments are likely due to the small size of the intersection relative to the field of view. We suspect that runs were shorter in the presence of chemoattractant because we mostly observed cells making rapid course corrections to return to the intersection, rather than observing cells moving up the chemical gradient. Measurement of individual cell trajectories also revealed that the Δ*cheA* mutant had shorter runs than the wild type. Observation of this behavior requires an assay which measures cell trajectories individually, and the microfluidic platform used for these assays facilitates such measurements.

These results demonstrate the effectiveness of track-etch nanopore membranes in controlling diffusive mass transport within a microfluidic device. Diffusion of chemoattractant through 10 nm diameter pores at the intersection of two orthogonal microfluidic channels rapidly produces a stable and reproducible gradient. Additionally, the nanopore membranes in these devices are commercially available, the fabrication methods used are inexpensive, and operation of the device is straightforward, requiring no pumps or valves. These advantages should help to make these devices more accessible to non-specialists. On the other hand, more complex fabrication methods could be used to improve this design. For example, planar devices, in which the nanochannel connections between the sample and cell channels are in the plane of the device (e.g., see Chapter 3),

would generate a gradient laterally across the width of the cell channel and permit monitoring of the gradient by epifluorescence.

As noted above, literature reports indicate that confinement in micrometer-scale channels affects motility in *E. coli*.[51,52] As a complement to the studies presented in this chapter, the Jacobson laboratory is currently investigating the effects of microchannel dimensions and flow rate on cell motion in *C. crescentus*. The results of these experiments will improve device design in future generations of microfluidic devices for chemotaxis assays.

5.5. References.

1. Rao, C. V. & Ordal, G. W. The three adaptation systems of *Bacillus subtilis* chemotaxis. *Trends Microbiol.* **2008**, *16,* 408-487.
2. Szurmant, H. & Ordal, G. W. Diversity in chemotaxis mechanisms among the bacteria and archaea. *Microbiol. Mol. Biol. Rev.* **2004**, *68,* 301-319.
3. Alley, M. R. K., Gomes, S. L., Alexander, W. & Shapiro, L. Genetic analysis of a temporally transcribed chemotaxis gene cluster *Caulobacter crescentus*. *Genetics* **1991**, *129,* 333-342.
4. Stock, J. B. & Surette, M. G. in *Escherichia coli and Salmonella typhimurium: Cellular and molecular biology* (ed. Neidhardt) 1103-1129 (ASM Press, Washington, DC, 1996).
5. Baker, M. D., Wolanin, P. M. & Stock, J. B. Systems biology of bacterial chemotaxis. *Curr. Opin. Microbiol.* **2006**, *9,* 187-192.
6. Pandey, G. & Jain, R. K. Bacterial chemotaxis toward environmental pollutants: role in bioremediation. *Appl. Environ. Microbiol.* **2002**, *68,* 5789-5795.
7. Parales, R. E. & Harwood, C. S. Bacterial chemotaxis to pollutants and plant-derived aromatic molecules. *Curr. Opin. Microbiol.* **2002**, *5,* 266-273.
8. Poindexter, J. S. Biological properties and classification of the Caulobacter group. *Bacteriol. Rev.* **1964**, *28,* 231-295.
9. Inagaki, F., Takai, K., Hirayama, H., Yamato, Y., Nealson, K. H. & Horikoshi, K. Distribution and phylogenetic diversity of the subsurface microbial community in a Japanese epithermal gold mine. *Extremophiles* **2003**, *7,* 307-317.
10. Mannisto, M. K., Tiirola, M. A., Salkinoja-Salonen, M. S., Kulomaa, M. S. & Puhakka, J. A. Diversity of chlorophenol-degrading bacteria isolated from contaminated boreal groundwater. *Arch. Microbiol.* **1999**, *171,* 189-197.

11. Hu, P., Brodie, E. L., Suzuki, Y., McAdams, H. H. & Andersen, G. L. Whole-genome transcriptional analysis of heavy metal stresses in *Caulobacter crescentus*. *J. Bacteriol.* **2005**, *187,* 8437-8449.
12. Ji, G. Y., Salzberg, S. P. & Silver, S. Cell-free mercury volatilization activity from three marine *Caulobacter* strains. *Appl. Environ. Microbiol.* **1989**, *55,* 523-525.
13. Braz, V. S. & Marques, M. V. Genes involved in cadmium resistance in *Caulobacter crescentus*. *FEMS Microbiol. Lett.* **2005**, *251,* 289-295.
14. Hillson, N. J., Hu, P., Andersen, G. L. & Shapiro, L. *Caulobacter crescentus* as a whole-cell uranium biosensor. *Appl. Environ. Microbiol.* **2007**, *73,* 7615-7621.
15. Patel, J., Zhang, Q., McKay, R. M. L., Vincent, R. & Xu, Z. Genetic engineering of *Caulobacter crescentus* for removal of cadmium from water. *Appl. Biochem. Biotechnol.* **2009**doi 10.1007/s12010-009-8540-0.
16. Jacobson, S. C., McKnight, T. E. & Ramsey, J. M. Microfluidic devices for electrokinetically driven parallel and serial mixing. *Anal. Chem.* **1999**, *71,* 4455-4459.
17. Dertinger, S. K. W., Chiu, D. T., Jeon, N. L. & Whitesides, G. M. Generation of gradients having complex shapes using microfluidic networks. *Anal. Chem.* **2001**, *73,* 1240-1246.
18. Amarie, D., Glazier, J. A. & Jacobson, S. C. Compact microfluidic structures for generating spatial and temporal gradients. *Anal. Chem.* **2007**, *79,* 9471-9477.
19. Mao, H., Cremer, P. S. & Manson, M. D. A sensitive, versatile microfluidic assay for bacterial chemotaxis. *Proc. Natl. Acad. Sci.* **2003**, *100,* 5449-5454.
20. Nam, S. W., Van Noort, D., Yang, Y. & Park, S. A biological sensor platform using a pneumatic-valve controlled microfluidic device containing *Tetrahymena pyriformis*. *Lab Chip* **2007**, *7,* 638-640.
21. Lanning, L. M., Ford, R. M. & Long, T. Bacterial chemotaxis transverse to axial flow in a microfluidic channel. *Biotechnol. Bioeng.* **2008**, *100,* 653-663.
22. Long, T. & Ford, R. M. Enhanced transverse migration of bacteria by chemotaxis in a porous T-sensor. *Environ. Sci. Technol.* **2009**, *43,* 1546-1552.
23. Seymour, J. R., Ahmed, T., Marcos & Stocker, R. A microfluidic chemotaxis assay to study microbial behavior in diffusing nutrient patches. *Limnol. Oceanogr.: Methods* **2008**, *6,* 477-488.
24. Ahmed, T. & Stocker, R. Experimental verification of the behavioral foundation of bacterial transport parameters using microfluidics. *Biophys. J.* **2008**, *95,* 4481-4493.
25. Diao, J., Young, L., Kim, S., Fogarty, E. A., Heilman, S. M., Zhou, P., Shuler, M. L., Wu, M. & DeLisa, M. P. A three-channel microfluidic device for generating static linear gradients and its application to the quantitative analysis of bacterial chemotaxis. *Lab Chip* **2006**, *6,* 381-388.
26. Cheng, S.-Y., Heilman, S., Wasserman, M., Archer, S., Shuler, M. L. & Wu, M. A hydrogel-based microfluidic device for the studies of directed cell migration. *Lab Chip* **2007**, *7,* 763-769.
27. Park, J., Bansal, T., Pinelis, M. & Maharbiz, M. M. A microsystem for sensing and patterning oxidative microgradients during cell culture. *Lab Chip* **2006**, *6,* 611-622.

28. Salman, H., Zilman, A., Loverdo, C., Jeffory, M. & Libchaber, A. Solitary modes of bacterial culture in a temperature gradient. *Phys. Rev. Lett.* **2006**, *97,* 118101.
29. Ely, B., Gerardot, C. J., Fleming, D. L., Gomes, S. L., Frederikse, P. & Shapiro, L. General nonchemotactic mutants of Caulobacter crescentus. *Genetics* **1986**, *114,* 717-730.
30. Kosar, T. F., Chen, C., Stucky, N. L. & Folch, A. Arrays of microfluidically-addressable nanoholes. *J. Biomed. Nanotech.* **2005**, *1,* 161-167.
31. Ismagilov, R. F., Ng, J. M. K., Kenis, P. J. A. & Whitesides, G. M. Microfluidic arrays of fluid-fluid diffusional contacts as detection elements and combinatorial tools. *Anal. Chem.* **2001**, *73,* 5207-5213.
32. Cannon, D. M. J., Kuo, T.-C., Bohn, P. W. & Sweedler, J. V. Nanocapillary array interconnects for gated analyte injections and electrophoretic separations in multilayer microfluidic architectures. *Anal. Chem.* **2003**, *75,* 2224-2230.
33. Nierman, W. C., Feldblyum, T. V., Laub, M. T., Paulsen, I. T., Nelson, K. E., Elsen, J., Heidelberg, J. F., Alley, M. R. K., Ohta, N., Maddock, J. R., Potocka, I., Nelson, W. C., Newton, A., Stephens, C., Phadke, N. D., Ely, B., DeBoy, R. T., Dodson, R. J., Durkin, A. S., Gwinn, M. L., Haft, D. H., Kolonay, J. F., Smit, J., Craven, M. B., Khouri, H., Shetty, J., Berry, K., Utterback, T., Tran, K., Wolf, A., Vamathevan, J., Ermolaeva, M., White, O., Salzberg, S. L., Venter, J. C., Shapiro, L. & Fraser, C. M. Complete genome sequence of *Caulobacter crescentus*. *Proc. Natl. Acad. Sci.* **2001**, *98,* 4136-4141.
34. Jones, S. E., Ferguson, N. L. & Alley, M. R. K. New members of the ctrA regulon: the major chemotaxis operon in *Caulobacter* is CtrA dependent. *Microbiol.* **2001**, *147,* 949-958.
35. Gonin, M., Quardokus, E. M., O'Donnol, D., Maddock, J. & Brun, Y. V. Regulation of stalk elongation by phosphate in *Caulobacter crescentus*. *J. Bacteriol.* **2000**, *182,* 337-347.
36. Koch, B., Jensen, L. E. & Nybroe, O. A panel of Tn7-based vectors for insertion of the gfp marker gene or for delivery of cloned DNA into gram-negative bacteria at a neutral chromosomal site. *J. Microbiol. Methods* **2001**, *45,* 187-195.
37. West, L., Yang, D. & Stephens, C. Use of the *Caulobacter crescentus* genome sequence to develop a method for systematic genetic mapping. *J. Bacteriol.* **2002**, *184,* 2155-2166.
38. Entcheva-Dimitrov, P. & Spormann, A. M. Dynamics and control of biofilms of the oligotrophic bacterium *Caulobacter crescentus*. *J. Bacteriol.* **2004**, *186,* 8254-8266.
39. Degnen, S. T. & Newton, A. Chromosome replication during development in *Caulobacter crescentus*. *J. Mol. Biol.* **1972**, *64,* 671-680.
40. Johnson, R. C. & Ely, B. Isolation of spontaneously derived mutants of Caulobacter crescentus. *Genetics* **1977**, *86,* 25-32.
41. Sbalzarini, I. F. & Koumoutsakos, P. Feature point tracking and trajectory analysis for video imaging in cell biology. *J. Struct. Biol.* **2005**, *151,* 182-195.
42. Frymier, P. D., Ford, R. M., Berg, H. C. & Cummings, P. T. Three-dimensional tracking of motile bacteria near a solid planar surface. *Proc. Natl. Acad. Sci.* **1995**, *92,* 6195-6199.

43. Lauga, E., DiLuzio, W. R., Whitesides, G. M. & Stone, H. A. Swimming in circles: Motion of bacteria near solid boundaries. *Biophys. J.* **2006**, *90*, 400-412.
44. Schmidt, J. M. Observations on the adsorption of Caulobacter bacteriophages containing ribonucleic acid. *J. Gen. Microbiol.* **1966**, *45*, 347-353.
45. Bodenmiller, D., Toh, E. & Brun, Y. V. Development of surface adhesion in *Caulobacter crescentus*. *J. Bacteriol.* **2004**, *186*, 1438-1447.
46. Xia, P., Bungay, P. M., Gibson, C. C., Kovbasnjuk, O. N. & Spring, K. R. Diffusion coefficients in the lateral intercellular spaces of Madin-Darby canine kidney cell epithelium determined with caged compounds. *Biophys. J.* **1998**, *74*, 3302-3312.
47. Ueadaira, H. & Uedaira, H. Diffusion coefficients of xylose and maltose in aqueous solutions. *Bull. Chem. Soc. Jpn.* **1969**, *42*, 2140-2142.
48. Sjöman, E., Mänttäri, M., Nyström, M., Koivikko, H. & Heikkilä, H. Separation of xylose from glucose by nanofiltration from concentrated monosaccharide solutions. *J. Mem. Sci.* **2007**, *292*, 106-115.
49. Deen, W. M. Hindered transport of large molecules in liquid-filled pores. *AIChE J.* **1987**, *33*, 1409-1425.
50. Giddings, J. C. *Unified separation science* (Wiley-Interscience, New York, 1991).
51. Liu, Z. & Papadopoulos, K. D. Unidirectional motion of *Escherichia coli* in restrictive capillaries. *Appl. Environ. Microbiol.* **1995**, *61*, 3567-3572.
52. Hill, J., Kalkanci, O., McMurry, J. L. & Koser, H. Hydrodynamic surface interactions enable *Escherichia coli* to seek efficient routes to swim upstream. *Phys. Rev. Lett.* **2007**, *98*, 068101.
53. Packer, H. L. & Armitage, J. P. The chemokinetic and chemotactic behavior of *Rhodobacter sphaeroides*: Two independent responses. *J. Bacteriol.* **1994**, *176*, 206-212.
54. Attmannspacher, U., Scharf, B. & Schmitt, R. Control of speed modulation (chemokinesis) in the unidirectional rotary motor of *Sinorhizobium meliloti*. *Mol. Microbiol.* **2005**, *56*, 708-718.
55. Meier, V. M., Muschler, P. & Scharf, B. E. Functional analysis of nine putative chemoreceptor proteins in *Sinorhizobium meliloti*. *J. Bacteriol.* **2007**, *189*, 1816-1826.
56. Hyakutake, A., Homma, M., Austin, M. J., Boin, M. A., Hase, C. C. & Kawagishi, I. Only one of the five CheY homologs in *Vibrio cholerae* directly switches flagellar rotation. *J. Bacteriol.* **2005**, *187*, 8403-8410.
57. McCarter, L. L. Polar flagellar motility of the Vibrionaceae. *Microbiol. Mol. Biol. Rev.* **2001**, *65*, 445-462.
58. Porter, S. L., Wadhamns, G. H. & Armitage, J. P. *Rhodobacter sphaeroides*: Complexity in chemotactic signaling. *Trends Microbiol.* **2008**, *16*, 251-260.
59. Schmitt, R. Sinorhizobial chemotaxis: a departure from the enterobacterial paradigm. *Microbiol.* **2002**, *148*, 627-631.
60. Bischoff, D. S. & Ordal, G. W. Sequence and characterization of *Bacillus subtilis* CheB, a homolog of *Escherichia coli* CheY, and its role in a different mechanism of chemotaxis. *J. Biol. Chem.* **1991**, *266*, 12301-12305.
61. Adler, J. Chemotaxis in bacteria. *Science* **1966**, *153*, 708-716.

62. Adler, J. A method for measuring chemotaxis and use of the method to determine optimum conditions for chemotaxis by *Escherichia coli*. *J. Gen. Microbiol.* **1973**, *74*, 77-91.

CHAPTER 6. Electrokinetic trapping on integrated microchannel - multiple nanopore devices.[1]

6.1. Introduction to relevant electrokinetic forces.

One approach to add new functionality to microfluidic devices is to construct multilayer systems,[2-4] and some of these devices have incorporated nanoscale elements.[5-7] Several examples of nanopore membranes integrated with microfluidic channels have been demonstrated,[8-11] as mentioned in Chapters 1 and 5. All of these devices made use of high pore density (~10^8 pores/cm^2) membranes. At lower pore densities, the nanopores can act as highly resistive elements because of their low cross-sectional areas. Thus, high electric field strengths can be generated with only modest potentials applied across short distances (i.e., the membrane thickness). Conically-shaped nanopores,[12,13] in particular, create high electric field strengths and gradients at their tips and have been used for electrophoretic capture of nanoscale particles[14] and particle characterization.[15]

The ability to generate and address strong, localized electric fields is of interest because the resulting electrophoretic and dielectrophoretic forces are useful in separating and characterizing nano- and microscale particles. Electrophoresis is well-characterized as a separation technique based on the ratio of the charge and hydrodynamic radius of the analyte. The electrophoretic force on a particle, f_{ep}, is linearly proportional to the applied electric field and is

$$f_{ep} = zFE \tag{6.1}$$

where z is the effective charge, F is Faraday's constant, and E is the electric field.[16] Dielectrophoresis (DEP), in contrast, refers to the effect of an electric field gradient on a polarizable particle. When a particle is more polarizable than the surrounding medium,

the particle experiences a dielectrophoretic force in the direction of increasing electric field gradient (positive DEP), and when a particle is less polarizable than the surrounding medium, the particle is repelled by regions of high field gradient (negative DEP). The dielectrophoretic force on a particle, f_{dep}, is

$$f_{dep} = 2\pi\varepsilon_m r^3 K \nabla E^2 \tag{6.2}$$

where ε_m is the permittivity of the suspending medium, r is the particle radius, E is the electric field strength, and K is the Clausius-Mosotti factor, which depends on the conductivities and permittivities of the medium and the particle and on the frequency of the applied field.[17] As seen in Equation 6.2, the dielectrophoretic force depends on the gradient of the square of the electric field. Because the force is proportional the field gradient rather than the field strength, the dielectrophoretic force is independent of the direction of the applied field. Frequency dependence arises in the Clausius-Mosotti term because the polarizability of lossy dielectric particles depends on the frequency of the applied field.[17] This frequency dependence allows particles to be either trapped or repelled by regions of high field gradient simply by adjusting the frequency of the trapping waveform.

Dielectrophoresis is an effective means to trap, sort, and preconcentrate particles of interest.[18] Traditionally, the high field gradients required for DEP are generated at patterned metal electrodes.[19] However, more recent work has been in electrodeless DEP, in which high electric field gradients are generated by micrometer-scale constrictions between insulating surfaces[20-22] or at the tip of a nanopipette.[23,24] Electrodeless DEP has a major advantage in that the trapping region is separated from the electrode surface, eliminating the problem of electrochemical gas evolution at the trapping location.

Here, we take advantage of the high electric fields that can be generated at the tips of conical nanopores by integrating membranes containing these pores at low pore densities between two microchannels. By coupling AC and DC electric fields to these integrated nanopore/microfluidic devices, we demonstrated for the first time electrophoretic and dielectrophoretic capture and concentration of microscale particles at the nanopore tips. While dielectrophoretic trapping has been demonstrated with nanopipettes,[23,24] to date, only micrometer-scale trapping elements have been integrated with microfluidic architectures. The microchannels allowed easy coupling of the electrical potentials to the nanoporous membrane and efficient particle delivery to the high electric field region at the membrane. Figure 6-1 shows a schematic of the device with the microchannels positioned orthogonal to each other and the nanoporous membrane between them. Polystyrene microspheres, 200 nm and 1 μm in diameter, and bacterial cells were trapped, concentrated, and released with this nanopore device. To determine the electrophoretic and dielectrophoretic contributions to trapping, we evaluated symmetric and asymmetric waveforms with applied potentials ranging from ±10 to ±100 V and frequencies from DC to 100 kHz.

6.2. Methods.

Nanopore device fabrication. Tracked poly(ethylene terephthalate) (PET) membranes (GSI, Darmstadt DE) with a track density of 10^6 tracks/cm^2 were etched and characterized by scanning electron microscopy as described in Section A4. Two membranes were used in these experiments, and the pore sizes were 130 ± 50 nm in diameter at the tip and 0.94 ± 0.11 μm in diameter at the base for the first membrane and

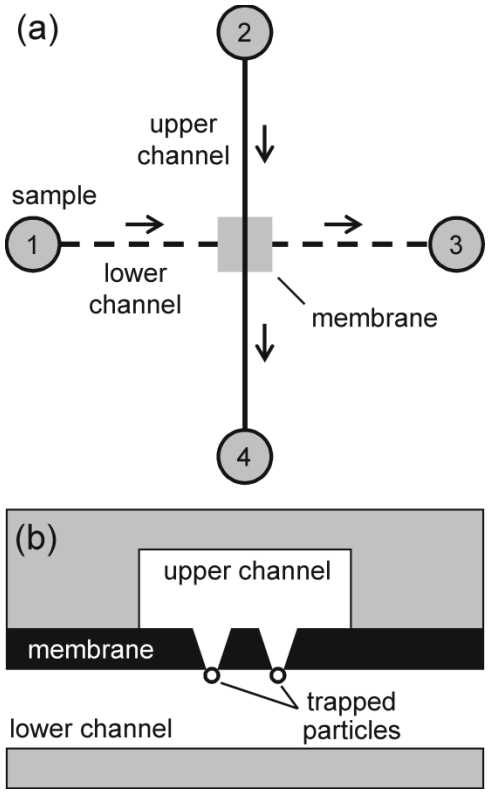

Figure 6-1. (a) Schematic of the conical nanopore device for AC electrokinetic trapping. The two microchannels were positioned orthogonally with the nanopore membrane sandwiched between them. The upper (solid) channel contained buffer, and the lower (dashed) channel contained the particle sample. Arrows depict direction of hydrostatic flow. (b) Cross section of the device at the microchannel intersection. Particles were trapped at the tips of the nanopores in the membrane separating the two channels.

140 ± 20 nm in diameter at the tip and 1.04 ± 0.04 μm in diameter at the base for the second membrane (n = 20 measurements for each side of each membrane).

We fabricated and characterized poly(dimethylsiloxane) (PDMS) microchannels from SU-8 masters as described in Sections A1 and A2. The channel masters were 33.2 ± 0.4 μm high and 75.3 ± 1.9 μm wide for 10 measurements made along the length of the master. The device was assembled by sandwiching an etched nanopore membrane between two orthogonal PDMS channels, as seen in Figure 6-1a. The assembled chip was then placed between an aluminum plate and a Plexiglas plate, which were held together by four screws. The screws were set finger-tight to seal the gap between the PDMS slabs around the edge of the membrane. The bottom aluminum plate had a 9.5 mm diameter hole machined in the center for optical access to the trapping region formed at the intersection of the two PDMS channels. After assembly the device was filled with buffer using a subambient pressure from a vacuum pump. A picoammeter/voltage source (6487, Keithley Instruments, Inc.) was used to perform current measurements of an assembled device. The current was measured between each pair of fluid reservoirs, and resistance of the membrane calculated.

Nanopore device operation. Hydrostatic flow was created in the channels by adjusting the fluid levels in 25 mm tall, 4 mm i.d. glass reservoirs epoxied to the top Plexiglas plate. Samples consisted of either 1 μm or 200 nm fluorescent microspheres (Invitrogen Corp.) or *Caulobacter crescentus* (courtesy of Prof. Yves V. Brun, Indiana University). The actual diameters of the microspheres were 1.100 ± 0.035 μm and 210 ± 10 nm; however, they are referred to by their nominal diameters of 1 μm and 200 nm, respectively. For the microsphere studies, 10 mM phosphate (J.T. Baker, Inc.) with 0.1%

Triton X-100 (Promega Corp.) (pH 6.8, σ = 1.6 mS/cm) was used as the buffer. Buffer conductivities were measured using a digital conductivity meter (1056, VWR International, LLC) equipped with a gold-plated dip conductivity cell. The Triton X-100 surfactant minimized the adsorption of the microspheres to the membrane surface. All microspheres were obtained as 2% solid solutions in 2 mM azide. The microspheres were then diluted to a concentration of 5400 or 10,800 microspheres/mL for the 1 μm microspheres or 9750 microspheres/mL for the 200 nm microspheres, using the 10 mM phosphate and 0.1% Triton X-100 buffer. For the bacteria trapping, M2G, a typical growth medium for *C. crescentus*, was used as the buffer. M2G consists of 12.3 mM Na_2HPO_4, 7.8 mM KH_2PO_4, 9.3 mM NH_4Cl, 0.5 mM $MgSO_4$, 0.5 mM $CaCl_2$, 8 μM EDTA, 10 μM $FeSO_4 \cdot 7H_2O$, and 0.2% dextrose (σ = 4.3 mS/cm).[25] *C. crescentus* strain CB15Δ*hfs*DABdsred was used. This strain had the advantages of lacking a holdfast on the stalk cells, which minimized adhesion to the channel walls and membrane, and of being fluorescent, which made detection and quantification of the trapped bacteria easier. The bacteria were cultured in M2G media with 5 μg/mL kanamycin. A Zetasizer Nano-ZS (Malvern Instruments, Ltd.) was used to determine the zeta potentials of the microspheres and *C. crescentus* cells.

Platinum wires were placed in reservoirs 1 and 2 to apply the appropriate waveforms to the device. To minimize the electric field dropped across the channel and the resulting electroosmotic flow, jumpers were connected between reservoirs 1 and 3 and between reservoirs 2 and 4. An analog output board (PCI-6713, National Instruments Corp.) and LabView program were used to control the waveforms applied to the device. The trapping waveforms were asymmetric (unipolar) and symmetric (about zero) square

waves with a 50% duty cycle and ranged from -100 V to 100 V. The waveform frequencies were incremented in decades from DC to 100 kHz. For initial experiments, ±10 V from the analog output boards was used directly, and for subsequent experiments requiring potentials up to ±100 V, an amplifier built in-house was used with a pair of DC power supplies (E3612A, Agilent Technologies, Inc.). After trapping proceeded for a predetermined accumulation time, the trapped microspheres were released either by applying -10 V or -100 V to repel the particles from the membrane. To release trapped bacteria, the potential was simply removed.

Trapping was monitored using a CCD camera (Cascade 512B, Photometrics) attached to an inverted microscope (TE-2000U, Nikon, Inc.) equipped for epifluorescence detection with a 60x extra-long working distance objective. Illumination was provided by a metal halide lamp (X-Cite 120, EXFO Life Sciences) and was filtered using a TRITC filter cube (96321M, Nikon, Inc.). Stacks of images were acquired while the trapping field was applied, and trapping was quantified either by counting the number of individual particles trapped during a fixed period of time or by determining the change in counts between an image of the trapped fluorescent particles and a background image acquired after the particles were released. Image acquisition and data analysis were performed using IPLab software (BD Biosciences Bioimaging). All trapping data were then normalized to the value obtained for trapping at 0 Hz.

Confocal fluorescence images of the microspheres trapped at the nanopores were obtained using a Nikon Swept Field Confocal system on an inverted microscope (TE-2000E) and NIS-Elements AR imaging software (v. 2.30). For the confocal images, the buffer in the top channel was doped with 10 μM disodium fluorescein (Sigma-Aldrich,

Inc.) in order to visualize the channel. Two-color fluorescence images of the fluorescein-filled channel and the red fluorescent microspheres were obtained by alternating illumination between the 488 nm and 561 nm laser lines on the confocal system. Confocal fluorescence images were obtained using a step size of 0.6 μm and were detected using a CCD camera (QuantEM 512SC, Photometrics).

Electric field simulations. We used COMSOL Multiphysics software (v. 3.3, COMSOL, Inc.) to perform finite element analysis of the electric field strength and gradient in the vicinity of the nanopores. In the simulated geometry, the nanopore was 130 nm at the tip, 1 μm at the base, and 10 μm long. A 20 μm thick layer of electrolyte was assumed on both sides of the membrane, and an applied potential of 4 V was modeled by setting the potential of the upper surface of the electrolyte layer equal to 0 V and the potential of the lower surface to 4 V. The membrane and channel walls were modeled as electrical insulators. The mesh was generated automatically by the software, and analysis was performed using COMSOL Multiphysics Conductive Media DC to solve for the electric field distribution.

6.3. Results and discussion.

The assembled device shown schematically in Figure 6-1 had PDMS channels that were 33 μm deep, 75 μm wide, and 13 mm long. Two hours of etching produced nanopores that were nominally 130 nm in diameter at the tip, 1 μm in diameter at the base, and 10 μm long. Exact nanopore dimensions are given in the figure captions for each data set. Based on the area of the microchannel intersection and pore density ($10^6/cm^2$), an average of 60 pores was expected in the intersection. This meant that the

nanopores accounted for approximately 40% of the resistance of the device. For example, an integrated membrane with pores 130 ± 50 nm at the tip and 940 ± 110 nm at the base contributed 39.6% of the total resistance of the device. Thus, when 10 V were applied to the device, an average field strength of 4000 V/cm (4 V across a 10 μm thick membrane) was produced across the nanopore membrane. Because of the conical geometry of the nanopores, the potential drop occurred disproportionately along the length of the pore, with the highest field strengths achieved at the tip of the pore.

The expected electric field distribution was modeled using the AC/DC module in COMSOL Multiphysics. Figure 6-2 shows the electric field distribution for 4 V dropped across a single conical nanopore with a 130 nm diameter tip and a 1 μm diameter base, which corresponded to 10 V applied at the reservoirs of the device. A maximum field strength of 1.3×10^4 V/cm and a maximum gradient of the field squared of 4.2×10^{13} V^2/cm^3 were produced at the pore wall near the tip. These values were well within the range typically used for dielectrophoretic trapping. Sub-micrometer particles and biopolymers, such as DNA and proteins, have been trapped using electric field strengths of 10^3-10^4 V/cm in the vicinity of micro- and nanoscale structures.[20,21,23,24,26,27] Additionally, these electric fields were calculated for a modest applied voltage of 10 V across the entire device, so electric field strengths up to 1.3×10^5 V/cm were estimated when 100 V were applied to the device.

As evident from the discussion above, the pore density played an important role in determining the effectiveness of trapping. The optimum pore density had to be high enough that the pores were distributed across the intersection and covered most of the intersection area so that particles at all lateral positions in the flow stream had a chance to

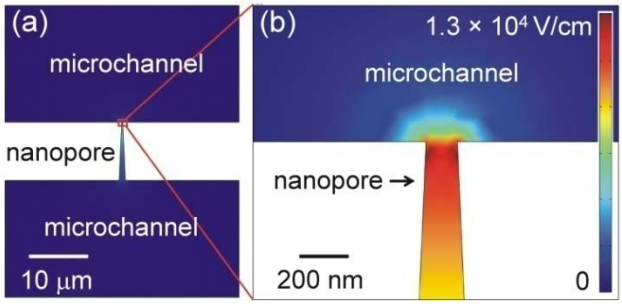

Figure 6-2. (a) COMSOL simulation of the electric field distribution at a nanopore. The nanopore was 130 nm in diameter at the tip, 1 μm in diameter at the base, and 10 μm long. A 20 μm thick layer of buffer was modeled on both sides of the pore, and the applied potential was 4 V. (b) Enlarged view of the small opening of the pore where the electric field strength and the gradient of the field squared have their maximum values of 1.3×10^4 V/cm and 4.2×10^{13} V^2/cm^3, respectively. The results of this simulation were similar to those shown in previous work.[14]

be trapped. However, the optimum pore density also needed to be low enough that the pores made up a significant percentage of the total device resistance. This was required to generate a sufficiently high electric field at the pore openings. A higher pore density, e.g., 10^8 pores/cm^2, would have resulted in 6000 pores in the intersection, but the average field strength along each pore would be just 66 V/cm. At the other extreme, a pore density of 1.7×10^4 pores/cm^2 would have yielded on average one pore in the intersection. This would produce an extremely high average field strength across the pore of 9750 V/cm, but would decrease the area of the membrane which could be used for trapping. We found an intermediate pore density of 10^6 pores/cm^2 to be a reasonable compromise between these two criteria, resulting in approximately 60 pores in the intersection with an average electric field strength of 4000 V/cm across each pore.

We investigated both asymmetric and symmetric electric fields for trapping negatively-charged, carboxylate-modified microspheres. For the asymmetric fields, the microspheres were trapped when a positive potential was applied to the opposite side of the membrane. Figure 6-3 shows a bright-field image of the nanopores (dark spots) in the intersection and fluorescence images of 1-μm microspheres trapped at the nanopores by a 10 V, 100 kHz asymmetric square wave and subsequently released by applying -10 V DC. A small number of microspheres remained adsorbed to the membrane surface after release; however, application of -100 V DC was effective at repelling the remaining microspheres from the membrane surface (data not shown). Figure 6-4 shows a confocal image of the 200 nm microspheres trapped at the pores. In Figure 6-4 the microspheres appear to be trapped just above the pore openings. Although the highest electric field strength was found just inside the pore opening (Figure 6-2), the 200 nm microspheres

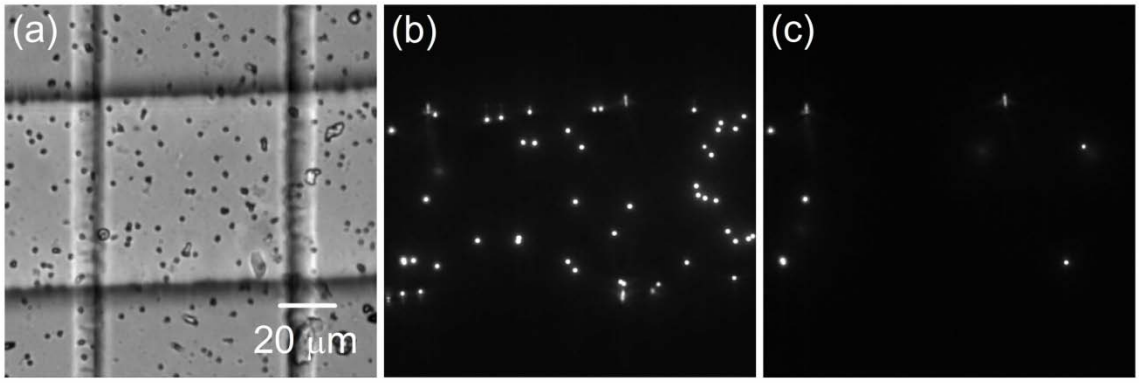

Figure 6-3. (a) Bright-field image of the intersection of two microfluidic channels separated by a nanopore membrane. The dark spots in the image were the nanopores. The horizontal channel was on the bottom of the device and contained the sample solution. Fluorescence images of 1 μm microspheres, which had been trapped at the intersection of the device by applying a 10 V, 100 kHz asymmetric square wave, (b) immediately following their release by reversing the applied potential, and (c) after the released microspheres were swept away by hydrostatic flow. The nanopores were 140 ± 20 nm in diameter at the tip and 1040 ± 40 nm in diameter at the base.

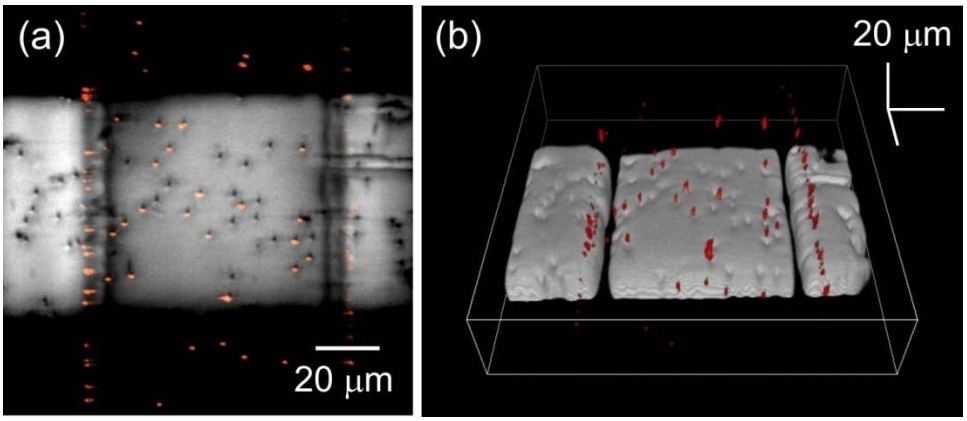

Figure 6-4. (a) Two-color confocal image of 200 nm microspheres (red) trapped at the membrane. To better visualize trapping at the nanopores, the horizontal channel was filled with 10 μM disodium fluorescein, and the resulting green fluorescence signal is shown in gray. The dark lines in the fluorescein-containing channel were due to the scattering of the fluorescence signal by the walls of the vertical channel. (b) A three-dimensional rendering of the 200 nm microspheres trapped at the nanopores. A stack of confocal images, which contained the image shown in (a), was used to reconstruct the three-dimensional image. The pores used for this experiment were 130 ± 50 nm in diameter at the tip and 940 ± 110 nm in diameter at the base.

were larger than the pore opening at the tip and, therefore, were trapped at the membrane surface.

Figure 6-5a shows the frequency dependence for trapping of 200 nm and 1-μm microspheres using an asymmetric 10 V square wave as the trapping waveform. Trapping efficiency was determined by counting the individual number of microspheres trapped during a 3-min interval, and the data were normalized to the trapping produced by the DC field. For polystyrene microspheres in aqueous media, the dielectrophoretic force is expected to be positive at low frequencies and negative at high frequencies;[28] however, when 10 V asymmetric waves were applied, trapping tended to increase with the frequency of the applied field. For the 1 μm microspheres, trapping dropped off for the 1 Hz waveform, but frequencies from 10 Hz – 100 kHz were as or more effective than a DC field. For the 200 nm microspheres, a similar trend was observed, in which trapping was less effective for low frequency waveforms than for DC. However, for frequencies of 1 kHz or greater, 200 nm microspheres were trapped equally well or better than for DC.

Figure 6-5b shows the increase in fluorescence signal with time as 1 μm microspheres accumulated at the membrane. As in Figure 6-5a, a noticeable difference in trapping behavior of the 1 μm microspheres was noted for the 1 Hz waveform. Trapping frequencies of 0, 10, and 1000 Hz resulted in steady increases in fluorescence intensity as microspheres were trapped at the membrane. In contrast, the data for the 1 Hz waveform showed an initial drop, due to photobleaching of the poly(ethylene terephthalate) membrane, followed by fluctuations in signal as microspheres flowed through the intersection without being trapped.

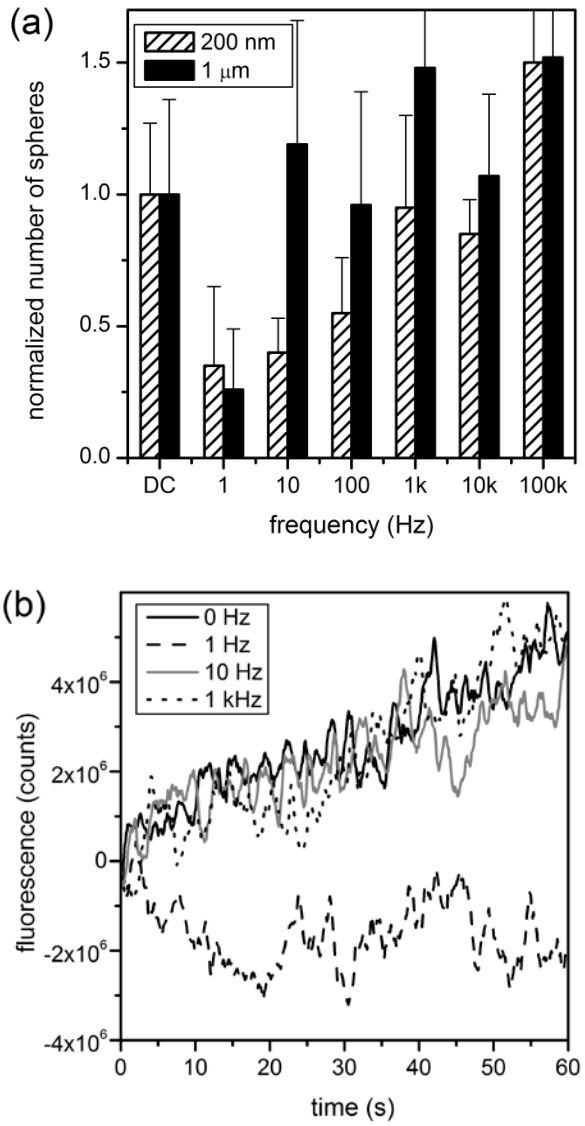

Figure 6-5. (a) Variation in the number of trapped 200 nm and 1 μm microspheres with frequency for a 10 V asymmetric square wave. Trapping was evaluated by counting the number of particles trapped in a 3-min interval and normalized to the number of particles trapped by the DC field. For the 1 μm microspheres, the error bars are ±σ for n = 6 for the DC measurements and n = 4 for the AC measurements, and for the 200 nm microspheres, the error bars are ±σ for n = 3 for both the DC and AC measurements. (b) Variation in fluorescence signal with time as 1 μm microspheres were trapped at the nanopores. Data for trapping frequencies of 0, 1, 10, and 1000 Hz are shown. Each trace was an average of at least 4 runs, and all runs were normalized to a starting signal of zero counts. Pore dimensions were the same as in Figure 6-3.

The trapping shown in Figures 6-3 and 6-4 and characterized in Figure 6-5 was primarily the result of the electrophoretic force on the particles. The frequency dependence of the trapping can be understood by considering the approximate timescale required for a trapped microsphere to escape from the vicinity of a pore. We estimated the time required for a microsphere to escape trapping by calculating the time required for a particle with a given diameter to travel one particle radius away from the membrane surface. For these calculations, we considered the influence of diffusion and hydrostatic flow to transport the particle from the membrane surface. The average particle velocity in the pressure-driven flow was 68.8 ± 20.9 μm/s, with a high standard deviation due to the parabolic flow profile. At 500 and 100 nm from the membrane surface, the linear velocities were estimated to be 1.2 and 0.24 μm/s, respectively. For a 1 μm microsphere, approximately 0.13 s would be required for the microsphere to travel 0.5 μm. This corresponded to a critical electrophoretic trapping frequency of 8 Hz, which agreed with the improved trapping for waveforms with frequencies of 10 Hz or greater. For a 200 nm microsphere, the critical frequency was expected to be 440 Hz, which also agreed well with the observed trapping behavior.

Because the error bars for both the 200 nm and 1 μm microsphere data in Figure 6-5a were large, we applied a two-tailed, unpaired t-test to determine whether the trapping behavior at each frequency was statistically different from trapping with the DC field. For the 1 μm microspheres, the 1 Hz data were statistically significant from the DC data for $\alpha = 0.005$, and for the 200 nm microspheres, the 1 and 10 Hz data were significant for $\alpha = 0.05$, and the 100 Hz data for $\alpha = 0.1$, also confirming statistical differences in the data sets. We attributed the variation in the data to several factors, including the random

distribution of pores across the membrane surface, the stochastic arrival of the microspheres in time, variation in the microsphere diameters, and the spatial distribution of the microspheres both laterally and in the z-direction.

Square waves which were symmetric about zero were also evaluated as trapping waveforms. These studies helped to elucidate the relative contributions of the electrophoretic and dielectrophoretic forces on trapping in the device. Because the dielectrophoretic force is proportional to the gradient of the square of the field,[17] the force is independent of the direction (or sign) of the field. This is in contrast to the electrophoretic force which depends on the sign of the electric field. Consequently, trapping waveforms which contain both the positive and the negative half-waves can help to distinguish the effects of the two forces.

For lower applied potentials, e.g., amplitude of 10 V, no trapping was observed for symmetric square waves of any frequency. We attributed this result to the dominance of the electrophoretic force for lower electric field strengths. During the negative half-cycle of the trapping waveform, the electrophoretic force repelled the negatively-charged microspheres from the pores, preventing long-term ($> \tau$ s) trapping of the particles. At higher applied voltages, e.g., amplitude of 100 V, trapping was observed for low frequency waveforms. Figure 6-6 shows the frequency dependence of 1 μm microspheres for a symmetric 100 V trapping waveform. Trapping was quantified as the sum of the fluorescence signal in the field of view after 2 min of trapping. Each image was background-subtracted using a fluorescence image taken after the trapped microspheres were released, and the data were normalized to the trapping for the DC field. The results were consistent with dominance of the dielectrophoretic force, which should be positive

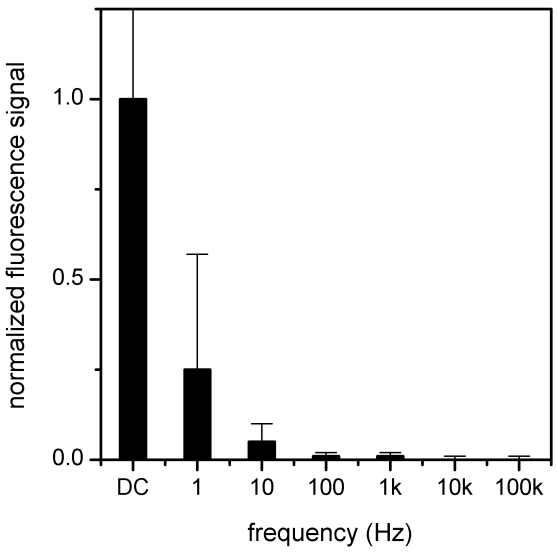

Figure 6-6. Variation of trapping behavior of 1 μm microspheres with frequency for a 100 V symmetric square wave. Trapping was evaluated from the fluorescence signal for the field of view after 2 min of accumulation time. A background signal which consisted of an image taken after the trapped microspheres were released was subtracted from each data point. All data were normalized to the trapping for the DC field. The errors bars are $\pm\sigma$ for n = 3 for each frequency. Pore dimensions were the same as for Figure 6-4.

(attractive) for the polystyrene microspheres at low frequencies and negative (repulsive) at high frequencies. The transition between electrophoretically-dominated behavior and dielectrophoretically-dominated behavior was expected to occur as the applied voltage increased since the electrophoretic force increases linearly with the electric field (Equation 6.1) while the dielectrophoretic force increases with the gradient of the square of the field strength (Equation 6.2). For intermediate voltages, when neither force was dominant, the trapping behavior should reflect contributions from both electrophoresis and dielectrophoresis.

To demonstrate an application of this trapping technique, the nanopore device was used to trap and accumulate live *C. crescentus* bacterial cells. Figure 6-7a shows a bright-field image of the nanopore membrane in the microchannel intersection, and Figure 6-7b-d shows fluorescence images of cells which have been trapped at the nanopore membrane using a 100 kHz asymmetric square wave with an amplitude of -25 V. The images were taken 3, 9, and 30 s after the trapping field was applied and show a steady accumulation of bacteria in the trapping region. After accumulating the bacteria at the nanopores for 45 s, the cells were released by removing the trapping voltage. At any given time, a fraction of the *C. crescentus* cells were in their motile, flagellated swarmer stage and were therefore able to swim.[25] Observation of motile swarmer cells among the released bacteria confirmed that at least some of the trapped cells remained viable after being released.

Bacteria were successfully trapped at the nanopores using both symmetric and asymmetric square waves, although trapping was slightly more effective for asymmetric waveforms. Unlike the microspheres, the bacteria were trapped using symmetric

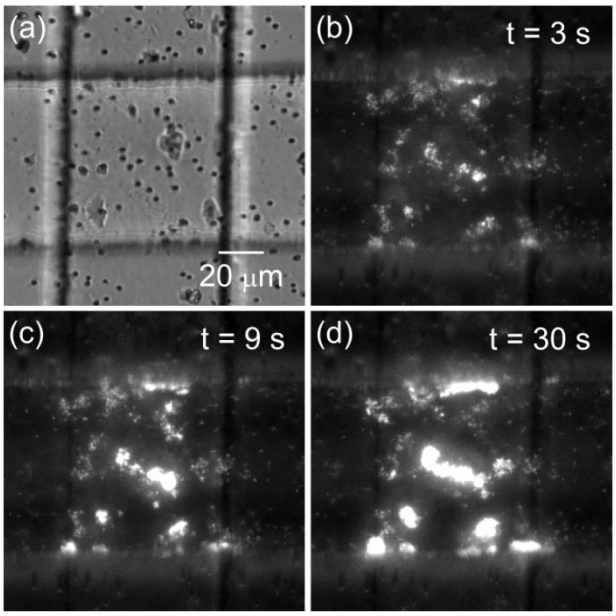

Figure 6-7. (a) Bright-field image of the nanopore membrane in the microchannel intersection and (b)-(d) fluorescence images of *C. crescentus* cells trapped at the nanopore membrane by a -25 V, 100 kHz asymmetric square wave taken (b) 3, (c) 9, and (d) 30 s after the trapping field was applied. Pore dimensions were the same as for Figure 6-4.

waveforms with lower applied potentials (25 V) and higher frequencies (up to 100 kHz). We attributed the improved trapping for symmetric waveforms to a higher dielectrophoretic force on the bacteria compared to the microspheres. The difference in the strength of the dielectrophoretic force was due to the difference in composition and, therefore, polarizability of the bacterial cells compared to the polystyrene microspheres. In addition, the bacteria were trapped most effectively using negative, asymmetric trapping waveforms, suggesting that the bacteria were trapped under electrokinetic conditions, i.e., electroosmotic and electrophoretic transport. The bacteria migrated in the cathodic direction in the PDMS microchannels, and the zeta potentials of the bacteria were -13.7 ± 2.1 mV (n = 3) and -12.6 ± 0.5 mV (n = 3) in M2G buffer and water, respectively. For comparison, 1 μm microspheres migrated in the anodic direction in the PDMS microchannels, and the zeta potential was -34.8 ± 4.5 mV (n = 3) in the 10 mM phosphate, 0.1% Triton X-100 buffer.

We also observed the bacteria samples routinely trapped at the intersection of the two channels (see Figure 6-7b-d), whereas microspheres also trapped in the membrane regions to either side of the intersection (see Figure 6-3b). The trapping outside the intersection occurred due to imperfect sealing of the PDMS substrate to the membrane, although any leakage was minimal such that fluorescent analytes (e.g., microspheres, bacteria, and disodium fluorescein) were never observed between the layers. A method for hydrophobic modification of the membrane which eliminates this effect is discussed in Chapter 7. The absence of bacterial trapping outside the intersection was likely due to the different relative and absolute magnitudes of the electrophoretic and dielectrophoretic forces on the cells compared to the microspheres.

6.4. Conclusions and future directions.

We have demonstrated successful trapping of both biological (bacterial cells) and non-biological (polystyrene microspheres) samples using an integrated nanopore/microchannel device. The high field strengths and gradients generated in the vicinity of the nanopore structures gave rise to both electrophoretic and dielectrophoretic effects. By adjusting the amplitude and frequency of the trapping waveform, the direction and relative magnitude of these two forces can be controlled. This trapping scheme relied on a combination of electrophoresis and dielectrophoresis and could potentially fractionate or concentrate particles based on size, charge, and polarizability. The possibility of capturing particles based on their dielectric properties makes this method complementary to alternative microfluidic particle traps, such as re-circulating flows, which trap based on a balance of pressure-driven and electrophoretic motion.[29] Additionally, the speed with which the trapping waveform can be varied suggests the possibility of on-the-fly tunable filtering.

Track-etch pores such as those used here can be fabricated with diameters down to 10 nm,[30] so stronger field gradients sufficient for trapping smaller analytes, perhaps single biomolecules, should be achievable. These pores are also well-established as resistive pulse sensors,[31] which means that future devices could use the nanopores as both trapping and sensing elements. Preliminary work in this direction is presented in Chapter 7. Because the nanopores were already integrated with microfluidic structures in the work presented here, additional processing or analysis steps could be incorporated into the microchannels upstream or downstream from the trapping/sensing region.

6.5. References.

1. This chapter reproduced in part with permission from Kovarik, M. L. and Jacobson, S. C. Integrated nanopore/microchannel devices for ac electrokinetic trapping of particles. *Anal. Chem.* **2008**, *80*, 657-664. Copyright 2008 American Chemical Society.
2. Unger, M. A., Chou, H. P., Thorsen, T., Scherer, A. & Quake, S. R. Monolithic microfabricated valves and pumps by multilayer soft lithography. *Science* **2000**, *288*, 113-116.
3. Anderson, J. R., Chiu, D. T., Jackman, R. J., Cherniavskaya, O., McDonald, J. C., Wu, H. K., Whitesides, S. H. & Whitesides, G. M. Fabrication of topologically complex three-dimensional microfluidic systems in PDMS by rapid prototyping. *Anal. Chem.* **2000**, *72*, 3158-3164.
4. Grover, W. H., Skelley, A. M., Liu, C. N., Lagally, E. T. & Mathies, R. A. Monolithic membrane valves and diaphragm pumps for practical large-scale integration into glass microfluidic devices. *Sensor Actuat B-Chem* **2003**, *89*, 315-323.
5. Kuo, T.-C., Cannon, D. M. J., Chen, Y., Tulock, J. J., Shannon, M. A., Sweedler, J. V. & Bohn, P. W. Gateable nanofluidic interconnects for multilayered microfluidic separation systems. *Anal. Chem.* **2003**, *75*, 1861-1867.
6. Wang, Y.-C., Stevens, A. L. & Han, J. Million-fold preconcentration of proteins and peptides by nanofluidic filter. *Anal. Chem.* **2005**, *77*, 4293-4299.
7. Kovarik, M. L. & Jacobson, S. C. Attoliter-scale dispensing in nanofluidic channels. *Anal. Chem.* **2007**, *79*, 1655-1660.
8. Ismagilov, R. F., Ng, J. M. K., Kenis, P. J. A. & Whitesides, G. M. Microfluidic arrays of fluid-fluid diffusional contacts as detection elements and combinatorial tools. *Anal. Chem.* **2001**, *73*, 5207-5213.
9. Cannon, D. M. J., Kuo, T.-C., Bohn, P. W. & Sweedler, J. V. Nanocapillary array interconnects for gated analyte injections and electrophoretic separations in multilayer microfluidic architectures. *Anal. Chem.* **2003**, *75*, 2224-2230.
10. de Jong, J., Lammertink, R. G. H. & Wessling, M. Membranes and microfluidics: a review. *Lab Chip* **2006**, *6*, 1125-1139.
11. Long, Z., Liu, D., Ye, N., Qin, J. & Lin, B. Integration of nanoporous membranes for sample filtration/preconcentration in microchip electrophoresis. *Electrophoresis* **2006**, *27*, 4927-4934.
12. Apel, P. Y., Korchev, Y. E., Ziwy, Z., Spohr, R. & Yoshida, M. Diode-like single-ion track membrane prepared by electro-stopping. *Nucl. Instrum. Methods Phys. Rev. Sect. B* **2001**, *184*, 337-346.
13. Li, N. C., Yu, S. F., Harrell, C. C. & Martin, C. R. Conical nanopore membranes. Preparation and transport properties. *Anal. Chem.* **2004**, *76*, 2025-2030.
14. Lee, S., Zhang, Y., White, H. S., Harrell, C. C. & Martin, C. R. Electrophoretic capture and detection of nanoparticles at the opening of a membrane pore using scanning electrochemical microscopy. *Anal. Chem.* **2004**, *76*, 6108-6115.
15. White, R. J. & White, H. S. Influence of electrophoresis waveforms in determining stochastic nanoparticle capture rates and detection sensitivity. *Anal. Chem.* **2007**, *79*, 6334-6340.

16. Giddings, J. C. *Unified separation science* (Wiley-Interscience, New York, 1991).
17. Jones, T. B. *Electromechanics of particles* (Cambridge University Press, Cambridge, 1995).
18. Hughes, M. P. Strategies for dielectrophoretic separation in laboratory-on-a-chip systems. *Electrophoresis* **2002**, *23*, 2569-2582.
19. Ramos, A., Morgan, H., Green, N. G. & Castellanos, A. AC electrokinetics: a review of forces in microelectrode structures. *J. Phys. D: Appl. Phys.* **1998**, *31*, 2338-2353.
20. Chou, C.-F., Tegenfeldt, J. O., Bakajin, O., Chan, S. S., Cox, E. C., Darnton, N., Duke, T. & Austin, R. H. Electrodeless dielectrophoresis of single- and double-stranded DNA. *Biophys. J.* **2002**, *83*, 2170-2179.
21. Cummings, E. B. & Singh, A. K. Dielectrophoresis in microchips containing arrays of insulating posts: theoretical and experimental results. *Anal. Chem.* **2003**, *75*, 4724-4731.
22. Pysher, M. D. & Hayes, M. A. Electrophoretic and dielectrophoretic field gradient technique for separating bioparticles. *Anal. Chem.* **2007**, *79*, 4552-4557.
23. Ying, L., White, S. S., Bruckbauer, A., Meadows, L., Korchev, Y. E. & David, K. Frequency and voltage dependence of the dielectrophoretic trapping of short lengths of DNA and dCTP in a nanopipette. *Biophys. J.* **2004**, *86*, 1018-1027.
24. Clarke, R. W., Piper, J. D., Ying, L. & Klenerman, D. Surface conductivity of biological macromolecules measured by nanopipette dielectrophoresis. *Phys. Rev. Lett.* **2007**, *98*, 198102.
25. Johnson, R. C. & Ely, B. Isolation of spontaneously derived mutants of Caulobacter crescentus. *Genetics* **1977**, *86*, 25-32.
26. Washizu, M., Suzuki, S., Kurosawa, O., Nishizaka, T. & Shinohara, T. Molecular dielectrophoreis of biopolymers. *IEEE Trans. Ind. Appl.* **1994**, *30*, 835-843.
27. Hölzel, R., Calander, N., Chiragwandi, Z., Willander, M. & Bier, F. F. Trapping single molecules by dielectrophoresis. *Phys. Rev. Lett.* **2005**, *95*, 128102.
28. Ermolina, I. & Morgan, H. The electrokinetic properties of latex particles: comparison of electrophoresis and dielectrophoresis. *J. Colloid Interf. Sci.* **2005**, *285*, 419-428.
29. Lettieri, G.-L., Dodge, A., Boer, G., de Rooij, N. F. & Verpoorte, E. A novel microfluidic concept for bioanalysis using freely moving beads trapped in recirculating flows. *Lab Chip* **2003**, *3*, 34-39.
30. Fischer, B. E. & Spohr, R. Production and use of nuclear tracks: imprinting structure on solids. *Rev. Mod. Phys.* **1983**, *55*, 907-948.
31. Baker, L. A., Choi, Y. & Martin, C. R. Nanopore membranes for biomaterials synthesis, biosensing and bioseparations. *Curr. Nanosci.* **2006**, *2*, 243-255.

CHAPTER 7. Electrokinetic trapping and resistive pulse sensing on integrated microchannel - single nanopore devices.

7.1. Introduction to resistive pulse sensing.

The logical limit of miniaturization for chemical analysis devices is at the level of a single ion or molecule. Single molecule detection is rapidly being developed for use in drug screening and in basic research on reaction intermediates and other low abundance species which go undetected by ensemble average measurements.[1,2] Studies of supramolecular assembly, in particular, will benefit from single-particle resolution because discrete assembly steps may be observed. Several detection methods have been developed to resolve single molecule events, including single-molecule fluorescence, force measurements, and resistive pulse sensing.[3] Of these, the resistive pulse method has the advantages of being relatively simple and readily miniaturizable for incorporation into micro- and nanofluidic systems. Additionally, detection does not require tagging of analyte molecules, yields nanometer resolution, and provides information based on analyte size, concentration, chemistry, and charge.[4,5]

Resistive pulse sensing detects analytes by measuring the change in current which occurs when an analyte particle enters an aperture between two conducting solutions.[5] When particle size is comparable to the aperture diameter, the presence of a particle in the aperture will produce a measurable change in the resistance by displacing a volume of conducting electrolyte solution equal to the particle volume. The change in resistance results in a current pulse during particle transit as shown in Figure 7-1. For micrometer-scale particles and apertures, the magnitude of the current pulse is directly proportional to the particle size,[3] but at the nanoscale, the signal can be more complex. In low ionic

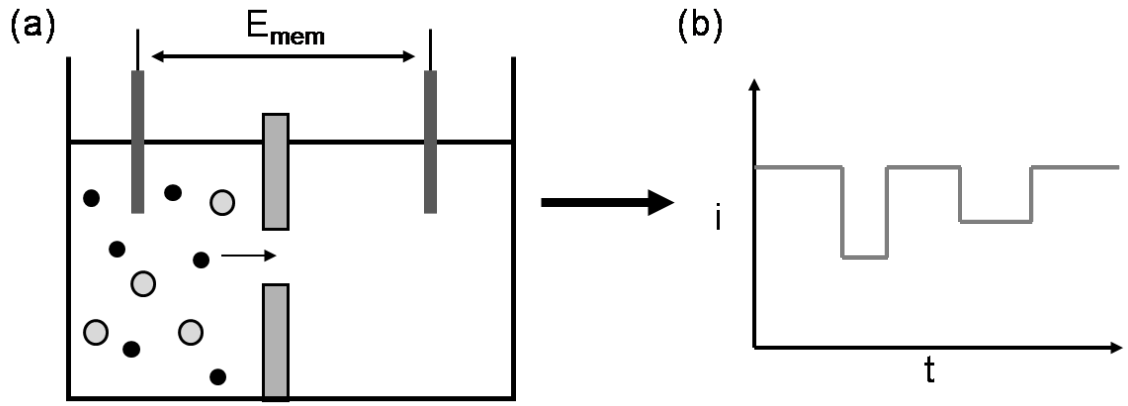

Figure 7-1. Schematic of (a) resistive pulse sensing and (b) an idealized current (i) trace with respect to time (t). The large gray particles produce a deep, short pulse, while the small black particles interact more with the pore walls, giving a shallower, longer pulse.

strength solutions, polyelectrolytes such as DNA and other highly-charged particles introduce more mobile charges into the pore than they displace, resulting in an upward current pulse.[6,7] As a result, pulse magnitude is influenced by ionic strength, particle size, and particle charge. The duration of the pulse gives the residence time of the particle in the aperture, and depending on the chemical characteristics of the pore and the analyte, this value may yield information on analyte interaction with the pore walls, including binding kinetics to a site within the pore,[8,9] the electrophoretic velocity of the analyte,[10,11] or its size.[12] Additionally, the concentration of an analyte in the sample can be determined from the frequency of the pulses.[3] By carefully analyzing these three characteristics of a current pulse – magnitude, duration, and frequency – a relatively large amount of information can be obtained from a simple analytical measurement, and after establishing characteristic signals for each species, a single pore can be used for multianalyte analysis.[13]

Resistive pulse sensors based on biological[14] and synthetic[15] nanopores were first demonstrated over 30 years ago, and both technologies have seen a renewed surge of interest in the past decade as our ability to fabricate structures and probe events at the nanoscale has improved. Unmodified protein pores have been used to characterize sugars,[16] polymers[17,18] and nucleic acid chains,[19] and engineered pores have been used to detect divalent metal ions[8] and small organic molecules.[9] Lipid bilayers containing α-hemolysin pores are particularly well-characterized for stochastic sensing of a variety of analyte molecules.[20,21] Protein pores offer unparalleled reproducibility with respect to pore composition and dimensions, and recent advances have improved the stability of the lipid bilayers surrounding the pores.[22,23] Despite these advantages, however, protein pores

have a limited range of dimensions, surface chemistries, and compatible buffer systems. Artificial pores offer an easily tailored alternative, and increasingly sophisticated fabrication techniques create pores on length scales comparable to those of protein pores. Pores can be formed by track-etching polymer membranes,[24] isolating single carbon nanotubes,[25] micromachining,[26,27] and soft lithography.[28] These systems have been used to characterize a range of analytes including viruses,[15,29] immune complexes,[27] proteins,[30,31] DNA,[7,26,28] and small molecules.[32]

In addition to detection of single molecules, nanopore resistive pulse sensors have been used to detect binding events and macromolecular complexes. A number of antigen-antibody interactions have been studied in this fashion. Both inhibition and sandwich assays have been demonstrated using antigen-modified colloids on PDMS devices.[33,34] Laser-machined glass nanopores have been used to detect large immune complexes[27] and direct binding of an antibody to a virus particle,[29] and smaller nanopores can be used to detect individual protein-antibody complexes, as demonstrated for BSA[12] and β-human chorionic gonadotropin.[35] Additionally, both silicon-based and α-hemolysin protein pores have been used to characterize a variety protein-nucleic acid binding events including interactions of nucleic acid material with restriction enzymes,[36,37] a DNA polymerase fragment,[38] and a viral packaging motor.[39]

In all of these examples, the interacting components were mixed together manually prior to detection at the nanopore. Integration of a nanopore sensing element with a microfluidic system would offer a number of advantages over this method. Addressing the pore with microchannels improves mass transport to the pore, and a microfluidic mixer upstream would facilitate precise, automated on-chip sample processing.

Additionally, a microfluidic architecture around a pore limits the wetted area of the membrane, decreasing membrane capacitance and associated noise.[40] Only a few examples of integrated microchannel-nanopore devices for resistive pulse sensing have been demonstrated,[7,28,34,41] and all of these use the microchannels to improve fluid and electrical access to a planar nanochannel rather than as active device elements. The work presented in this chapter addresses some of the preliminary obstacles to obtaining a functional out-of-plane nanopore sensor on-chip, including device design, trapping and transport at isolated pores, current-based detection of trapping and transport events, and device sealing.

7.2. Methods.

Nanopore device fabrication. Tracked poly(ethylene terephthalate) (PET) membranes with 10^6 tracks/cm^2 were etched and characterized by scanning electron microscopy as described in Section A4. Some membranes were covalently modified with naphthalene groups on the surface using a reaction procedure adapted from the literature.[42] Specific reaction conditions are given in Section A4. The membranes used in these experiments had tip diameters ranging from 120 to 560 nm and base diameters ranging from 1.26 to 3.77 μm. The exact dimensions of the pores used in each experiment are given in the text.

Poly(dimethylsiloxane) (PDMS) microchannels were fabricated from SU-8 masters and characterized as described in Sections A1 and A2. Each 20 μm deep channel was a straight line, 1.4 cm long and 50 μm wide at the ends and narrowed to 10 μm wide for 3 mm at the center. The device was assembled by sandwiching an etched nanopore

membrane between two orthogonal PDMS channels to isolate a single pore, as shown in Figure 7-2. As discussed in Chapter 4, Poisson statistics describe the probability of isolating a single pore at the intersection; however, the reversible nature of the initial seal allowed the upper channel to be adjusted to guarantee a single isolated pore on every device. After assembly the device was reversibly sealed to a PDMS reservoir layer containing 6.2 mm tall, 4 mm i.d. glass reservoirs and filled with buffer using subambient pressure from a house vacuum line. As described in Section 6.2, a picoammeter/voltage source (6487, Keithley Instruments, Inc.) was used to determine the resistance of the channels and the isolated pore.

Sample preparation. pBR322 plasmids, YO-PRO-1, and fluorescent microspheres were obtained from Invitrogen Corp. Plasmids were diluted to a concentration of 1 μg/mL in 10 mM Tris, 1 mM EDTA, 1% w/v BSA buffer and stained with 0.8 μM YO-PRO-1. Microsphere samples were diluted in 10 mM phosphate buffer with 0.1% Triton X-100 to final particle concentrations of 4.4×10^9/mL for 40 nm green fluorescent NeutrAvidin-modified microspheres and 1 to 2×10^8/mL for 100 nm and 200 nm red fluorescent carboxylated microspheres.

Nanopore device operation. Sample was loaded into the lower PDMS channel (reservoir 2 or 4 in Figure 7-2a) and brought to the intersection by hydrostatic flow controlled by adjusting the fluid levels in the reservoirs. The average hydrodynamic velocity of the sample particles was ~40 μm/s. Voltages were applied to the device as described in Section 5.2 and shown schematically in Figure 7-2a. As in previous experiments, reservoirs at each end of the channels were jumpered together to maximize

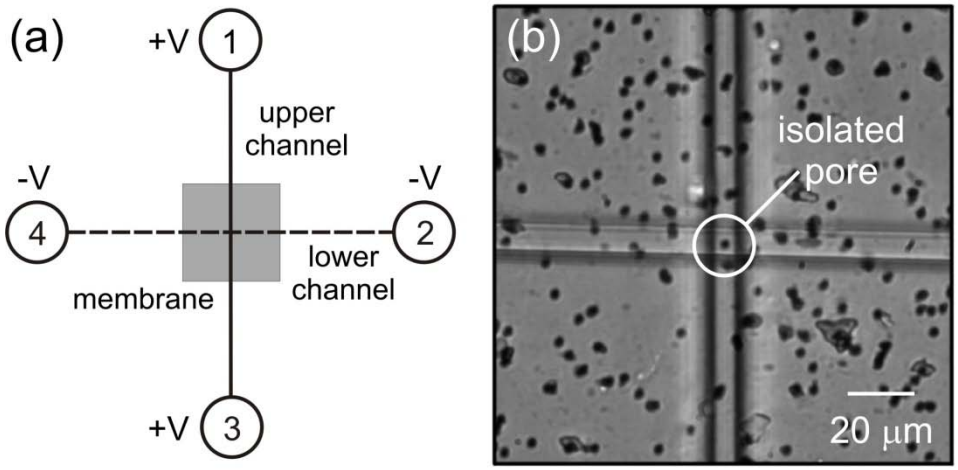

Figure 7-2. (a) Schematic of an integrated nanopore - microchannel device consisting of a track-etch membrane positioned between upper and lower microfluidic channels. The +V and –V labels show where voltages were applied for trapping and sensing. Sample was loaded in reservoir 2 or 4. (b) White light image of the intersection of an assembled device with a single pore isolated at the intersection.

the voltage drop across the pore and to reduce electroosmotic flow through the microchannels.

Optical measurements were made using a CCD camera (9100-13, Hamamatsu Corp.) attached to an inverted microscope (TE-2000U, Nikon, Inc.) equipped for epifluorescence detection with a 60x extra-long working distance objective. Illumination was provided by a metal halide lamp (X-Cite 120, EXFO Life Sciences) and filtered using either a FITC or TRITC filter cube (96320M and 96321M, Nikon, Inc.). Image acquisition and data analysis were performed using IPLab software (BD Biosciences Bioimaging).

Current measurements were obtained using a low-noise current preamplifier (SR 570, Stanford Research Systems), an analog input/output board (PCI-6110, National Instruments Corp.), and LabView software. A single LabView program applied voltages, recorded current measurements into an ASCII file, and triggered the CCD camera to ensure that optical and electrical measurements could be correlated.

7.3. Results and discussion.

Figure 7-3 shows the application of an integrated single nanopore - microchannel device for trapping pBR322 plasmid DNA. The isolated nanopore, shown in Figure 7-3a, was 340 ± 90 nm at the tip and 1.26 ± 0.77 μm at the base. The plasmids were stained with YO-PRO-1, allowing fluorescence detection of discrete DNA molecules, and trapped electrokinetically by applying a 10 V, 1 Hz asymmetric square wave to the device (Figure 7-3b). The fluorescence signal as a function of time (Figure 7-3c) showed a steady increase in trapped material with 1 Hz fluctuations superimposed on the signal

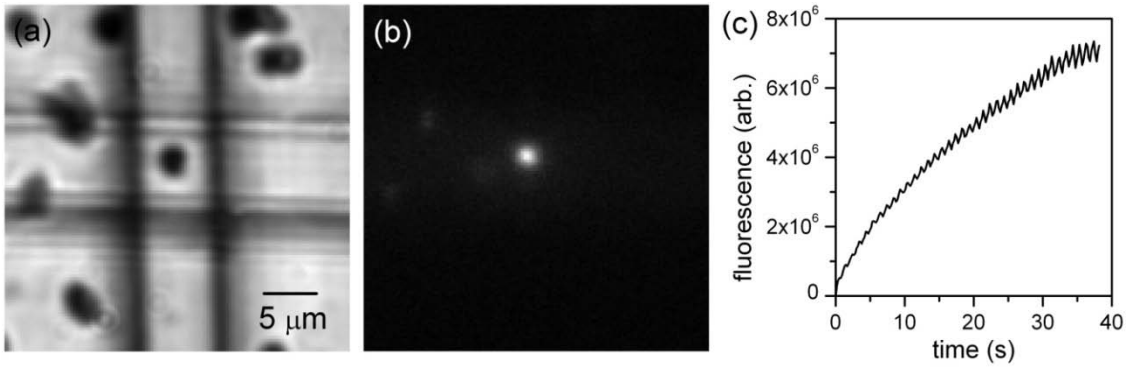

Figure 7-3. (a) White light image of a single isolated pore at the intersection. The pore diameter was 340 ± 90 nm at the tip and 1.26 ± 0.77 μm at the base. (b) Fluorescence image of YO-PRO-1-stained pBR322 plasmids trapped at the nanopore by a 10 V, 1 Hz asymmetric square wave. (c) Fluorescence intensity with time for the region at the intersection. The plot shows a steady increase in fluorescence as plasmids accumulated with regular fluctuations from the 1 Hz trapping waveform superimposed.

due to the trapping waveform. As the trapping waveform cycled, the trapped plasmids were drawn in and out of the focal plane, resulting in a regular variation in intensity. These results demonstrate our ability to manipulate small numbers of biomolecules in the vicinity of the nanopore.

The trapped plasmids in Figure 7-3 were optically detected, but resistive pulse sensing relies on current-based detection of pore blockades. As the next step toward resistive pulse sensing on-chip, we pursued simultaneous optical and electrical detection of trapping events to confirm the origin of the resulting current signals. Figure 7-4 shows simultaneous optical and electrical signals demonstrating the release of a cluster of 40 nm NeutrAvidin-modified microspheres from a 220 ± 40 nm pore. In Figure 7-4a, the fluorescence image shows the trapped particles as a bright spot at the pore. Subsequently, the voltage applied to the device was reversed to eject the cluster of particles, which was absent from the following video frame (Figure 7-4b). The resulting current signal is shown in Figure 7-4c; after the trapped particles were released, the current through the nanopore increased approximately two-fold.

A more sophisticated demonstration of electrical detection of trapping at the nanopore is shown in Figure 7-5. The current trace corresponds to the repeated trapping and release of a single 100 nm carboxylated microsphere using a slowly varying 0.25 Hz, 0 to +2 V sine wave as the trapping waveform. When the applied voltage was high, the particle was electrophoretically trapped at a 120 ± 20 nm pore, resulting in a decrease in current (black arrows). The current did not drop to zero because the trapped particle did not completely occlude the pore. If the particle completely closed the current path, the trapping force would be eliminated. As a result, the trapping position was likely at an

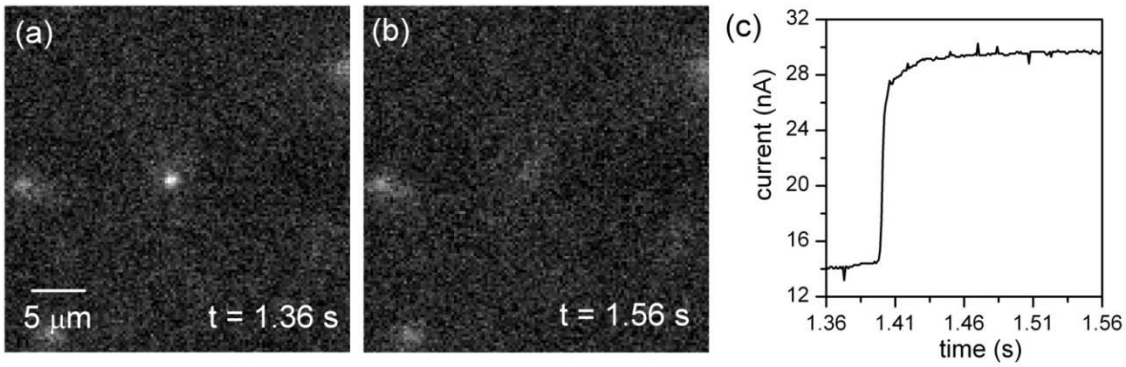

Figure 7-4. Fluorescence images of (a) a cluster of 40 nm NeutrAvidin-modified fluorescent microspheres trapped at an isolated pore and (b) of the same region after the microspheres were removed from the pore by electrokinetic flow. (c) The current trace corresponding to the time period between frames (a) and (b). The current signal increased approximately two-fold when the microspheres were removed from the pore.

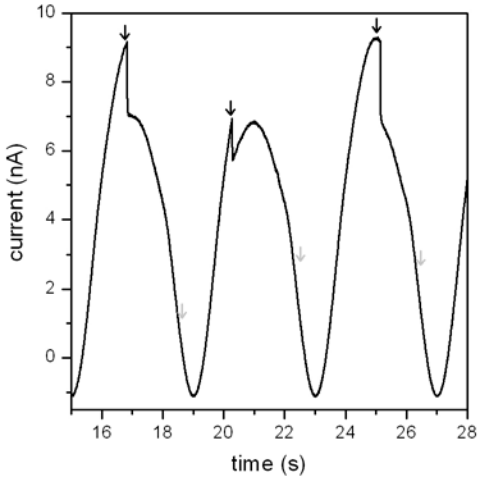

Figure 7-5. Current-time trace showing the signal resulting from repeated trapping and release of a single 100 ± 6 nm carboxylated microsphere at a 120 ± 20 nm nanopore. The trapping waveform applied was a 0.25 Hz sine wave varying from 0 to +2 V. When the waveform was high, the particle was electrophoretically trapped at the nanopore, resulting in a decrease in the current signal (black arrows). When the waveform was low, the particle was released (gray arrows). Release and recapture of the particle with each cycle was confirmed by fluorescence video.

equilibrium point above the nanopore tip, which maintained sufficient electric field strength to hold the particle in place.[43] When the applied waveform was low, the trapped microsphere was able to escape and diffuse away from the pore (gray arrows). The current signal shows no observable change upon particle release because the voltage is low, and by Ohm's law the change in current is proportional to the applied voltage. Instead, particle release and recapture were confirmed by fluorescence video data (not shown).

For many resistive pulse sensing applications, transport of the analyte through the pore, rather than trapping at the pore tip, is desired. To transport analyte particles efficiently through the nanopore, the electric field lines and the resulting flow[44] must lead exclusively through the isolated pore at the intersection. Extraneous electric fields produced by leaks in the device result in electrokinetic traps outside the intersection. This effect was observed in previous work, e.g., Figure 5-4, in which some microspheres trapped outside the intersection and at the microchannel walls, indicating regions of high electric field. These fields must be eliminated for efficient analyte transport through the pore at the intersection. Because the electric field leaks were likely mediated by a thin layer of electrolyte between the device layers, we chemically-modified the membrane to improve device sealing and reduce wetting between layers. PDMS channels are naturally hydrophobic, and hydrophobic compounds are known to partition into PDMS.[45] Therefore, we expected hydrophobic modification of the membrane to improve sealing and to reduce or eliminate wetting between device layers.

A previous report in the literature demonstrated hydrophobic modification of track-etch membranes by covalent attachment of naphthalene residues at reactive carboxylic

acid sites.[42] Modification was confirmed by contact angle measurements and by covalent attachment of a fluorescent residue to the membrane via the same reaction. The fluorescence measurements also demonstrated that the internal pore surfaces, in addition to the outer membrane surface, were modified. When this reaction was applied in our laboratory, the water contact angle increased from 65 - 70˚ after etching to ~80˚ after modification. Additionally, the pore diameters decreased in an unpredictable fashion, in some cases by as much as 500 nm at the base. We attributed the decrease in diameter to solvent-induced shrinkage of the PET membranes by the reaction solvent, dimethylformamide (DMF). PET is known to shrink after exposure to certain solvents, including DMF, due to relaxation of defects in the arrangement of the polymer chains.[46] Shrinkage likely occurred but was overlooked in the original reference because no electron microscopy or gas or current flux studies were performed to evaluate pore size before and after the reaction. We found that the original reaction performed in acetone resulted in a similar change in contact angle with no measurable change in pore diameter ($p = 0.74$, unpaired t-test).

Hydrophobic modification of the nanopore membranes using a reaction run in acetone effectively eliminated electric field leakage between device layers. As a result, efficient transfer of particles through the pore at the intersection was possible. Figure 7-6 shows still images from a fluorescence video of 200 nm carboxylated microspheres being transported through a 560 ± 30 nm hydrophobic pore by a +3 V potential. Particle transport through the pore was confirmed by the 90̊ turn in their flow direction and the Airy disks observed when the particles went through the pore into the upper channel and out of the focal plane. Transfer efficiency was a function of the driving force, i.e., the

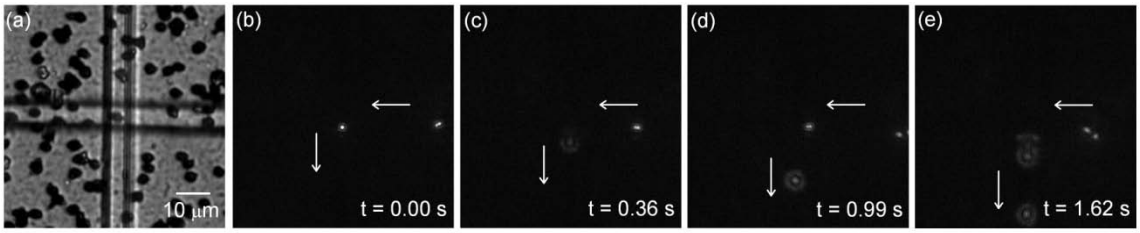

Figure 7-6. (a) White light image of an isolated hydrophobic pore. The nanopore was 560 ± 30 nm at the tip and 3.77 ± 0.20 μm at the base. (b-e) Fluorescence images of two 200 nm diameter microspheres passing through the pore. A +3 V DC signal was applied to the opposite side of the membrane to effect microsphere transport. Arrows indicate the direction of hydrodynamic flow in each channel.

applied potential across the device. Figure 7-7 shows a plot of the number of particles transported through the pore during a 35 s run for applied voltages from 0 to +4 V. For +4 V applied across the device, 100% of the particles passing through the intersection were transferred through the pore, corresponding to an average of 23 particles during every 35 s run.

The final step in development of an on-chip resistive pulse sensor is current-based detection of transport events. By monitoring fluorescence and electrical signals, we validated current pulses corresponding to particle transport through an isolated nanopore. Figure 7-8 shows an example pulse produced by transport of a 40 nm fluorescent microsphere through a conical nanopore with a tip diameter of 120 ± 20 nm, resulting in a ~3% drop in the current through the pore. A potential of +4 V was applied across the device, corresponding to +2.3 V across the pore, to effect transport. Transport of the particle through the pore to the upper channel of the device was confirmed by fluorescence images (not shown). The resulting current pulse lasted ~100 ms and had a signal-to-noise ratio greater than 10.

7.4. Conclusions and future directions.

This chapter has addressed preliminary efforts towards on-chip resistive pulse sensing. We have demonstrated trapping at single pores, efficient transport of particles between device layers, and simultaneous optical and electrical detection of trapping and transport events. A published reaction was adapted to modify etched membranes without changing the pore dimensions. This hydrophobic modification method worked well to resolve sealing issues in devices with pore diameters > 100 nm. Smaller hydrophobic

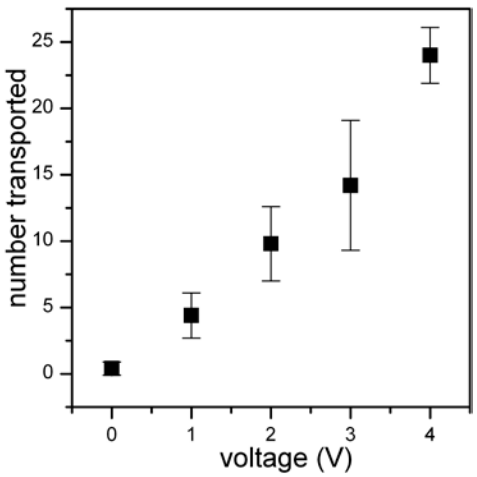

Figure 7-7. The number of microspheres transported through the pore in Figure 7-6 during a 35 s run as a function of applied voltage. The errors bars are ±σ for n = 5 runs at each voltage.

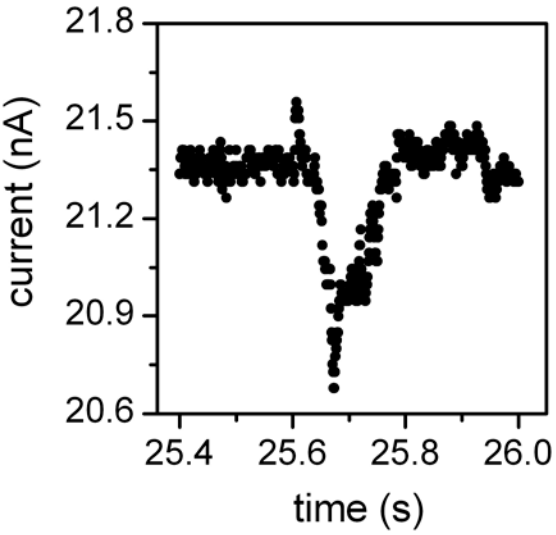

Figure 7-8. Resistive pulse signal arising from transport of a 40 nm NeutrAvidin-modified microsphere through a pore with tip diameter of 120 ± 20 nm. The pulse represents a 3% change in the current through the device, has a signal-to-noise ratio of ~10, and was ~100 ms long. The applied potential was +4 V.

pores, however, did not wet readily without additional surfactant, which often led to wetting between layers. As a result, an alternative sealing strategy is desirable for experiments with smaller pores. Covalent bonding of device layers may be required because this would eliminate wetting between layers and make sealing more robust at higher voltages. Planar devices, such as the one discussed in Chapter 3, are also of interest because they contain only one bonding interface.

This chapter demonstrated fabrication and operation of integrated resistive pulse sensors on-chip, but these devices still need to be optimized and characterized with respect to several analytical metrics, including sensitivity, detection limit, and throughput. These performance measures depend on a variety of experimental parameters, most notably buffer conditions and the pore diameter relative to analyte size. A resistive pulse signal is a function of analyte size and charge, i.e., a given analyte may produce either a positive or a negative pulse depending on whether or not the analyte displaces more charge than it carries. [6,7] As a result, sensing conditions must be chosen carefully to avoid ionic strengths near the transition from positive to negative pulses, where the signal is weakest. For cylindrical pores, detectable signals have been obtained for analyte diameters ranging from 2 – 60% of the pore diameter,[13] but this guideline may not apply for conical pores.

Based on these considerations, further characterization of these systems is required to evaluate their potential and to determine optimum operating conditions. We have chosen to evaluate some of these variables using single-track membranes. These membranes can be etched to leave one isolated pore in the absence of a microfluidic architecture,

allowing rapid characterization of a variety of sensing parameters without the need for further fabrication steps. The results of these studies are discussed in Chapters 8 and 9.

7.5. References.

1. Gribbon, P., Schaertl, S., Wickenden, M., Williams, G., Grimley, R., Stuhmeier, F., Preckel, H., Eggeling, C., Kraemer, J., Everett, J., Keighley, W. W. & Sewing, A. Experience in implementing μHTS - Cutting edge technology meets the real world. *Curr. Drug Disc. Tech.* **2004**, *1*, 27-35.
2. Zander, C., Enderlein, J. & Keller, R. A. (eds.) *Single Molecule Detection in Solution* (Wiley-VCH, Berlin, 2002).
3. Bayley, H. & Martin, C. R. Resistive-pulse sensing -- From microbes to molecules. *Chem. Rev.* **2000**, *100*, 2575-2594.
4. Nakane, J., Akeson, M. & Marziali, A. Evaluation of nanopores as candidates for electronic analyte detection. *Electrophoresis* **2002**, *23*, 2592-2601.
5. Henriquez, R. R., Ito, T., Sun, L. & Crooks, R. M. The resurgence of Coulter counting for analyzing nanoscale objects. *Analyst* **2004**, *129*, 478-482.
6. Chang, H., Kosari, F., Andreadakis, G., Alam, M. A., Vasmatzis, G. & Bashir, R. DNA-mediated fluctuations in ionic current through silicon oxide nanopore channels. *Nano. Lett.* **2004**, *4*, 1551-1556.
7. Fan, R., Karnik, R., Yue, M., Li, D., Majumdar, A. & Yang, P. DNA translocation in inorganic nanotubes. *Nano. Lett.* **2005**, *5*, 1633-1637.
8. Braha, O., Walker, B., Cheley, S., Kasianowicz, J. J., Song, L., Gouaux, J. E. & Bayley, H. Designed protein pores as components for biosensors. *Chem. Biol.* **1997**, *4*, 497-505.
9. Gu, L.-Q., Braha, O., Conlan, S., Cheley, S. & Bayley, H. Stochastic sensing of organic analytes by a pore-forming protein containing a molecular adapter. *Nature* **1999**, *398*, 686-690.
10. Ito, T., Sun, L. & Crooks, R. M. Simultaneous determination of the size and surface charge of individual nanoparticles using a carbon nanotube-based Coulter counter. *Anal. Chem.* **2003**, *75*, 2399-2406.
11. Ito, T., Sun, L., Bevan, M. A. & Crooks, R. M. Comparison of nanoparticle size and electrophoretic mobility measurements using a carbon-nanotube-based Coulter counter, dynamic light scattering, transmission electron microscopy, and phase analysis light scattering. *Langmuir* **2004**, *20*, 6940-6945.
12. Sexton, L. T., Horne, L. P., Sherrill, S. A., Bishop, G. W., Baker, L. A. & Martin, C. R. Resistive-pulse studies of proteins and protein/antibody complexes using a conical nanopore sensor. *J. Am. Chem. Soc.* **2007**, *129*, 13144-13152.
13. Schmidt, J. Stochastic sensors. *J. Mater. Chem.* **2005**, *15*, 831-840.
14. Hladky, S. B. & Haydon, D. A. Discreteness of conductance change in biomolecule lipid membranes in the presence of certain antibiotics. *Nature* **1970**, *225*,

15. DeBlois, R. W., Bean, C. P. & Wesley, R. K. A. Electrokinetic measurements with submicron particles and pores by the resistive pulse technique. *J. Colloid Interf. Sci.* **1977**, *61*, 323-335.
16. Kullman, L., Winterhalter, M. & Bezrukov, S. M. Transport of maltodextrins through maltoporin: a single-channel study. *Biophys. J.* **2002**, *82*, 803-812.
17. Bezrukov, S. M., Vodyanoy, I. & Parsegian, V. A. Counting polymers moving through a single ion channel. *Nature* **1994**, *370*, 279-281.
18. Robertson, J. W. F., Rodrigues, C. G., Stanford, V. M., Rubinson, K. A., Krasilnikov, O. V. & Kasianowicz, J. J. Single-molecule mass spectrometry in solution using a solitary nanopore. *Proc. Natl. Acad. Sci.* **2007**, *104*, 8207-8211.
19. Kasianowicz, J. J., Brandin, E., Branton, D. & Deamer, D. W. Characterization of individual polynucleotide molecules using a membrane channel. *Proc. Natl. Acad. Sci. USA* **1996**, *93*, 13770-13773.
20. Bayley, H., Braha, O. & Gu, L.-Q. Stochastic sensing with protein pores. *Adv. Mater.* **2000**, *12*, 139-142.
21. Bayley, H. & Cremer, P. S. Stochastic sensors inspired by biology. *Nature* **2001**, *413*, 226-230.
22. White, R. J., Ervin, E. N., Yang, T. Y., Chen, X., Daniel, S., Cremer, P. S. & White, H. S. Single ion-channel recordings using glass nanopore membranes. *J. Am. Chem. Soc.* **2007**, *129*, 11766-11775.
23. Heitz, B. A., Xu, J., Hall, H. K., Jr., Aspinwall, C. A. & Saavedra, S. S. Enhanced long-term stability for single ion channel recordings using suspended poly(lipid) bilayers. *J. Am. Chem. Soc.* **2009**doi: 10.1021/ja901442t.
24. Fischer, B. E. & Spohr, R. Production and use of nuclear tracks: imprinting structure on solids. *Rev. Mod. Phys.* **1983**, *55*, 907-948.
25. Ito, T., Sun, L., Henriquez, R. R. & Crooks, R. M. A carbon nanotube-based coulter nanoparticle counter. *Acc. Chem. Res.* **2004**, *37*, 937-945.
26. Li, J., Stein, D., McMullan, C., Branton, D., Aziz, M. J. & Golovchenko, J. A. Ion-beam sculpting at nanometre length scales. *Nature* **2001**, *412*, 166-169.
27. Uram, J. D., Ke, K., Hunt, A. J. & Mayer, M. Label-free affinity assays by rapid detection of immune complexes in submicrometer pores. *Angew. Chem. Int. Ed.* **2006**, *45*, 2281-2285.
28. Saleh, O. A. & Sohn, L. L. An artificial nanopore for molecular sensing. *Nano. Lett.* **2003**, *3*, 37-38.
29. Uram, J. D., Ke, K., Hunt, A. J. & Mayer, M. Submicrometer pore-based characterization and quantification of antibody-virus interactions. *Small* **2006**, *2*, 967-972.
30. Siwy, Z., Trofin, L., HKohli, P., Baker, L. A., Trautmann, C. & Martin, C. R. Protein biosensors based on biofunctionalized conical gold nanotubes. *J. Am. Chem. Soc.* **2005**, *127*, 5000-5001.
31. Fologea, D., Ledden, B., McNabb, D. S. & Li, J. Electrical characterization of protein molecules by a solid-state nanopore. *Appl. Phys. Lett.* **2007**, *91*, 053901.
32. Heins, E. A., Sizy, Z. S., Baker, L. A. & Martin, C. R. Detecting single porphyrin molecules in a conically shaped synthetic nanopore. *Nano. Lett.* **2005**, *5*, 1824-1829.

33. Saleh, O. A. & Sohn, L. L. Direct detection of antibody-antigen binding using an on-chip artificial pore. *Proc. Natl. Acad. Sci.* **2003**, *100*, 820-824.
34. Carbonaro, A. & Sohn, L. L. A resistive-pulse sensor chip for multianalyte immunoassays. *Lab Chip* **2005**, *5*, 1155-1160.
35. Han, A., Creus, M., Schürmann, G., Linder, V., Ward, T. R., de Rooij, N. F. & Staufer, U. Label-free detection of single protein molecules and protein-protein interactions using synthetic nanopores. *Anal. Chem.* **2008**, *80*, 4651-4658.
36. Zhao, Q., Sigalov, G., Dimitrov, V., Dorvel, B., Mirsaidov, U., Sligar, S., Aksimentiev, A. & Timp, G. Detecting SNPs using a synthetic nanopore. *Nano. Lett.* **2007**, *7*, 1680-1685.
37. Hornblower, B., Coombs, A., Whitaker, R. D., Kolomeisky, A., Picone, S. J., Meller, A. & Akeson, M. Single-molecule analysis of DNA-protein complexes using nanopores. *Nat. Methods* **2007**, *4*, 315-317.
38. Benner, S., Chen, R. J. A., Wilson, N. A., Abu-Shumays, R., Hurt, N., Lieberman, K. R., Deamer, D. W., Dunbar, W. B. & Akeson, M. Sequence-specific detection of individual DNA polymerase complexes in real time using a nanopore. *Nat. Nanotechnol.* **2007**, *2*, 718-724.
39. Astier, Y., Kainov, D. E., Bayley, H., Tuma, R. & Howorka, S. Stochastic detection of motor protein-RNA complexes by single-channel current recording. *Chem. Phys. Chem.* **2007**, *8*, 2189-2194.
40. Uram, J. D., Ke, K. & Mayer, M. Noise and bandwidth of current recordings from submicrometer pores and nanopores. *ACS Nano* **2008**, *2*, 857-872.
41. Saleh, O. A. & Sohn, L. L. Quantitative sensing of nanocolloids using a microchip Coulter counter. *Rev. Sci. Instr.* **2001**, *72*, 4449-4451.
42. Maekawa, Y., Suzuki, Y., Maeyama, K., Yonezawa, N. & Yoshida, M. Chemical modification of the internal surfaces of cylindrical pores of submicrometer size in poly(ethylene terephthalate). *Langmuir* **2006**, *22*, 2832-2837.
43. Lee, S., Zhang, Y., White, H. S., Harrell, C. C. & Martin, C. R. Electrophoretic capture and detection of nanoparticles at the opening of a membrane pore using scanning electrochemical microscopy. *Anal. Chem.* **2004**, *76*, 6108-6115.
44. Cummings, E. B., Griffiths, S. K., Nilson, R. H. & Paul, P. H. Conditions for similitude between the fluid velocity and electric field in electroosmotic flow. *Anal. Chem.* **2000**, *72*, 2526-2532.
45. Toepke, M. W. & Beebe, D. J. PDMS absorption of small molecules and consequences in microfluidic applications. *Lab Chip* **2006**, *6*, 1484-1486.
46. Ribnick, A. S., Weigmann, H.-D. & Rebenfeld, L. Interactions of nonaqueous solvents with textile fibers. Part II: Isothermal shrinkage kinetics of a polyester yarn. *Textile Res. J.* **1973**176-182.

CHAPTER 8. Effects of conical nanopore diameter and buffer conditions on ion current rectification.[1]

8.1. Introduction to ion current rectification in nanoconduits.

Successful design and implementation of a nanoscale resistive pulse sensor require a thorough understanding of ion current through nanopores. With this in mind, the following experiments were undertaken to characterize the electrical properties of conical nanopores as functions of pore diameter and buffer conditions. In addition to the particular concern of sensor design, the ion transport and electrical properties of biological and synthetic nanopores are currently of great interest because of the unique phenomena which occur at this scale. Optical and electrical measurements of nanopores have revealed several interesting ion transport properties including ion permselectivity,[2] ion enrichment and depletion,[3-5] and ion current rectification.[6] The physical phenomena underlying these characteristics have been investigated both as matters of fundamental interest and with the aim of utilizing them in various applications, including analyte preconcentration,[4,7,8] resistive pulse sensing, and ion current rectification-based sensing.[9,10]

An early example of ion current rectification by an isolated nanofluidic component was reported over a decade ago using a quartz nanopipette electrode.[11] Since then, rectification has been observed in silicon-based nanochannels,[9] quartz nanopipettes,[12] and track-etch polymer membranes.[13] Track-etch nanopores have been particularly well-studied due to the development of a simple and reliable fabrication method for conical pores.[14] Early work demonstrated ion pumping up a concentration gradient and showed the pH-dependence of rectification,[13,15] and a subsequent study established the internal

surface charge of the nanopore as a critical parameter in controlling rectification.[16] More recently, several research groups have designed nanopores with specific surface modifications[17-21] or electrical-gating[22,23] to enhance or control rectification.

All of these ion current rectifiers meet two fundamental criteria: a characteristic dimension on the nanoscale and a geometric or surface charge asymmetry along the axis of ion current flow. An example of geometric asymmetry is a conical nanopore (Figure 8-1), which has a nanoscale diameter tip and a larger diameter base. For a conical nanopore, the magnitude of the ion current depends on whether counterions, such as the cations in Figure 8-1, travel from the tip to the base or from base to tip. When an electric field is applied such that counterions travel from tip to base, the resulting ion current is higher than when counterion transport is from base to tip. This effect is typically studied using current-voltage (IV) curves, and the degree of rectification (or rectification ratio) is quantified by taking the ratio of the ion current at two applied potentials of equal magnitude but opposite sign.

While the phenomenon of ion current rectification in nanopores is well-known, debate persists concerning its mechanism, and theoretical models to explain ion current rectification have been pursued concurrent with empirical studies. Initially, a ratchet mechanism based on electrokinetic trapping of mobile ions was proposed.[13] This model attributes the low conductance state to a potential well near the tip of the conical pore which traps ions and decreases current flow. The potential well itself arises from the combined effects of the applied field and the local electric field arising from fixed surface charges. When the external electric field is applied in the opposite direction, a potential well is not produced, and a high conductance state is observed. The presence of a

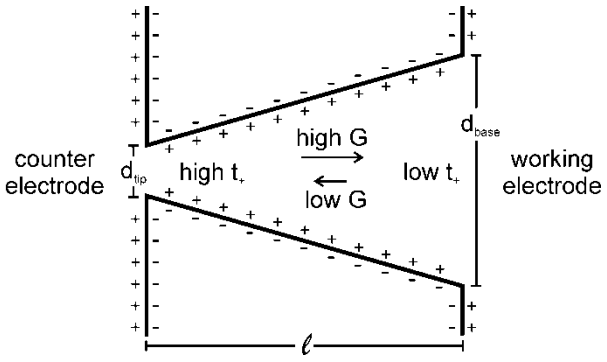

Figure 8-1. Schematic showing the cross-section of a conical nanopore with negative surface charge. Potentials are applied to the working electrode relative to the counter electrode. Arrows show the direction of cation flux in high and low conductance (G) states, and regions of high and lower cation transference number (t_+) are indicated.

potential well has been confirmed in numerical simulations of the local electric field within pores,[24,25] but its magnitude depends strongly on the surface charge and applied potential.[26,27]

An alternative explanation has been proposed which attributes the high conductance state to an increase in ion concentration within the pore. This effect has been predicted by calculations based on a membrane model with narrow pores,[28,29] as well as by numerical analysis of the Poisson Nernst-Planck equations.[24,26,27,30,31] These models predict that rectification arises due to differing transference numbers in and around the tip of the nanopore. At the tip of the pore, a large proportion of the current is carried by counterions. Further into the pore, a smaller percentage of current arises from the surface charge, i.e., the counterion transference number is lower. When counterion transport is from tip to base, as in the high conductance state (G) in Figure 8-1, counterions move from a high transference number region at and near the tip to a lower transference number region within the pore where the diameter is larger and the surface charge contribution is lower. The result is counterion accumulation within the pore, which increases its conductance (high G in Figure 8-1). When the field is applied in the opposite direction, counterions travel from base to tip, from a region of low transference number to a region of higher transference number. Because the solid angle for diffusion within the pore is small, ions transported from base to tip may be removed more quickly than they are replenished, resulting in decreased ion concentration within the pore and consequently lower conductance (low G in Figure 8-1).

Recently, finite element analysis was used to model ion concentrations and ion current for a conical pore with a 100 nm tip and predicted rectification of ion current for KCl

concentrations below 10 mM.[27] This finding is significant since most of the prior experimental and theoretical work was done with much smaller nanoconduits having tip radii comparable to the double layer thickness. In fact, only a few experimental studies have been published showing rectification in an isolated nanoconduit with a diameter ≥ 50 nm, and each of these studies examined only a single pore diameter.[10,12,32] In this work, we systematically examine ion current behavior as a function of tip diameter, buffer conductivity, and buffer pH. Also, included is the first report to our knowledge of ion current rectification by a nanopore with a tip diameter > 200 nm.

8.2. Methods.

Nanopore fabrication. Conical nanopores were etched in tracked poly(ethylene terephthalate) (PET) membranes (GSI, Darmstadt DE) as described in Section A4 and in references 33 and 34. For the 35 and 85 nm tip membranes (see below), a second etch step was performed by filling both sides of the U-cell with 1 M sodium hydroxide and etching until the desired current level, 20 nA and 50 nA, respectively, was reached.[34] The second etch step was 2 h of additional etching after a 40 min first etch step for the 35 nm pore and 65 min of additional etching after a 60 min first etch step for the 85 nm pore. The membranes used were 12 μm thick before etching and approximately 10 μm thick after etching. The base diameters of the pores were obtained from scanning electron microscope (SEM; LEO 1430, Carl Zeiss SMT, Inc., or Quanta 600F, FEI Co.) images of high pore density (10^6 pores/cm^2) membranes etched in an identical fashion. For each single pore membrane, three corresponding multiple pore membranes were etched, and

the base diameters of 20 pores were measured from each. The tip diameter, d_{tip}, of a single pore was calculated using Equation 8.1,

$$d_{tip} = \frac{4\rho\ell}{\pi R_{pore} d_{base}} \tag{8.1}$$

where R_{pore} is the resistance of the pore filled with high ionic strength buffer (10 mM phosphate with 0.5 or 1 M KCl), ρ is the buffer resistivity measured with a conductivity meter (1056, Amber Scientific, Inc.), ℓ is the length of the pore (e.g., 10 μm), and d_{base} is the base diameter from SEM measurements.

Electrical characterization. Current-voltage (IV) behavior was measured for each membrane using the same picoammeter/voltage source and software used for etching. Silver-silver chloride wire electrodes were used to minimize the effects of electrode polarization during the measurements. IV curves were recorded over a potential range of ±1 V with a 0.2 V step every 1.4 s. All voltages are given with respect to the nanopore tip, which was held at ground (counter electrode in Figure 8-1). Unless otherwise noted, IV curves were recorded with five potassium phosphate (J.T. Baker, Inc.) buffers: (1) 1 mM phosphate, (2) 10 mM phosphate, (3) 10 mM phosphate with 0.1 M KCl, (4) 10 mM phosphate with 0.5 M KCl, and (5) 10 mM phosphate with 1 M KCl. For experiments at pH 3.4, the potassium phosphate buffer was replaced with sodium acetate buffer. For each buffer condition, IV curves were recorded in triplicate scanning from -1 V to +1 V and in triplicate from +1 V to -1 V, and all curves were adjusted to zero current at zero volts to remove small offsets between runs. These offsets were from 10's of pA for the smaller pores to the nA range for the 380 nm pores, but were typically < 10% of the maximum current for a given IV curve. The offset currents were variable in sign and

were not eliminated either by adjusting the liquid levels in the U-cell or by allowing the U-cell to equilibrate for 15-30 min between runs. To determine the stability of the rectification behavior, three data sets were taken for each membrane. Between data sets, the membrane was rinsed thoroughly and soaked in water for at least 3 h. The IV curves were then repeated at each buffer concentration. The extent of ion current rectification was evaluated by determining the rectification ratio (the current measured at -1 V divided by the current measured at +1 V).

Four different pore sizes with tip diameters of 11 ± 2 nm, 35 ± 8 nm, 84 ± 7 nm, and 380 ± 30 nm were investigated. These tip diameters corresponded to base diameters of 130 ± 20 nm, 590 ± 140 nm, 600 ± 90 nm, and 1.66 ± 0.13 μm and half cone angles of 0.3˚, 1.5˚, 1.6˚, and 3.7˚, respectively. We refer to the pores by their nominal tip diameters, 10, 35, 85, and 380 nm, and the two 380 nm pores are discussed separately due to their unique rectification behavior.

8.3. Results and discussion.

The current-voltage characteristics of each pore were investigated using phosphate buffers of varying ionic strength. Buffered solutions were used instead of KCl solutions to maintain constant pH and surface charge throughout all experiments. Unbuffered KCl solutions have been used in most previous work because potassium and chloride ions have similar mobilities. To determine whether the different mobilities of the hydrogen phosphate, dihydrogen phosphate, and potassium ions would significantly affect rectification, IV curves for 0.001, 0.01, 0.1, 0.5, and 1 M KCl solutions were taken for the 85 nm pore and compared to IV curves for phosphate buffered solutions. For the

lowest and highest concentrations, the rectification behavior was not statistically different between the buffered and unbuffered solutions. At intermediate ionic strengths, 0.01 to 0.5 M, the rectification ratios observed for the KCl solutions were statistically different (unpaired t-test, $p < 0.05$) from the ratios for phosphate buffered solutions with percent differences ranging from 4% to 23%. However, the KCl solutions did not have consistently higher or lower rectification ratios than the buffered solutions. For the 0.1 and 0.5 M solutions, rectification was higher for unbuffered KCl, and for 0.01 M, rectification was greater for the buffered solutions. Additionally, the overall trends for rectification as a function of ionic strength were the same for unbuffered and buffered solutions. As a result, we chose to use buffered solutions for the studies discussed below.

Figure 8-2a shows IV curves for the 85 nm pore filled with 1 and 10 mM phosphate buffers. Ion current rectification, evident from lower magnitude currents for positive applied potentials than for negative potentials, was observed for both 1 mM and 10 mM phosphate buffers, which correspond to double layer thicknesses of approximately 10 and 3 nm, respectively.[35] This demonstrated experimentally what prior theoretical work has already suggested[27] – while double layer overlap may enhance ion current rectification, overlap is not required. Figure 8-2b shows these curves in addition to those for 10 mM phosphate buffer with 0.1 M and 0.5 M KCl. As expected from previous studies,[30,36] the IV curves became more linear at high ionic strengths. Some previous reports have indicated that pores larger than 15 - 20 nm do not rectify ion current, but these studies did not examine IV curves for low buffer concentrations.[6,13,37] Figure 8-2 demonstrates that larger pores will rectify ion current provided that the ionic strength is sufficiently low, e.g., $\leq$ 10 mM.

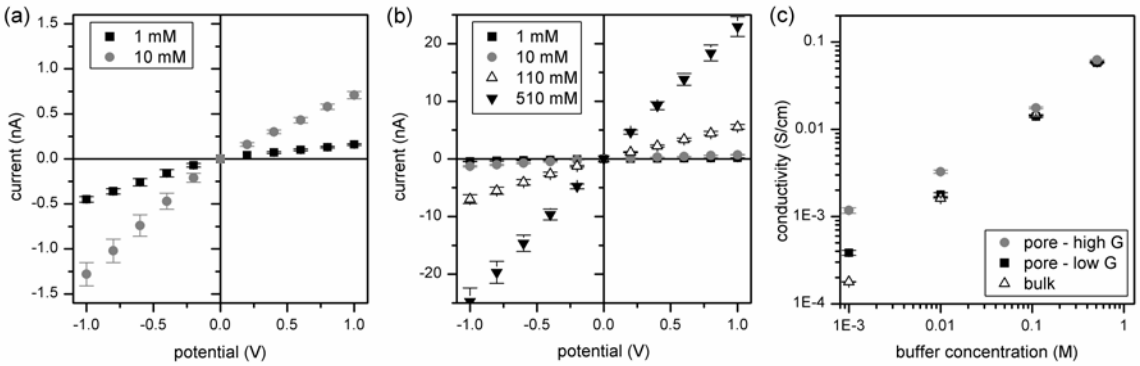

Figure 8-2. (a) Current-voltage (IV) curves showing ion current rectification by the 85 nm pore filled with 1 mM and 10 mM phosphate buffers (pH 6.7). (b) IV curves shown in (a) with curves for 10 mM phosphate with 0.1 M KCl (110 mM) and 0.5 M KCl (510 mM) added. (c) Variation of the pore conductivity in the high and low conductance (G) states with buffer concentration for the 85 nm pore. Error bars in parts (a)-(b) and for the pore conductivities in part (c) are $\pm\sigma$ for n = 18, and errors bars for the bulk buffer conductivities are $\pm\sigma$ for n = 6.

Surface charge played an increasingly important role in pore conductivity as ionic strength decreased. Figure 8-2c shows the pore conductivity as a function of buffer concentration for the 85 nm pore. The bulk conductivity of each buffer is also plotted for comparison. While the bulk buffer conductivity was linear with concentration, the nanopore conductivity was typical of nanoconduits, in which pore conductance becomes less dependent of buffer concentration at low ionic strength.[38,39] For the high conductance state, the pore conductivity exceeded the bulk buffer conductivity for all ionic strengths except 10 mM phosphate with 0.5 M KCl. For the low conductance state, pore conductivity was only higher than the bulk buffer conductivity at 1 mM phosphate. Increased conductivity relative to the buffer conductivity occurred at low ionic strength because of the constant contribution of surface-associated counterions to the current through the pore; as buffer concentration decreased, these ions carried a larger percentage of the total current. Figure 8-2c demonstrates that surface charge effects contributed substantially to current through the 85 nm pore at low ionic strength, and as a result, there was a high transference number for cations in the pore, particularly at the tip.

The IV curves in Figure 8-3 for the 10, 35, and 85 nm pores in 10 mM phosphate buffer with 0.1 M KCl all showed some degree of ion current rectification. The corresponding rectification ratios were 4.8, 2.8, and 1.3, respectively. The rectification ratio decreased with increasing tip diameter, as might be expected based on the relative proportion of current carried by surface charge for each pore. Smaller pores have higher surface area-to-volume ratios, are more cation selective,[40] and have higher cation transference numbers at the tip, resulting in greater rectification.

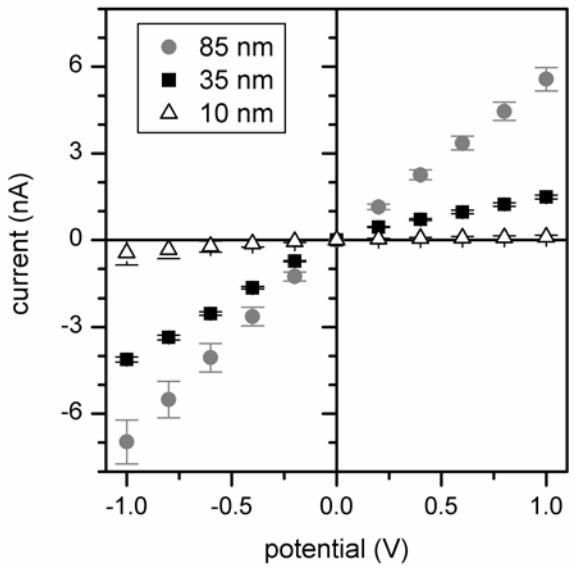

Figure 8-3. IV curves for the 10, 35, and 85 nm pores filled with 10 mM phosphate buffer with 0.1 M KCl (pH 6.7). Error bars are ±σ for n = 18.

For the 10, 35, and 85 nm pores, the rectification ratio decreased with increasing tip diameter at all ionic strengths. Figure 8-4 shows rectification ratios as a function of buffer concentration for these pores. Figure 8-4a shows average values for n = 6 runs from a single data set, and Figure 8-4b shows average values for n = 18 from 3 data sets. Some variation was seen between data sets, especially for smaller pores and lower ionic strengths; however, the overall trends were the same for all data sets collected and the current-voltage behavior of the pores was stable over several days to weeks. For the 10 nm pore, data are shown only for 10 mM phosphate with 0.1 M, 0.5 M, and 1 M KCl because the IV curves were unstable at lower ionic strengths (1 and 10 mM phosphate). At 1 mM phosphate, fewer than 200 K^+ ions are expected to be in the first 800 nm of the 10 nm pore tip, where 50% of the voltage is dropped,[6] and the small number of charge carriers and/or electrothermal effects may have caused the fluctuations observed at low ionic strength.

For the 10 nm pore, the observed rectification ratios increased with decreasing ionic strength and were comparable to those reported in the literature for similarly-sized PET nanopores.[36,37,41] For the 85 nm pore, the rectification ratio also increased with decreasing buffer concentration. As shown in Figure 8-2c, the degree of rectification correlated with an increased contribution of the surface charge to the overall pore conductance. The rectification ratio for the 35 nm pore, however, reached a maximum of 5.7 ± 1.0 (n = 18, Figure 8-4b) for the 10 mM phosphate buffer. Maxima in rectification ratios as a function ionic strength have been observed in previous experiments[25,30,42,43] and predicted by theoretical analyses.[25,27] The maximum occurred near the buffer concentration at which pore conductivity began to differ substantially from the buffer conductivity. Based on the

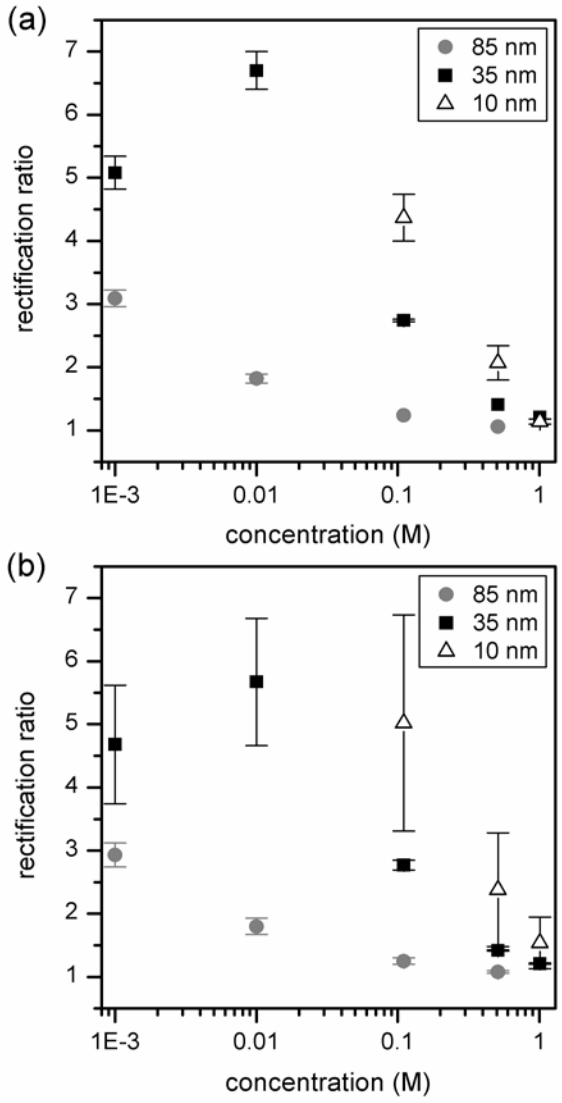

Figure 8-4. Variation of rectification ratio with buffer concentration for the 10, 35, and 85 nm pores. (a) Error bars are ±σ for n = 6. (b) Error bars are ±σ for n = 18. The rectification ratio is the current measured at -1 V divided by the current measured at +1 V.

high conductance state data, the conductivity of the 35 nm pore at 10 mM phosphate was nearly 6 times higher than the conductivity of the bulk buffer. In the low conductance state, however, the conductivity of the pore was not significantly different from the buffer conductivity (unpaired t-test, $p = 0.76$). In other words, the high and low conductance states had dramatically different conductivities at 10 mM, resulting in a maximum. In contrast, at 1 mM phosphate, both the high and the low conductance state resulted in pore conductivities much higher than the buffer conductivity. Even in the low conductance state, the conductivity of the pore was dominated by current arising from the surface charge, reducing the observed rectification ratio.

As discussed above and shown previously,[16] surface charge is critical to ion current rectification, and as a result PET nanopores do not rectify at low pH.[13,15] The isoelectric point of PET membranes has been estimated to be ~3.7,[44] and at lower pH values the surface charge on the pore walls is minimized. Figure 8-5a shows IV curves taken for the 85 nm pore filled with 1 mM potassium phosphate (pH 6.7) and 1 mM sodium acetate (pH 3.4) buffers and demonstrates this effect. In phosphate buffer, the walls of the nanopore were negatively charged and a substantial proportion of the ion current was carried by cationic counterions, resulting in rectification. In the acetate buffer (pH 3.4), the surface charge on the nanopore was reduced, and as a result, the nanopore did not rectify ion current. Figure 8-5b shows the rectification ratio as a function of ionic strength for the pH 6.7 and pH 3.4 buffers. As seen previously in Figure 8-4, the 85 nm pore rectified ion current at lower ionic strengths. For the acetate buffers, however, the rectification ratio was approximately 1 and was nearly independent of ionic strength. The slight maximum at 10 mM acetate with 0.1 M KCl was possibly due to residual surface

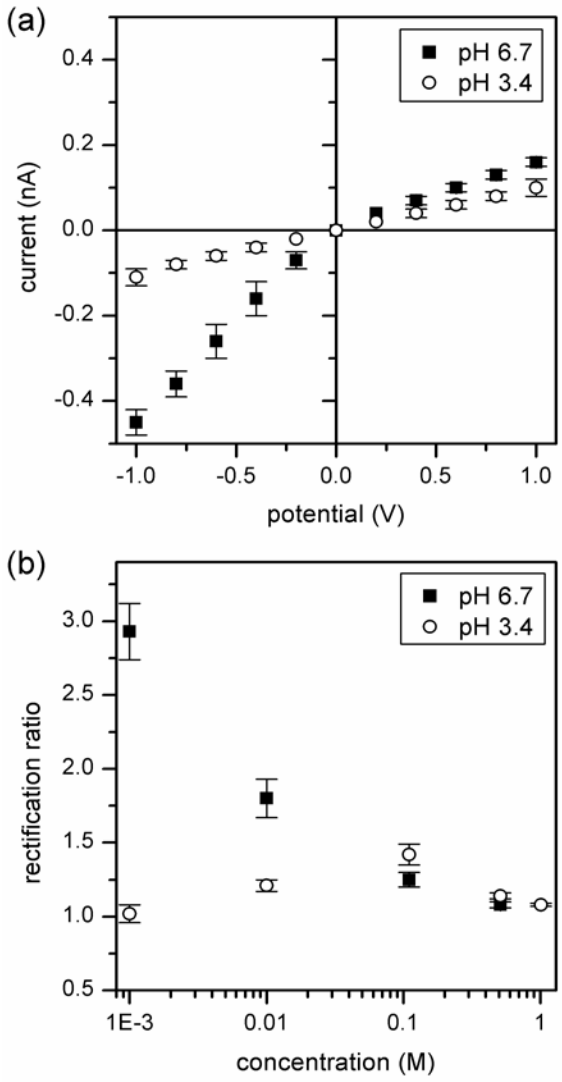

Figure 8-5. (a) IV curves for the 85 nm pore filled with 1 mM potassium phosphate buffer (pH 6.7) and 1 mM sodium acetate buffer (pH 3.4). (b) Variation of the rectification ratio with buffer concentration for phosphate buffer and acetate buffer. Error bars are $\pm\sigma$ for n = 18.

charge. The conductivity of the pore filled with 1 mM acetate was approximately 2 times greater than the bulk acetate buffer conductivity at 1 mM, suggesting that residual surface charge contributed to the pore conductance at lower ionic strengths, albeit to a lesser extent than at pH 6.7.

Based on the trends observed in Figures 8-3 and 8-4, we expected that a relatively large 380 nm pore would not rectify ion current or would rectify only weakly and at very low ionic strength. Figure 8-6a shows the current-voltage behavior of a 380 nm pore filled with 10 mM phosphate with 0.1 M KCl, which initially exhibited nearly diode-like current rectification after etching with rectification ratios as high as 56. After the membrane was stored in water for several days, the rectification ratio decreased substantially and stabilized, as seen in the data set labeled “stable” in Figure 8-6a. Even after stabilizing, however, the pore continued to rectify much more strongly than smaller pores had. Figure 8-6b shows rectification ratio as a function of buffer concentration for the pore in Figure 8-6a. Data are shown for the initial highly rectifying state and for subsequent runs taken after the current-voltage behavior stabilized. The initial data point for 1 mM phosphate is not shown because the IV behavior at this buffer concentration was not repeatable even for immediately successive runs. Comparison to Figure 8-4 indicates that the 380 nm pore rectified more strongly than the 85 nm pore at all ionic strengths.

Figure 8-6c shows the conductivity of the 380 nm pore in the high and low conductance states as well as the bulk conductivity of each buffer. Interestingly, the pore conductivities in the low conductance state after the IV behavior stabilized were approximately equal to the bulk buffer conductivities. The high rectification ratios

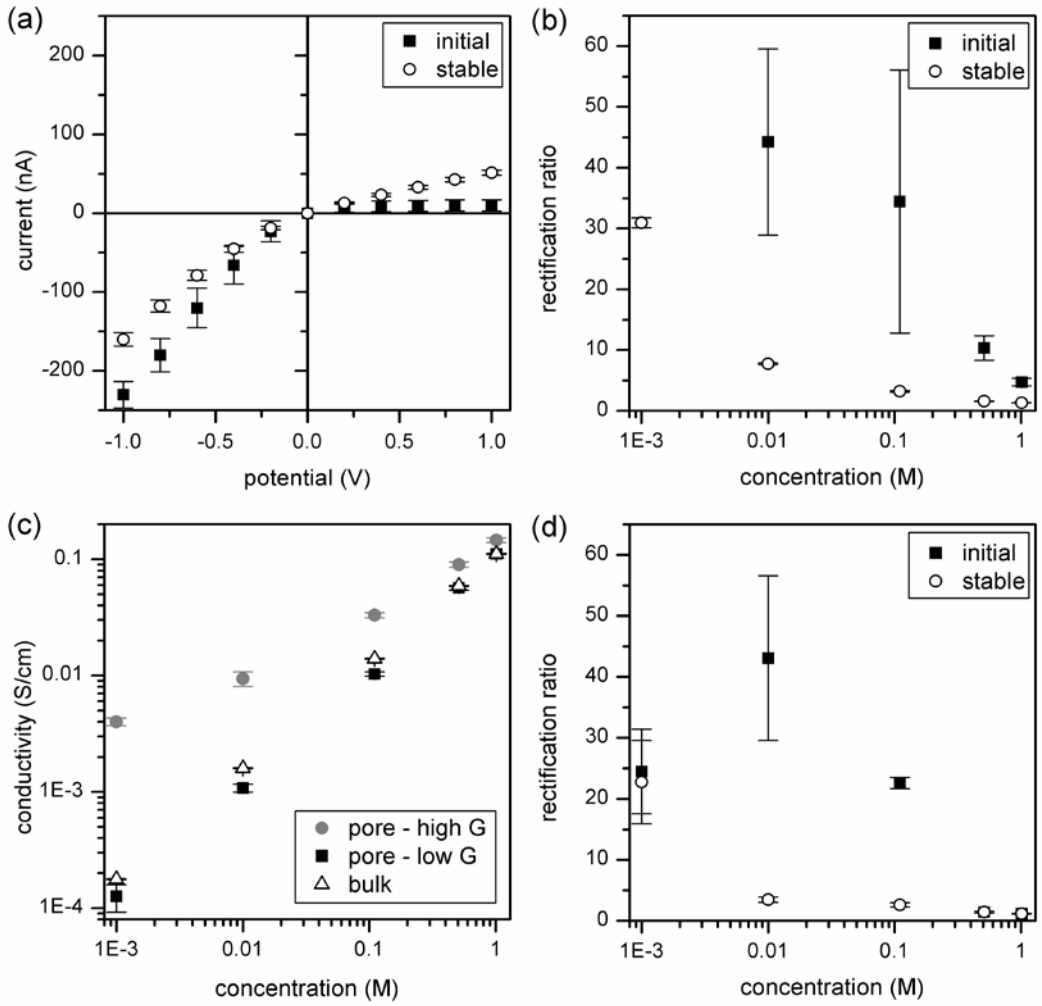

Figure 8-6. (a) IV curves for a 380 nm pore filled with 10 mM phosphate with 0.1 M KCl (pH 6.7) taken initially after etching and after the ion current stabilized. (b) Variation of the rectification ratio with buffer concentration for the pore shown in part (a). (c) Variation of the conductivity with buffer concentration for the high and low conductance (G) states for the pore in part (a) after stabilizing and for the bulk buffer solutions. (d) Variation of the rectification ratio with buffer concentration for a second 380 nm pore, which is similar to the pore from parts (a)-(c). Data points for the initial runs with 10 mM phosphate with 0.5 M KCl and 1 M KCl are obscured by the stable data points because the rectification ratios were almost identical. Error bars for the initial data points are $\pm\sigma$ for n = 6, and error bars for the stable data points are $\pm\sigma$ for n = 18 in (a)-(c) and n = 6 in (d).

observed occurred because the pore conductivities in the high conductance state were 1.3 to 23 times greater than the bulk buffer conductivities. This indicates that rectification resulted from increased conductivity during the high conductance state rather than from a blockade of the pore or ion depletion during the low conductance state. To confirm that this behavior was repeatable for other samples, comparable data were taken for a different pore etched under identical conditions and having the same dimensions. The rectification behavior of the second pore, which was quite similar to the first, is shown for comparison in Figure 8-6d. Two other large pores (> 200 nm) were etched, characterized, and also exhibited rectification ratios > 10 (data not shown).

The larger half cone angle of the 380 nm pores, 3.7˚, compared to 1.6˚ for the 85 nm pore, may account at least partially for the higher rectification ratio. Numerical simulations have suggested that larger cone angles and bullet-like, rather than conical, cross-sections result in increased rectification in small pores ($d_{tip} \leq 10$ nm).[25,26] Higher rectification ratios as the pore cross-section becomes more bullet-like are particularly associated with an increase in current in the high conductance state and minimal change in the low conductance state,[25] an effect that may explain the conductivity trends seen in Figure 8-6c. If the pores were bullet-shaped, the actual tip diameters would be less than 380 nm because Equation 8.1 assumes a conical cross-section. We were unable to locate the tips of the 380 nm pores by scanning electron microscopy; however, three similarly etched multiple pore membranes had tip diameters ranging from 150 to 460 nm with an average tip diameter of 230 ± 74 nm for n = 60. These results indicate that the tip diameters of the single pores were likely much greater than 100 nm, but whether the single pores were bullet-shaped or conical is unclear. Further empirical and theoretical

studies will be required to determine the cross-sectional geometry of these pores and whether larger cone angles, other geometric effects, contributions from electroosmotic flow, or some other mechanism is responsible for the rectification ratios observed. In addition, the change in rectification behavior from initially diode-like behavior to slightly weaker rectification after storage also bears investigation, particularly as the current-voltage characteristics of the smaller pores did not change from their initial behavior under the same conditions (see Figure 8-4b).

8.4. Conclusions and implications for nanopore resistive pulse sensing.

The work presented here has systematically examined the effect of pore diameter and buffer conditions on rectification. Smaller pores typically rectified ion current to a greater extent than larger pores, although double layer overlap and very small tip diameters were not necessary for rectification to occur. The importance of surface charge was evident from pore conductivity measurements and IV curves taken at neutral and low pH. These effects must be considered when designing resistive pulse experiments with conical nanopores. Surface charge exerts such a profound effect on current levels that resistive pulse signals may be easier to interpret if the nanopore surface is chemically modified to render it electrically neutral. Otherwise, non-linear changes in pore resistance with applied potential, ionic strength, and possibly divalent cation concentration[45] must be considered when evaluating the resulting current signal.

The results present here have implications for other areas of applied nanofluidics as well. Practical applications of nanopores, such as sample concentration by ion enrichment, frequently rely on the unique ion transport properties of very small diameter

pores, e.g., sub-20 nm. However, if these effects can be routinely produced in larger pores, e.g., 100 nm or larger, by tuning their geometry and surface charge properties, fabrication protocols could be greatly simplified, and these technologies could be made available to laboratories with limited nanofabrication facilities. Tip diameter is only one of several geometric parameters expected to influence ion current rectification. The cone angle and cross-section of track-etch pores can be controlled by adding organic solvents[46] or surfactants[47] to the etch solutions and by varying the UV treatment of the membrane.[48] Additionally, electron beam lithography can be used to prepare planar nanochannels representative of two-dimensional projections of various nanopore cross-sections. Using these and other fabrication methods, Jacobson laboratory members are further investigating the effects of pore dimensions and geometry on ion transport in asymmetric nanostructures.

8.5. References.

1. This chapter reproduced in part with permission from Kovarik, M. L., Zhou, K., and Jacobson, S. C. Effect of conical nanopore diameter on ion current rectification. *J. Phys. Chem. B* **2009**, in press. Copyright 2009 American Chemical Society.
2. Siwy, Z., Kosinska, I. D., Fulinski, A. & Martin, C. R. Asymmetric diffusion through synthetic nanopores. *Phys. Rev. Lett.* **2005**, *94,* 048102.
3. Pu, Q., Yun, J., Temkin, H. & Liu, S. Ion-enrichment and ion-depletion effect of nanochannel structures. *Nano. Lett.* **2004**, *4,* 1099-1103.
4. Wang, Y.-C., Stevens, A. L. & Han, J. Million-fold preconcentration of proteins and peptides by nanofluidic filter. *Anal. Chem.* **2005**, *77,* 4293-4299.
5. Zhou, K., Kovarik, M. L. & Jacobson, S. C. Surface-charge-induced ion depletion and sample stacking near single nanopores in microfluidic devices. *J. Am. Chem. Soc.* **2008**, *130,* 8614-8616.
6. Siwy, Z. S. Ion-current rectification in nanopores and nanotubes with broken symmetry. *Adv. Funct. Mater.* **2006**, *16,* 735-746.
7. Wang, Y.-C. & Han, J. Pre-binding dynamic range and sensitivity enhancement for immuno-sensors using nanofluidic preconcentrator. *Lab Chip* **2008**, *8,* 392-394.

8. Lee, J. H., Song, Y.-A., Tannenbaum, S. R. & Han, J. Increase of reaction rate and sensitivity of low-abundance enzyme assay using micro/nanofluidic preconcentration chip. *Anal. Chem.* **2008**, *80,* 3198-3204.
9. Karnik, R., Duan, C., Castelino, K., Daiguji, H. & Majumdar, A. Rectification of ionic current in a nanofluidic diode. *Nano. Lett.* **2007**, *7,* 547-551.
10. Wang, J. & Martin, C. R. A new drug-sensing paradigm based on ion-current rectification in a conically shaped nanopore. *Nanomed.* **2008**, *3,* 13-20.
11. Wei, C., Bard, A. J. & Feldberg, S. W. Current rectification at quartz nanopipet electrodes. *Anal. Chem.* **1997**, *69,* 4627-4633.
12. Umehara, S., Pourmand, N., Webb, C. D., Davis, R. W., Yasuda, K. & Karhanek, M. Current rectification with poly-l-lysine-coated quartz nanopipettes. *Nano. Lett.* **2006**, *6,* 2486-2492.
13. Siwy, Z. & Fulinski, A. Fabrication of a synthetic nanopore ion pump. *Phys. Rev. Lett.* **2002**, *89,* 198103.
14. Apel, P. Y., Korchev, Y. E., Siwy, Z., Spohr, R. & Yoshida, M. *Nucl. Instrum. Methods Phys. Rev. Sect. B* **2001**, *184,* 337-346.
15. Siwy, Z., Apel, P., Dobrev, D., Neumann, R., Spohr, R., Trautmann, C. & Voss, K. Ion transport through asymmetric nanopores prepared by ion track etching. *Nucl. Instrum. Methods Phys. Rev. Sect. B* **2003**, *208,* 143-148.
16. Siwy, Z., Heins, E., Harrell, C. C., Kohli, P. & Martin, C. R. Conical-nanotube ion-current rectifiers: The role of surface charge. *J. Am. Chem. Soc.* **2004**, *126,* 10850-10851.
17. Vlassiouk, I. & Siwy, Z. S. Nanofluidic diode. *Nano. Lett.* **2007**, *7,* 552-556.
18. Ali, M., Ramirez, P., Mafé, S., Neumann, R. & Ensinger, W. A pH-tunable nanofluidic diode with a broad range of rectifying properties. *ACS Nano* **2009**, *3,* 603-608.
19. Yameen, B., Ali, M., Neumann, R., Ensinger, W., Knoll, W. & Azzaroni, O. Single conical nanopores displaying pH-tunable rectifying characteristics. Manipulating ionic transport with zwitterionic polymer brushes. *J. Am. Chem. Soc.* **2009**, *131,* 2070-2071.
20. Cheng, L.-J. & Guo, L. J. Ionic current rectification, breakdown, and switching in heterogeneous oxide nanofluidic devices. *ACS Nano* **2009**, *3,* 575-584.
21. He, Y., Gillespie, D., Boda, D., Vlassiouk, I., Eisenberg, R. S. & Siwy, Z. S. Tuning transport properties of nanofluidic devices with local charge inversion. *J. Am. Chem. Soc.* **2009**, *131,* 5194-5202.
22. Kalman, E., Healy, K. & Siwy, Z. S. Tuning ion current rectification in asymmetric nanopores by signal mixing. *Euro. Phys. Lett.* **2007**, *78,* 28002.
23. Kalman, E. B., Sudre, O., Vlassiouk, I. & Siwy, Z. S. Control of ionic transport through gated single conical nanopores. *Anal. Bioanal. Chem.*doi 10.1007/s00216-008-2545-3.
24. Cervera, J., Schiedt, B. & Ramirez, P. A Poisson/Nernst-Planck model for ionic transport through synthetic conical nanopores. *Europhys. Lett.* **2005**, *71,* 35-41.
25. Ramirez, P., Apel, P. Y., Cervera, J. & Mafé, S. Pore structure and function of synthetic nanopores with fixed charges: tip shape and rectification properties. *Nanotechnology* **2008**, *19,* 315707.

26. Liu, Q., Wang, Y., Guo, W., Ji, H., Xue, J. & Ouyang, Q. Asymmetric properties of ion transport in a charged conical nanopore. *Phys. Rev. E* **2007**, *75*, 051201.
27. White, H. S. & Bund, A. Ion current rectification at nanopores in glass membranes. *Langmuir* **2008**, *24*, 2212-2218.
28. Woermann, D. Analysis of non-ohmic electrical current-voltage characteristic of membranes carrying a single track-etched conical pore. *Nucl. Instrum. Methods Phys. Rev. Sect. B* **2002**, *194*, 458-462.
29. Woermann, D. Electrochemical transport properties of a cone-shaped nanopore: high and low electrical conductivity states depending on the sign of an applied electrical potential difference. *Phys. Chem. Chem. Phys.* **2003**, *5*, 1853-1858.
30. Cervera, J., Schiedt, B., Neumann, R., Mafé, S. & Ramirez, P. Ionic conduction, rectification, and selectivity in single conical nanopores. *J. Chem. Phys.* **2006**, *124*, 104706.
31. Qian, S., Joo, S. W., Ai, Y., Cheney, M. A. & Hou, W. Effect of linear surface-charge non-uniformities on the electrokinetic ionic-current rectification in conical nanopores. *J. Colloid Interf. Sci.* **2009**, *329*, 376-383.
32. Jung, J.-Y., Joshi, P., Petrossian, L., Thornton, T. J. & Posner, J. D. Electromigration current rectification in a cylindrical nanopore due to asymmetric concentration polarization. *Anal. Chem.* **2009**, *81*, 3128-2133.
33. Apel, P. Y., Korchev, Y. E., Ziwy, Z., Spohr, R. & Yoshida, M. Diode-like single-ion track membrane prepared by electro-stopping. *Nucl. Instrum. Methods Phys. Rev. Sect. B* **2001**, *184*, 337-346.
34. Wharton, J. E., Jin, P., Sexton, L. T., Horne, L. P., Sherrill, S. A., Mino, W. K. & Martin, C. R. A method for reproducibly preparing synthetic nanopores for resistive-pulse biosensors. *Small* **2007**, *3*, 1424-1430.
35. Bard, A. J. & Faulkner, L. R. *Electrochemical Methods: Fundamentals and Applications* (Wiley, New York, 2000).
36. Siwy, Z., Apel, P., Baur, D., Dobrev, D. D., Korchev, Y. E., Neumann, R., Spohr, R., Trautmann, C. & Voss, K.-O. Preparation of synthetic nanopores with transport properties analogous to biological channels. *Surf. Sci.* **2003**, *532-535*, 1061-1066.
37. Siwy, Z. & Fulinski, A. A nanodevice for rectification and pumping ions. *Am. J. Phys.* **2004**, *72*, 567-574.
38. Stein, D., Kruithof, M. & Dekker, C. Surface-charge-governed ion transport in nanofluidic channels. *Phys. Rev. Lett.* **2004**, *93*, 035901.
39. Ho, C., Qiao, R., Heng, J. B., Chatterjee, A., Timp, R. J., Aluru, N. R. & Timp, G. Electrolytic transport through a synthetic nanometer-diameter pore. *Proc. Natl. Acad. Sci.* **2005**, *102*, 10445-10450.
40. Vlassiouk, I., Smirnov, S. & Siwy, Z. Ionic selectivity of single nanochannels. *Nano. Lett.* **2008**, *8*, 1978-1985.
41. Fulinski, A., Kosinska, I. & Siwy, Z. Transport properties of nanopores in electrolyte solutions: the diffusional model and surface currents. *New J. Phys.* **2005**, *7*, 132.
42. Schiedt, B., Healy, K., Morrison, A. P., Neumann, R. & Siwy, Z. Transport of ions and biomolecules through single asymmetric nanopores in polymer films. *Nucl. Instrum. Methods Phys. Rev. Sect. B* **2005**, *236*, 109-116.

43. Guo, W., Xue, J. M., Zhang, W. M., Zou, X. Q. & Wang, Y. G. Electrolytic conduction properties of single conical nanopores. *Rad. Meas.* **2008**, *43*, S623-S626.
44. Ermakova, L. E., Sidorova, M. P. & Bezrukova, M. E. Filtration and electrokinetic characteristics of track membranes. *Coll. J.* **1998**, *60*, 705-712.
45. Siwy, Z. S., Powell, M. R., Kalman, E., Astumian, R. D. & Eisenberg, R. S. Negative incremental resistance induced by calcium in asymmetric nanopores. *Nano. Lett.* **2006**, *6*, 473-477.
46. Guo, W., Xue, J., Wang, L. & Wang, Y. Controllable etching of heavy ion tracks with organic solvent addition in etchant. *Nucl. Instrum. Methods Phys. Rev. Sect. B* **2008**, *266*, 3095-3099.
47. Apel, P. Y., Blonskaya, I. V., Orelovitch, O. L., Root, D., Vutsadakis, V. & Dmitriev, S. N. Effect of nanosized surfactant molecules on the etching of ion tracks: New degrees of freedom in design of pore shape. *Nucl. Instrum. Methods Phys. Rev. Sect. B* **2003**, *209*, 329-334.
48. Apel, P. Y., Blonskaya, I. V., Orelovitch, O. L. & Dmitriev, S. N. Diode-like ion-track asymmetric nanopores: Some alternative methods of fabrication. *Nucl. Instrum. Methods Phys. Rev. Sect. B* **2009**, *267*, 1023-1027.

CHAPTER 9. Resistive pulse studies of viral capsids.

9.1. Introduction to assembly of icosahedral virus capsids.

Assembly of icosahedral virus capsids represents an attractive system for preliminary resistive pulse studies of supramolecular assembly for several reasons. The process of capsid assembly is of interest with respect to both antiviral drug design[1,2] and for use in engineering self-assembling nanostructures.[3-5] Hepatitis B virus (HBV) capsid assembly is a particularly good model for these experiments. Capsids are formed from multiple copies of a single protein subunit that is readily expressed in *E. coli*; requires no covalent modification prior to assembly; and assembles into well-characterized capsids *in vitro* at high ionic strength. Assembly processes favored by high ionic strength are especially well-suited for resistive pulse analyses because high conductivity buffers reduce noise and ion current rectification in nanopore current measurements.

HBV capsid assembly results in a 36 nm diameter icosahedral capsid of triangulation number (T) 4. T=4 capsids are composed of 4 × 60, or 240, copies of the capsid protein subunit. *In vivo*, this subunit is the 17 kDa, 183-mer HBcAg, which exists as a dimer, but *in vitro*, empty capsids readily assemble from dimers of Cp149, a truncated version which lacks the 34 C-terminal amino acids involved in nucleic acid-packaging.[6] The robust nature of Cp149 capsid assembly has permitted numerous kinetic and thermodynamic studies,[6-12] making HBV assembly a paradigm for icosahedral capsid formation.

Thermodynamically, capsid assembly is entropy-driven by hydrophobic contacts between adjacent dimers. Each contact has a relatively weak association energy (-2.9 to -4.4 kcal/mol), but the network of contacts that forms with assembly results in a globally

stable capsid.[8] The individually weak protein-protein interactions maintain robust assembly of dynamic capsids, capable of sampling their environment ("breathing") and releasing their genetic cargo at the opportune time.[8]

Assembly of HBV capsids follows sigmoidal kinetics with stages of virus assembly corresponding to (1) formation of a nucleus from a trimer of dimers and gradual build-up of a steady-state pool of intermediates by single subunit additions,[7,13] (2) rapid increase in the rate of capsid assembly once the intermediate pool is established, (3) attainment of a steady state in which each new nucleus formed corresponds to completion of one capsid, and (4) a plateau reached when the free subunit concentration decreases below the pseudocritical point.[12] Depending on assembly conditions, including subunit concentration, temperature, ionic strength, and pH, complete capsids are typically detectable on a time-scale of seconds, and equilibrium is reached within 24 h.[7,10,11]

Recently, a number of small molecules have been discovered which interfere with HBV assembly.[10,14,15] These small molecules, including a group of heteraryl-dihydropyrimidines (HAPs),[10,15] increase the subunit-subunit association energy and result in faster, stronger capsid assembly. This limits the opportunities for thermodynamic editing of assembly, increases the number of misformed particles, and produces kinetic traps. These effects make HAPs and similarly-functioning molecules interesting as potential antivirals, particularly because capsid assembly – unlike other aspects of the HBV lifecycle – has no known counterpart in cells.[16] Indeed, kinetic effects of HAPs *in vitro* are correlated with decreases in such metrics as the cytoplasmic concentration of viral DNA and number of secreted virions *in vivo*.[10] Analytical methods

for rapid screening of capsid assembly are therefore of interest in the search for promising drug candidates.

Several analytical methods have been used to characterize HBV assembly and misassembly, including size exclusion chromatography, dynamic light scattering, and fluorescence techniques based on the burial and mobility of tryptophan and tyrosine residues[12] and self-quenching of BODIPY labels.[17] These methods have been quite powerful in elucidating the kinetics of HBV assembly; however, all three techniques measure the ensemble average of the sample population's progress toward assembly. Because intermediates exist at very low concentrations, only the dimer and capsid concentrations can be determined by these methods. In contrast, resistive pulse sensing measures single particles individually, and by taking a sufficient number of measurements, detection of low abundance intermediates should be possible. As a result, resistive pulse sensing represents a complementary method to established techniques which may shed light on empirical intermediate concentrations during the course of assembly.

Early work on resistive pulse sensing of sub-micron particles demonstrated detection and sizing of several viruses > 60 nm, including T-even bacteriophages and four type C oncornaviruses.[18,19] Sub-micron conical pores have also been used to detect antibody binding to individual 190 nm *Paramecium bursaria* chlorella viruses in a resistive pulse immunoassay.[20] The goal of the work described here is to develop a resistive pulse method to interrogate capsid assembly on short (seconds to minutes) time scales and on a single particle basis. These experiments are specifically designed to exploit the single

particle resolution of resistive pulse sensing to detect low abundance intermediates that have not been observed experimentally to date.

9.2. Methods.

Membrane and sample preparation. Poly(ethylene terephthalate) (PET) membranes containing a single track were sealed in Parafilm, mounted in glass U-cells, etched using the two-step method described in Section A4, and electrically and optically characterized using the means described in Chapter 8. Results from two pores are given in this chapter: an 84 ± 7 nm pore was used for DNA sample and a 30 ± 7 nm pore for the HBV capsid sample. λ-phage DNA (New England Biolabs, Inc.) was suspended in 10 mM Tris, 1 mM EDTA, 1 M KCl at a final concentration of 5 μg/mL, and empty HBV capsids assembled from Cp 149 dimers ($Cp149_2$) were obtained from the Zlotnick laboratory (Department of Biology, Indiana University) and suspended in 50 mM HEPES, 0.7 M NaCl (pH 7.5) at a concentration of ~10 nM.

Resistive pulse measurements. Current measurements were obtained using a low-noise current preamplifier (SR 570, Stanford Research Systems), an analog input/output board (PCI-6110, National Instruments Corp.), and LabView software. The preamplifier was set to 6 dB low pass filtering at 300 Hz, 1 kHz sampling, and low noise gain with sensitivities of 20 nA/V for the DNA sample and 10 nA/V for the capsid sample. For all systems, background current-time traces were obtained at 0 V and +1 V for the U-cell filled with the appropriate buffer system in the absence of analyte. These data were used to determine a baseline noise level and to confirm that no current pulses were observed prior to sample introduction. QuB software (v. 1.5.0.11)[21] was used for baseline

subtraction by manual selection of baseline nodes, to apply a 200 Hz filter to the current data, and to identify potential sensing events using segmental k-means (SKM) idealization.

9.3. Preliminary data.

Resistive pulse sensing of λ-phage DNA has been demonstrated several times in the literature,[22-24] so we chose it as a model analyte to evaluate our current measurement system. Figure 9-1 shows a current-time trace obtained for a 5 μg/mL sample in 10 mM Tris, 1 mM EDTA, 1 M KCl passing through an 84 nm pore. Approximately 58 events of variable amplitude and duration were observed during the 150 s period shown in Figure 9-1a. Figure 9-1b shows an expanded view demonstrating some of the variation in pulses. This variation was likely due to several different conformations of the 48.5 kbp λ-phage DNA passing through the pore, an effect which has been observed previously.[22] The baseline root mean square (rms) noise was 17 pA after application of a 200 Hz filter (40 pA before filtering), and a typical pulse amplitude was ~150 pA, resulting in an average signal to noise ratio of ~9. While this was sufficient to resolve λ-phage DNA transport through the pore, the bandwidth of the measurement was low, and the noise level was higher than literature values for similar measurements (typically ~2 pA rms).[22,25,26] A number of improvements can be made to reduce the noise in this system, and these are discussed in Section 9.4.

Figure 9-2 shows resistive pulse signals obtained for HBV capsids in 50 mM HEPES, 0.7 M NaCl (pH 7.5) passing through a 30 nm pore. Five long (duration > 1 s) pulses, like the first pulse in Figure 9-2a, were observed during this experiment. Because the

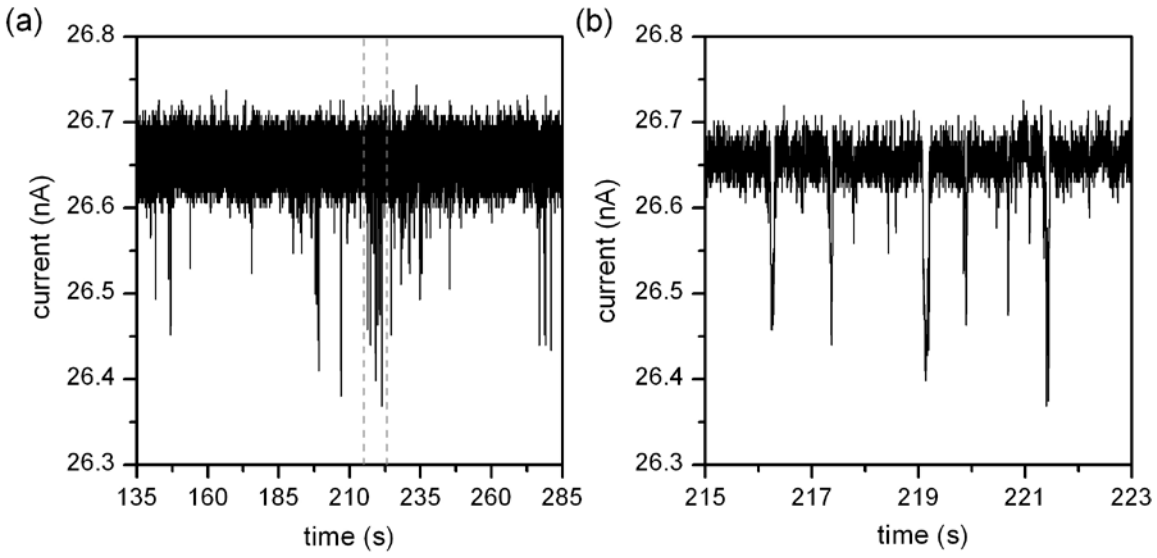

Figure 9-1. Resistive pulse sensing of 5 μg/mL λ-phage DNA in 10 mM Tris, 1 mM EDTA, 1 M KCl using an 85 nm diameter conical nanopore. (a) Current-time trace for a 150 s window with +1 V applied. Approximately 58 events with an average duration of 17 ms were detected in this window. (b) An expanded view of the area bounded by the dashed gray lines in panel (a) which demonstrates the variation in pulse amplitude and duration.

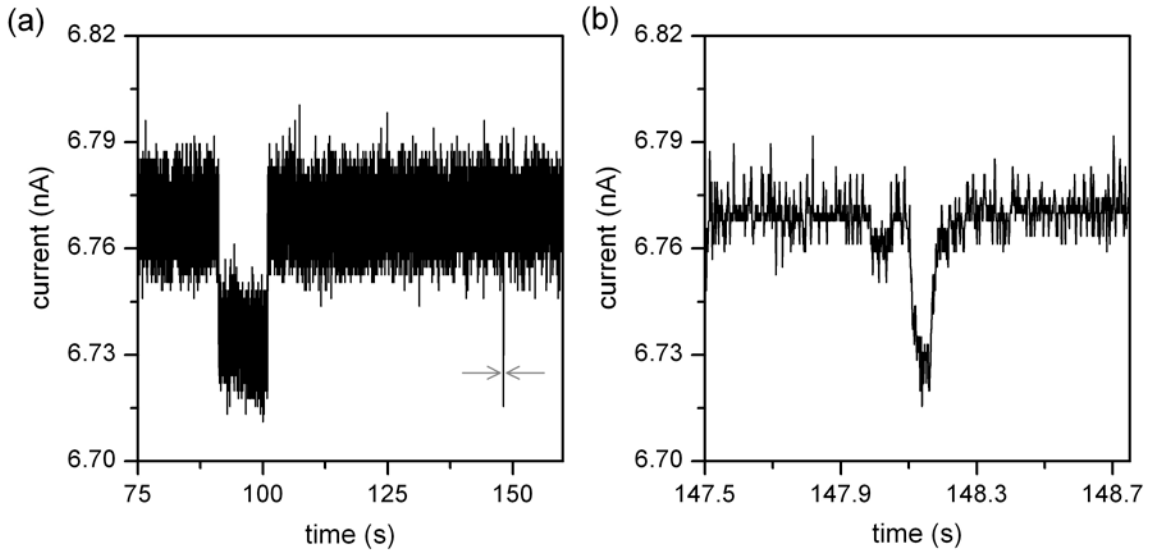

Figure 9-2. Resistive pulse sensing of 10 nM HBV capsids in 50 mM HEPES, 0.7 M NaCl (pH 7.5) using a 30 nm conical nanopore. (a) Current-time trace for an 85 s window with +1 V applied. Two events are visible with durations of 10 s and 100 ms. (b) An expanded view of the 100 ms pulse showing the area bounded in (a) by the two gray arrows.

pore diameter was smaller than the capsid diameter (36 nm), we attribute these prolonged blockades to capsids temporarily stuck in the pore tip. HBV capsids are soft matter, and as mentioned in Section 9.1, held together by individually weak subunit contacts. As a result, we suspect that the capsids were sufficiently flexible to eventually squeeze through the pore tip.

The assumption that long current blockades corresponded to viruses completely occluding the pore tip raises the interesting question of why these events decreased current through the pore by only ~34 pA (0.5%). One potential explanation is that current continued to flow *through the empty capsid*. A unique feature of the HBV lifecycle is that reverse transcription of viral pregenomic RNA to the relaxed circular DNA contained in the mature virion occurs inside the completed capsid, with nucleotides diffusing in and out as needed through ~2 nm diameter openings in the capsid.[16] While the small size of these openings may reduce the mobility of Na^+ and Cl^- ions passing through them, the capsid structure is likely open enough to permit measurable current flow. This hypothesis is readily testable by measuring the current change produced by a nucleocapsid filled with genetic material, which would reduce the cross-section of capsid interior available for current flow and presumably produce a larger change in current. If this is indeed the case, there is the intriguing possibility of determining capsid cargo loading by resistive pulse methods; this would be a particularly useful measurement for research into encapsidation of optical probes, drugs, and other abiotic materials.[4]

Another interesting feature of the current-time trace in Figure 9-2 is the more rapid, 100 ms pulse indicated by the gray arrows in (a) and expanded in (b). As mentioned above, most HBV capsids are T=4; however, both *in vivo* and *in vitro*, a small percentage

of 180-subunit T=3 capsids are also produced.[6] The short pulse in Figure 9-2 may correspond to a 32 nm diameter T=3 capsid,[27] which would have fit more easily through the nanopore than 36 nm T=4 capsids. Unfortunately, the pore was clogged before a large enough number of measurements could be obtained to determine the particle distribution and test this possibility. Future experiments will use a pore larger than the T=4 capsid diameter, allowing a greater number of events to be recorded and an accurate distribution to be determined. While the amplitude of the 100 ms pulse was comparable to that of the longer pulse, this does not necessarily indicate that the two particles are equal in size. In fact, differences in pulse duration, rather than amplitude, have been used to distinguish differently-sized analytes.[28]

9.4. Future directions.

The data shown in Figures 9-1 and 9-2 demonstrate the importance of reducing the rms current noise if assembly studies are to be undertaken. Currently, the noise level observed is due to insufficient electrical shielding and the noise floor of the electronics, and the rms noise levels are well-above those predicted for the bandwidth and pore resistance (40 – 170 MΩ).[26] Performing these measurements in a well-shielded environment with a low-noise amplifier, such as the Axopatch 200B (Molecular Devices Corp.), should substantially decrease the electrical noise. For pore resistances between 30 and 400 MΩ, thermal noise is expected to dominate at low bandwidths (~1 kHz), and dielectric noise and headstage and amplifier noise are expected to dominate at high bandwidths ($\gtrsim$ 10 kHz). [26] Both dielectric noise and headstage and amplifier noise decrease with the capacitance of the dielectric substrate. Literature reports indicate that

decreasing the wetted area of the membrane by painting the surrounding area with poly(dimethylsiloxane) (PDMS) results in decreased noise levels.[29] Published experimental results have shown that 10 pA peak-to-peak noise levels (~2 pA rms) can be obtained for bandwidths of ~1 kHz,[22,25] and a theoretical study of noise in nanopore current recordings indicated lower noise limits of < 1 pA rms at 1 kHz and < 5 pA rms at 10 kHz for 100 MΩ pores.[26] Based on these reports, we conservatively estimate that rms noise of ≤ 5 pA at a bandwidth of 1 kHz and ≤ 10 pA at 10 kHz are achievable.

As discussed in Chapter 7, the signal arising in nanoscale resistive pulse sensing is complex and depends on a number of parameters, including ionic strength, pore and analyte surface charge, and the relative scales of the pore tip and analyte volume. Results presented in Chapter 8 indicate that high ionic strength and conditions favoring neutral pore walls reduce ion current rectification and associated changes in ion concentration within the pore. Further work is required to determine a working range for the ratio of nanopore tip to analyte diameter.

The presence of both T=4 and T=3 capsids in HBV samples will be useful in determining the optimum pore diameter for assembly studies. The relative proportion of the two capsid sizes can be controlled by varying the length of the Cp subunits. Assembly of Cp149 forms 95% T=4 capsids and 5% T=3. Truncation of Cp at residue 140 increases the proportion of T=3 capsids to 15%.[6] T=3 capsids are 32 nm in diameter, rather than 36 nm,[27] corresponding to a 20% decrease in capsid volume and a 25% decrease in total protein volume that should be readily resolved by resistive pulse methods. Demonstration of the ability to discriminate T=3 from T=4 particles will be a useful benchmark in progress toward resistive pulse studies of capsid assembly.

Preliminary assembly studies will be conducted with the U-cell used in these preliminary experiments; the transmembrane potential will be applied and current recorded following manual mixing of the protein subunits and assembly buffer in the U-cell. For initial studies, studying disassembly of capsids using a chaotrope, such as urea, may be more instructive than studying assembly. Disassembly of HBV capsids demonstrates marked hysteresis, resulting in concentrations of intermediates that may be orders of magnitude higher than at equilibrium.[9] This occurs because as dissociation proceeds local concentrations allow reassembly to compete favorably with disassembly, especially for nearly complete intermediates. Consequently, studies of disassembly are likely to provide a relatively intermediate-rich sample on which to hone preliminary measurements.

Integration of nanopore-based resistive pulse sensing with microfluidic architectures will facilitate studies of assembly on short time scales, permit continuous sampling of assembly at discrete time points, and potentially improve throughout for rapid screening of potential drug targets. Currently, some assembly conditions result in such rapid kinetics that complete capsids are formed within the dead time of manual mixing. For example, in 1 M NaCl, $Cp149_2$ assembles into complete capsids in less than the time required to mix and obtain a single data point, i.e., less than 10 s.[11] Microfluidic mixing will permit kinetic measurements of rapid assembly reactions, with an initial data point taken 1 s after mixing readily achievable with a flow rate of 500 μm/s and a distance from mixing tee to nanopore of 0.5 mm. Another advantage of flow-based microfluidic mixing is that the nanopore will continuously sample freshly-mixed reactants, essentially "parking" the reaction at a specific time point determined by the flow rate. Many events

can be sampled at a specific time point until an accurate portrait of the entire population, including low abundance intermediates, has been obtained. By adjusting the flow rate, several discrete time points can be sampled on a single device, resulting in rapid, flexible data acquisition.

Rapid data acquisition is of particular interest for high throughput screening of potential capsid-targeting antivirals. Recently, a fluorescence-based assay was described for rapid screening of capsid-targeting drugs.[17] This technique uses an engineered capsid protein with a C-terminal BODIPY label. Upon assembly, the BODIPY molecules go from a 50 Å separation in the dimer to a 12-20 Å separation inside the completed capsid, resulting in self-quenching. Assembly is therefore correlated with a decrease in fluorescence signal. This fluorescence assay has already been successfully demonstrated in a 96-well format.[17] Interestingly, a microfabricated well-based format has also been pursued for automated patch clamp experiments, in which the bottom of each well contains a conical pore that narrows to a 1 μm diameter.[30] An electrode is located under each well, on the opposite side of the conical pore, for conducting electrophysiological measurements. By decreasing the size of this pore from 1 μm to < 100 nm, the well-based format developed for patch clamp experiments could be used for resistive pulse sensing of discrete particles. Construction of these devices in optically transparent materials would permit complementary ensemble fluorescence measurements to be obtained simultaneously.

9.5. References.

1. Choi, I.-G. & Yu, Y. G. Interaction and assembly of HBV structural proteins: novel target sites of anti-HBV agents. *Infect. Disord. Drug Targets* **2007**, *7*, 251-256.
2. Nassal, M. New insights into HBV replication: new opportunities for improved therapies. *Future Virol.* **2009**, *4*, 55-70.
3. Uchida, M., Klem, M. T., Allen, M., Suci, P., Flenniken, M., Gillitzer, E., Varpness, Z., Liepold, L. O., Young, M. & Douglas, T. Biological containers: protein cages as multifunctional nanoplatforms. *Adv. Mater.* **2007**, *19*, 1025-1042.
4. Aniagyei, S. E., DuFort, C., Kao, C. C. & Dragnea, B. Self-assembly approaches to nanomaterial encapsulation in viral protein cages. *J. Mater. Chem.* **2008**, *18*, 3763-3774.
5. Ueno, T. Functionalization of viral protein assemblies by self-assembly reactions. *J. Mater. Chem.* **2008**, *18*, 3741-3745.
6. Zlotnick, A., Cheng, N., Conway, J. F., Booy, F. P., Steven, A. C., Stahl, S. J. & Wingfield, P. T. Dimorphism of hepatitis B virus capsids is strongly influenced by the C-terminus of the capsid protein. *Biochem.* **1996**, *35*, 7412-7421.
7. Zlotnick, A., Johnson, J. M., Wingfield, P. T., Stahl, S. J. & Endres, D. A theoretical model successfully identifies features of hepatitis B virus capsid assembly. *Biochem.* **1999**, *38*, 14644-14652.
8. Ceres, P. & Zlotnick, A. Weak protein-protein interactions are sufficient to drive assembly of hepatitis B virus capsids. *Biochem.* **2002**, *41*, 11525-11531.
9. Singh, S. & Zlotnick, A. Observed hysteresis of virus capsid disassembly is implicit in kinetic models of assembly. *J. Bio. Chem.* **2003**, *278*, 18249-18255.
10. Bourne, C., Lee, S., Venkataiah, B., Lee, A., Korba, B., Finn, M. G. & Zlotnick, A. Small-molecule effectors of hepatitis B virus capsid assembly give insight into virus life cycle. *J. Virol.* **2008**, *82*, 10262-10270.
11. Bourne, C. R., Katen, S. P., Fulz, M. R., Packianathan, C. & Zlotnick, A. A mutant hepatitis B virus core protein mimics inhibitors of icosahedral capsid self-assembly. *Biochem.* **2009**, *48*, 1736-1742.
12. Katen, S. & Zlotnick, A. The thermodynamics of virus capsid assembly. *Methods Enzymol.* **2009**, *455*, 395-417.
13. Nguyen, H. D., Reddy, V. S. & Brooks III, C. L. Deciphering the kinetic mechanism of spontaneous self-assembly of icosahedral capsids. *Nano. Lett.* **2007**, *7*, 338-344.
14. Stray, S. J. & Zlotnick, A. BAY 41-4109 has multiple effects on hepatitis B virus capsid assembly. *J. Mol. Recognit.* **2006**, *19*, 542-548.
15. Bourne, C. R., Finn, M. G. & Zlotnick, A. Global structural changes in hepatitis B virus capsids induced by the assembly effector HAP1. *J. Virol.* **2006**, *80*, 11055-11061.
16. Steven, A. C., Conway, J. F., Cheng, N., Watts, N. R., Belnap, D. M., Harris, A., Stahl, S. J. & Wingfield, P. T. Structure, assembly, and antigenicity of hepatitis B virus capsid proteins. *Adv. Virus Res.* **2005**, *64*, 125-164.

17. Stray, S. J., Johnson, J. M., Kopek, B. G. & Zlotnick, A. An *in vitro* fluorescence screen to identify antivirals that disrupt hepatitis B capsid assembly. *Nat. Biotech.* **2006**, *24,* 358-362.
18. DeBlois, R. W., Bean, C. P. & Wesley, R. K. A. Electrokinetic measurements with submicron particles and pores by the resistive pulse technique. *J. Colloid Interf. Sci.* **1977**, *61,* 323-335.
19. DeBlois, R. W. & Wesley, R. K. A. Sizes and concentrations of several type C oncornaviruses and bacteriophage T2 by the resistive-pulse technique. *J. Virol.* **1977**, *23,* 227-233.
20. Uram, J. D., Ke, K., Hunt, A. J. & Mayer, M. Submicrometer pore-based characterization and quantification of antibody-virus interactions. *Small* **2006**, *2,* 967-972.
21. Qin, F., Auerbach, A. & Sachs, F. Estimating single-channel kinetic parameters from idealized patch-clamp data containing missed events. *Biophys. J.* **1996**, *70,* 264-280.
22. Saleh, O. A. & Sohn, L. L. An artificial nanopore for molecular sensing. *Nano. Lett.* **2003**, *3,* 37-38.
23. Chen, P., Gu, J., Brandin, E., Kim, Y.-R., Wang, Q. & Branton, D. Probing single DNA molecule transport using fabricated nanopores. *Nano. Lett.* **2004**, *4,* 2293-2298.
24. Fan, R., Karnik, R., Yue, M., Li, D., Majumdar, A. & Yang, P. DNA translocation in inorganic nanotubes. *Nano. Lett.* **2005**, *5,* 1633-1637.
25. Heins, E. A., Sizy, Z. S., Baker, L. A. & Martin, C. R. Detecting single porphyrin molecules in a conically shaped synthetic nanopore. *Nano. Lett.* **2005**, *5,* 1824-1829.
26. Uram, J. D., Ke, K. & Mayer, M. Noise and bandwidth of current recordings from submicrometer pores and nanopores. *ACS Nano* **2008**, *2,* 857-872.
27. Crowther, R. A., Kiselev, N. A., Böttcher, B., Berriman, J. A., Borisova, G. P., Ose, V. & Pumpens, P. Three-dimensional structure of hepatitis B virus core particles determined by electron cryomicroscopy. *Cell* **1994**, *77,* 943-950.
28. Sexton, L. T., Horne, L. P., Sherrill, S. A., Bishop, G. W., Baker, L. A. & Martin, C. R. Resistive-pulse studies of proteins and protein/antibody complexes using a conical nanopore sensor. *J. Am. Chem. Soc.* **2007**, *129,* 13144-13152.
29. Tabard-Cossa, V., Trivedi, D., Wiggin, M., Jetha, N. N. & Marziali, A. Noise analysis and reduction in solid-state nanopores. *Nanotechnology* **2007**, *18,* 305505.
30. Neubert, H.-J. Patch clamping moves to chips. *Anal. Chem.* **2004**, *76,* 327A-330A.

CHAPTER 10. Summary of research contributions and outlook on the field.

10.1. Research contributions.

As the field of nanofluidics matures, fundamental discoveries are being applied in lab-on-a-chip analyses. The unique behavior of matter at the nanoscale lends itself to new functionalities on devices which integrate nanopores or nanochannels. Chapter 1 summarized the general progress in this effort to date, and subsequent chapters have detailed specific contributions of this work to the fabrication, operation, and application of integrated micro- and nanofluidic devices.

While much progress has been made, nanofabrication is still far from routine, especially when device dimensions span several orders of magnitude. Before nanofluidic systems can be applied by non-specialists, nanofabrication techniques must be made simpler and more reliable. Techniques which reduce the number of fabrication steps contribute to this effort. Chapter 2 reported a technique for fabricating three-dimensional structures from two-dimensional photomasks in a single exposure. This method takes advantage of size-dependent transmission properties of apertures in the photomask to control polymer feature dimensions across a wide range of length scales. The resulting SU-8 features had widths from 0.35 to 5.5 μm and heights from 1.1 to 10.8 μm. This technique easily coupled nanoscale to microscale features because they were created in the same photoresist layer with one exposure. By using a single UV exposure step, this method proved less time-intensive than alternative three-dimensional fabrication methods, including multilayer exposure steps[1] and direct write techniques based on

scanning instruments.[2-4] As a result, this UV-exposure technique is more amenable to rapid, large-scale production of nanofluidic devices.

In concert with development of this new fabrication technique, operational aspects of functional nanofluidics have also been investigated. Chapter 3 presented a study of nanochannel fluid dispensing techniques which resulted in injection volumes from 42 aL to 4.1 fL. Two sample dispensing schemes, modified pinched and gated injections, were evaluated on devices with hybrid poly(dimethylsiloxane) and glass nanochannels. These experiments demonstrated the low power requirements and high temporal resolution achieved through miniaturization. Electrokinetic transport was achieved using potentials applied directly from an analog output board without amplification, producing modest electric field strengths in the nanochannels (0.2–2 kV/cm) and enabling rapid dispensing and analysis (10–100 ms). The volumes dispensed are the smallest electrokinetically controlled injections to date and compare favorably with the volumes used for single organelle analyses.[5] Higher modulus materials, e.g., highly crossed-linked PDMS, are improving fidelity in the fabrication of these channels, allowing current members of the Jacobson lab to explore electrokinetic transport in sub-100-nm nanochannels.

In addition to in-plane nanochannels for dispensing, out-of-plane nanofluidics, such as artificial nanopore membranes, were explored for diffusion-based sensing, electrokinetic trapping, and resistive pulse sensing. Track-etch nanopores in polymer membranes are promising for nanoscale analyses due to their rapid, simple, and flexible fabrication.[6] The primary obstacle to incorporation of track-etch membranes in functional devices is the random distribution of pores across the membrane surface. Chapters 4-7 described photolithographic and microfluidic isolation of pores at specific locations to

overcome this issue. For lithographic isolation, UV exposure through a transparency photomask patterned arrays of openings in a SU-8 film to uncover pores in discrete locations. The resulting square patterns ranged in scale from 12 to 75 μm on a side, and the number of isolated pores in each pattern varied from 1 to more than 50 and could be predicted using Poisson statistics. While the SU-8 layer successfully isolated pores in specific locations, the cross-linked SU-8 proved too brittle for use in most applications. The Jacobson laboratory is exploring less brittle materials as alternatives, including another epoxy-based photoresist, 1002-F.[7]

Integrated nanofluidic elements were used to control diffusive and hydrodynamic transport within a device designed for chemotaxis assays and described in Chapter 5. A multilayer microchannel-nanopore device to assay chemotactic behavior was described. Diffusion through a track-etch nanopore membrane integrated in the device created a patch of chemoattractant at the intersection of two microchannels, and changes in cell swimming behavior were monitored in the vicinity of the intersection. Because chemoattractant was dispensed through 10 nm diameter pores, effects of transmembrane pressure were minimized, and the resulting gradient was both stable and reproducible. Additionally, the microfluidic platform permitted microscopic observation of cell swimming and characterization of individual cell trajectories. We applied this system to measure the chemotactic response of an aquatic bacterium, *Caulobacter crescentus*, using xylose as a chemoattractant. For the wild type strain, changes in cell motion indicative of chemotaxis were observed for xylose concentrations ranging from 130 μM to 1.3 M. Furthermore, characterization of individual cell trajectories revealed that a chemotaxis-impaired mutant turns more frequently and exhibits an average run length and duration of

41 μm and 1.4 s, respectively, compared to 68 μm and 2.0 s for the wild type strain. This observation, which was only made possible by tracking individual cells, provided new insight into the chemotaxis pathway in *C. crescentus*. These studies demonstrate the potential for integrated microchannel-nanopore devices in performing rapid, low-sample volume chemotaxis assays with single cell resolution. Devices like these will be useful for investigations of bacterial chemotaxis toward toxic compounds and development of engineered strains for bioremediation.

Chapter 6 reported microfluidic isolation of small ensembles of pores in integrated nanopore-microfluidic devices. In these devices, the unique combination of low pore density, conical nanopores, and microfluidic channels created addressable, localized high-field regions for electrophoretic and dielectrophoretic trapping of particles. Integration of the nanopore membrane with microfluidic channels permitted easy coupling of the electrical potentials and directed transport of the analyte particles, 200 nm and 1 μm polystyrene microspheres and *Caulobacter crescentus* bacteria, to the trapping region. Square waves applied to the device generated electric field strengths up to 1.3×10^5 V/cm at the tips of the nanopores in the microchannel intersection. By varying the applied potentials from ±10 to ±100 V and exploring frequencies from dc to 100 kHz, the relative contributions of electrophoretic and dielectrophoretic forces to the trapping and concentration process were determined. These results suggest that tunable filter elements can be constructed in which the nanoporous elements provide a physical barrier and the applied ac field enhanced selectivity.

In Chapter 7, the electrical properties of single pores isolated at microfluidic intersections were evaluated with a particular focus on on-chip resistive pulse sensing.

Analyte trapping, transport, and sensing were demonstrated at isolated single pores, and a chemical modification method was established for improving device sealing to membranes containing ≥ 100 nm pores. Transport efficiencies of ~100% were achieved for applied potentials of +4 V. Using a 120 nm pore, particles as small as 40 nm were detected with signal-to-noise ratios up to 10. This work provides a foundation for future development of on-chip resistive pulse sensing devices which combine microfluidic sample manipulation with single particle sensing; the long-term goal of this work is to development an integrated microchannel–nanopore device for studies of supramolecular assembly.

Successful design and implementation of such a device require thorough understanding of ion current through nanopores. Conical track-etch pores rectify ion current due to surface charge effects,[8,9] and most previous work concerning this phenomenon had been obtained for small nanopores with diameters comparable to the electrical double layer thickness. Chapter 8 systematically evaluated rectification for nanopores in poly(ethylene terephthalate) membranes with tip diameters of 10, 35, 85, and 380 nm. Current-voltage behavior was determined for buffer concentrations from 1 mM to 1 M and pHs 3.4 and 6.7. In general, ion current rectification increased with decreasing tip diameter, with decreasing ionic strength, and at higher pH. Surface charge contributed to increased pore conductivities compared to bulk buffer conductivities, though double layer overlap was not necessary for rectification to occur. In addition to providing useful information for future experimental design using these nanopores, these experiments led to a number of important fundamental observations. For example, this work confirmed theoretical predictions concerning ion current rectification in large

nanopores in the absence of double layer overlap.[10] Additionally, the 380 nm pores exhibited nearly diode-like current-voltage curves when initially etched and strong rectification after the ion current had stabilized, posing new questions concerning nanopore geometry for empirical and theoretical investigation.

Membranes containing a single isolated pore were used for preliminary resistive pulse sensing experiments with λ-phage DNA and empty hepatitis B virus (HBV) capsids. Experiments with λ-phage DNA demonstrated that while the electronics currently employed for these measurements in our laboratory are capable of detecting analyte transport through a single nanopore, significant improvements in signal-to-noise ratio will be required before assembly studies are undertaken. Published results indicate that an approximately 5-fold reduction in noise beyond our present capabilities should be achievable.[11-13] Preliminary experiments with HBV capsids were also performed. While intact viral particles have been detected by resistive pulse methods in the past,[14-16] studies of supramolecular assembly and protein binding using this technique have been limited to immunoassays. Initial data on resistive pulse sensing of HBV capsids are promising and suggest the intriguing possibility that the resistive pulse signal may depend on capsid contents. Future work will be geared toward reduction of electrical noise; resolution of T=3 and T=4 capsids; determination of the effect of capsid cargo on the resistive pulse signal; detection of intermediates during capsid disassembly and assembly; and integration of the nanopore sensor with microfluidic mixing architecture.

The breadth of the work described here reflects the many possibilities for applied nanofluidics in chemical analysis. Currently, this field is an interesting mix of fundamental studies and analytical applications; as nanotechnology becomes increasingly

available to non-specialists, new and more sophisticated analyses will be pursued. A brief outlook on the prospects for such work and on the future of applied nanofluidics is given below.

10.2. Future outlook for applied nanofluidics.

Specific follow-up experiments and suggestions for future research have been included at the end of each chapter, so a more general outlook on the future of applied nanofluidics is given here. While a number of nanofluidic applications have been presented in the literature and in this dissertation, nanoscale analyses have yet to be proven in terms of clinical or commercial relevancy. Instead, most research in nanofluidics to date has been performed in academic laboratories which specialize in miniaturization. A number of practical advancements must be made before this technology will be accessible and useful to non-specialists.

Continued improvement in the reproducibility, availability, and absolute tolerances of nanofabrication techniques will encourage new laboratories to pursue this work and make routine application of nanofluidic devices viable. Because the behavior of nanofluidic devices depends strongly on device dimensions and surface charge, these variables must be finely controlled to produce consistently functional devices. Currently, no fabrication method has been sufficiently refined to produce uniform nanoscale features quickly and cheaply, but progress in this area is progressing rapidly.[17] Both traditional top-down microfabrication techniques and bottom-up self-assembly methods are being eagerly pursued and improved.[18] Breakthroughs in the field of materials science are aiding in this

endeavor, as methods are developed for precise control of surfaces, nanoscale features, and nanoparticles.

A unified theoretical description of the dominant physical phenomena at the nanoscale will also enormously benefit the field of nanofluidics. A number of observed electrokinetic phenomena are currently poorly understood, making optimal device designs and operating conditions difficult to predict. Additionally, the recent surge of interest in nanotechnology research has led to re-characterization of a number of phenomena in discrete nanochannels which had previously been described in disordered nanoporous gels, membranes, and colloids; for example, see references 19-21, which discuss entropic trapping, ion permselectivity, and electroosmosis of the second kind, respectively. Many important characteristics of nanofluidic devices, such as surface charge, characteristic dimensions, double layer thickness, and others, are closely interrelated. As a result, a comprehensive understanding of the relevant forces and their interrelated effects improves nanofluidic device designs and inspires new applications.

Finally and most importantly, the success of applied nanofluidics depends on identification of appropriate applications. Nanoscale systems are not well-suited for all analyses. The evolution of expectations for microfluidics has recently been described using the Gartner Hype Cycle Model, in which a new technology creates a peak of initial excitement, a precipitous drop in expectations due to early disappointments, an upward slope of enlightenment, and finally a realistic plateau as the actual potential of the technology is realized.[22] Nanofluidics will likely follow the same course. The level of the plateau reached will depend on successful identification of the highest impact applications of nanoscale analyses. The survey of preliminary applications given in

Chapter 1 hints at where nanofluidics may prove most useful. Tunable filtering and sample concentration based on size and surface charge; manipulation of ultra-small volume samples; gel-free macromolecule separations; and single molecule detection are a few areas which take advantage of the unique behavior of matter on the nanoscale and already show promise. Continued investment of time and resources will tell which of these and other applications can best be achieved through nanofluidics.

10.3. References.

1. Madou, M. *Fundamentals of Microfabrication* (CRC Press, Boca Raton, FL, 2002).
2. Wong, W. H. & Pun, E. Y. B. SU8C resist for electron beam lithography. *Proc. SPIE* **2001**, *4345*, 873-880.
3. Reyntjens, S. & Puers, R. A review of focused ion beam applications in microsystem technology. *J. Micromech. Microeng.* **2001**, *11*, 287-300.
4. Sun, H.-B. & Kawata, S. Two-photon photopolymerization and 3D lithographic microfabrication. *Adv. Polym. Sci.* **2004**, *170*, 169-273.
5. Allen, P. B., Doepker, B. R. & Chiu, D. T. High-throughput capillary-electrophoresis analysis of single mitochondria. *Anal. Chem.* **2009**, *81*, 3784-3791.
6. Fischer, B. E. & Spohr, R. Production and use of nuclear tracks: imprinting structure on solids. *Rev. Mod. Phys.* **1983**, *55*, 907-948.
7. Pai, J.-H., Wang, Y., Salazar, G. T., Sims, C. E., Bachman, M., Li, G. P. & Allbritton, N. L. Photoresist with low fluorescence for bioanalytical applications. *Anal. Chem.* **2007**, *79*, 8774-8780.
8. Siwy, Z., Heins, E., Harrell, C. C., Kohli, P. & Martin, C. R. Conical-nanotube ion-current rectifiers: The role of surface charge. *J. Am. Chem. Soc.* **2004**, *126*, 10850-10851.
9. Zhou, K., Kovarik, M. L. & Jacobson, S. C. Surface-charge-induced ion depletion and sample stacking near single nanopores in microfluidic devices. *J. Am. Chem. Soc.* **2008**, *130*, 8614-8616.
10. White, H. S. & Bund, A. Ion current rectification at nanopores in glass membranes. *Langmuir* **2008**, *24*, 2212-2218.
11. Saleh, O. A. & Sohn, L. L. An artificial nanopore for molecular sensing. *Nano. Lett.* **2003**, *3*, 37-38.
12. Heins, E. A., Sizy, Z. S., Baker, L. A. & Martin, C. R. Detecting single porphyrin molecules in a conically shaped synthetic nanopore. *Nano. Lett.* **2005**, *5*, 1824-1829.

13. Uram, J. D., Ke, K. & Mayer, M. Noise and bandwidth of current recordings from submicrometer pores and nanopores. *ACS Nano* **2008**, *2*, 857-872.
14. DeBlois, R. W., Bean, C. P. & Wesley, R. K. A. Electrokinetic measurements with submicron particles and pores by the resistive pulse technique. *J. Colloid Interf. Sci.* **1977**, *61*, 323-335.
15. Uram, J. D., Ke, K., Hunt, A. J. & Mayer, M. Submicrometer pore-based characterization and quantification of antibody-virus interactions. *Small* **2006**, *2*, 967-972.
16. DeBlois, R. W. & Wesley, R. K. A. Sizes and concentrations of several type C oncornaviruses and bacteriophage T2 by the resistive-pulse technique. *J. Virol.* **1977**, *23*, 227-233.
17. Gates, B. D., Xu, Q., Stewart, M., Ryan, D., Willson, C. G. & Whitesides, G. M. New approaches to nanofabrication: molding, printing, and other techniques. *Chem. Rev.* **2005**, *105*, 1171-1196.
18. Mijatovic, D., Eijkel, J. C. T. & van den Berg, A. Technologies for nanofluidic systems: *top-down* vs. *bottom-up* -- a review. *Lab Chip* **2005**, *5*, 492-500.
19. Han, J., Turner, S. W. & Craighead, H. G. Entropic trapping and escape of long DNA molecules at submicron size constriction. *Phys. Rev. Lett.* **1999**, *83*, 1688-1691.
20. Siwy, Z., Kosinska, I. D., Fulinski, A. & Martin, C. R. Asymmetric diffusion through synthetic nanopores. *Phys. Rev. Lett.* **2005**, *94*, 048102.
21. Wang, Y.-C., Stevens, A. L. & Han, J. Million-fold preconcentration of proteins and peptides by nanofluidic filter. *Anal. Chem.* **2005**, *77*, 4293-4299.
22. Mukhopadhyay, R. Microfluidics: On the slope of enlightenment. *Anal. Chem.* **2009**, *81*, 4169-4173.

APPENDIX. Fabrication details.

Details of the fabrication methods used in this research are summarized below.

A1. SU-8 processing.

Glass substrates for SU-8 masters were cleaned by rinsing sequentially with water, acetone, and methanol and dried with a stream of nitrogen. To improve the robustness of SU-8 features, an adhesion layer of AP300 (Silicon Resources, Inc.), an organic titanate, was spin-coated (PWM32-PS-R790; Headway Research, Inc.) onto the clean glass surface at 3000 rpm for 30 s. Within 1 minute of AP300 application, a 10 μm thick SU-8 2010 (MicroChem Corp.) base layer was applied to the surface and processed to further aid adhesion of the patterned SU-8 layer. After the base layer was completely processed, the feature layer of SU-8 was spin-coated onto the surface. Typical spin-coating protocols and the resulting feature heights are given in Table A-1.

After spin-coating, the SU-8 layer was thermally treated on a programmable hotplate (732P Dataplate; Barnstead International) by ramping at 100-300 ºC/h to 65 ºC, holding at 65 ºC for 2 min, ramping at 100-300 ºC/h to 95 ºC, holding at 95 ºC for 3 min, and cooling to ambient temperature. Slower temperature ramps resulted in fewer defects in the SU-8 films. Substrates were then exposed through a photomask to 200 mJ/cm^2 of ultraviolet radiation using a mask aligner (205S; Optical Associates Inc.), unless otherwise noted. A post-exposure bake, identical to the pre-exposure thermal processing, was then performed. Samples were developed for 1-2 min (Nano PG Developer; MicroChem Corp.) to remove unexposed resist and leave the polymerized SU-8 pattern.

Table A-1. Spin-coater protocols for SU-8 2010.

Material	Thickness (μm)	Spread Step	Spin Step 1	Spin Step 2
AP300	---	300 rpm 500 rpm/s during dispense	3000 rpm 1000 rpm/s 30 s	---
25% $^{v}/_{v}$ SU-8 2010 in cyclopentanone	0.4	500 rpm 100 rpm/s 5 s	3000 rpm 300 rpm/s 30 s	---
30% $^{v}/_{v}$ SU-8 2010 in cyclopentanone	3	50 rpm 100 rpm/s 10 s	200 rpm 100 rpm/s 30 s	275 rpm 100 rpm/s 90 s
SU-8 2010	6	500 rpm 100 rpm/s 3 s	2000 rpm 2000 rpm/s 30 s	---
SU-8 2010	10	500 rpm 100 rpm/s 5 s	3000 rpm 300 rpm/s 30 s	---
SU-8 2010	20	---	1000 rpm 1000 rpm/s 45 s	---

The masters were then rinsed with isopropanol and dried in a stream of nitrogen. After developing and drying overnight, the dimensions of the SU-8 masters were determined using a stylus profiler (Dektak 6M, Veeco Instruments, Inc.).

A2. Poly(dimethylsiloxane) processing.

Poly(dimethylsiloxane) (PDMS) channels were formed by soft lithography as described previously.[1] Prepolymer and curing agent were mixed in a 10:1 ratio and degassed under vacuum. Approximately 1.5 mL of the degassed mixture was then poured over the SU-8 master and cured either at 70 ºC for 2 h in a programmable oven (DKN-600; Yamato Scientific America, Inc.) or at 120 ºC for 20 min on a hotplate (732P Dataplate; Barnstead International) for processes requiring complete curing.

For devices which required further assembly, e.g., sealing of a track-etch membrane, the PDMS layer was cured at 70 ºC for 20 min. After partial curing, the PDMS substrates were removed from the masters. A small (2-5 mm on a side) square of membrane was placed over one channel and a tiny drop of uncured PDMS (< 1 μL) was placed at each corner. The top PDMS substrate was positioned over the membrane, and the assembled device was allowed to cure at room temperature overnight. For all PDMS devices, access holes were punched in one layer to provide fluidic access to the channels before device assembly

A3. Glass microchannel fabrication.

Borosilicate glass substrates (B270; Telic Co.) coated with 120 nm of Cr and 530 nm of AZ1500 photoresist were exposed to 200 mJ/cm^2 UV radiation through a transparency

photomask (Photoplot Store). Substrates were then developed for 2 min in Microposit MF-319 developer (Rohm and Haas Co.) and rinsed with water. After development, the channel pattern was transferred to the chromium layer by etching 8 min in Cr Etchant 8002-A (Transene Company, Inc.) and subsequently to the glass layer by etching for 10 min in buffered oxide etchant (Transene Company, Inc.) until the channels were 10 μm deep. A sandblaster (AEC Air Eraser; Paasche Airbrush Co.) was used to drill ~2-mm diameter access holes into the ends of the channels. Following sandblasting, the photoresist layer was removed by rinsing in acetone for 2 min, and the chromium layer was removed by etching for 8 min in Cr Etchant 1020 (Transene Company, Inc.). 4-mm i.d. glass reservoirs were then attached over the sandblasted holes using epoxy (353ND-T; Epoxy Technology, Inc.).

A4. Conical nanopore fabrication and modification.

Tracked poly(ethylene terephthalate) (PET) membranes with either a single track or 10^6 tracks/cm^2 were obtained from GSI, Darmstadt DE. Conical nanopores were etched in the membranes using an etching technique described previously.[2] The tracked membranes were exposed to UV light (UVGL-55; UVP, LLC) overnight prior to etching. UV irradiation of the tracked membranes improves the selectivity of the etchant for the damage tracks over the untracked portion of the membrane and allows even conical pores to be etched.[3] Each membrane was sealed in Parafilm and mounted in a U-cell. One side of the U-cell was filled with etchant, 9 M potassium hydroxide (Mallinckrodt, Inc.), and the other side was filled with a stop solution, composed of 1 M formic acid (J.T. Baker)

and 1 M potassium chloride (Mallinckrodt, Inc.). The membranes were etched for 15 min - 2 h depending on the pore size desired.

For some single track membranes, a previously described two-step etching method was used.[4] The first step was identical to the protocol described above, except that during etching, platinum wire electrodes, a picoammeter/voltage source, and compatible software (6487 and ExceLinx; Keithley Instruments, Inc.) were used to apply a potential of +1 V at the base and to monitor the resulting current. The second etch step was performed with 1 M NaOH on both sides of the membrane and lasted until a desired current level was reached.

To terminate etching, both sides of the U-cell were rinsed with water and filled with stop solution for 30 min to neutralize any remaining base. Membranes were then rinsed and soaked in ultrapure water overnight. The membranes were 12 μm thick before etching and ~10 μm thick after etching. A piece of each multiple pore membrane was sputter-coated with 10 nm of gold (Polaron E5100; Quorum Technologies Ltd.) and characterized using scanning electron microscopy (Leo 1430; Zeiss SMT, Inc.) to obtain the pore dimensions (n = 20 measurements from each side of each membrane).

Some membranes were modified to be more hydrophobic using a procedure adapted from the literature.[5] Prior to modification, the membrane was soaked for 30 min in 1 M NaOH to hydrolyze surface groups. After hydrolysis, the membrane was rinsed with ultrapure water and dried in a vacuum dessicator. The membrane was then suspended in the reaction mixture, which consisted of 50 mM 2-bromomethylnaphthalene and 0.80 mmol potassium fluoride (s) in 40 mL of dimethylformamide (DMF), toluene, or acetone. The reaction proceeded at room temperature with stirring overnight. The membrane was

then removed, rinsed with the reaction solvent and dried in a vacuum dessicator. Before and after modification, the water contact angle was measured using a side-mounted stereoscope (SMZ1000; Nikon Corp.) and a digital camera (MicroPublisher 3.3 RTV; QImaging) to confirm an increase in hydrophobicity. The pore dimensions were also reexamined by scanning electron microscopy. As discussed in Chapter 7, both the tip and base diameters of the nanopores decreased for reactions run in DMF and in toluene. Running the modification reaction in acetone resulted in no significant change in the pore diameter (unpaired t-test, $p = 0.74$), and as a result acetone was the preferred solvent for subsequent modification reactions.

A5. References.

1. Duffy, D. C., McDonald, J. C., Schueller, O. J. A. & Whitesides, G. M. Rapid prototyping of microfluidic systems in poly(dimethylsiloxane). *Anal. Chem.* **1998**, *70*, 4974-4984.
2. Apel, P. Y., Korchev, Y. E., Ziwy, Z., Spohr, R. & Yoshida, M. Diode-like single-ion track membrane prepared by electro-stopping. *Nucl. Instrum. Methods Phys. Rev. Sect. B* **2001**, *184*, 337-346.
3. Fischer, B. E. & Spohr, R. Production and Use of Nuclear Tracks - Imprinting Structure on Solids. *Rev. Mod. Phys.* **1983**, *55*, 907-948.
4. Wharton, J. E., Jin, P., Sexton, L. T., Horne, L. P., Sherrill, S. A., Mino, W. K. & Martin, C. R. A method for reproducibly preparing synthetic nanopores for resistive-pulse biosensors. *Small* **2007**, *3*, 1424-1430.
5. Maekawa, Y., Suzuki, Y., Maeyama, K., Yonezawa, N. & Yoshida, M. Chemical modification of the internal surfaces of cylindrical pores of submicrometer size in poly(ethylene terephthalate). *Langmuir* **2006**, *22*, 2832-2837.

Michelle L. Kovarik

800 N. Smith Rd. Apt 8V, Bloomington, IN 47408
Home: (812) 334-8199 ◘ Cell: (812) 320-0986
Email Address: mkovarik@indiana.edu

EDUCATION

PhD Candidate, Analytical Chemistry, Indiana University, Bloomington, IN, *anticipated Oct 2009.*

Honors Bachelor's of Science, Chemistry, Saint Louis University, St. Louis, MO, May 2004.

RESEARCH EXPERIENCE AND INTERESTS

Graduate Research, Prof. Stephen C. Jacobson, Indiana University
July 2004 – present

- Electron beam lithography for fabrication of 3D micro- and nanoscale features
- Fluid handling on nanofluidic devices
- Electrophoretic and dielectrophoretic trapping and resistive pulse sensing of particles, macromolecules, and cells using track-etch nanopores coupled with microchannels
- Bacterial chemotaxis and transport studies on multilayer microfluidic devices

Undergraduate Research, Profs. Dana M. Spence and R. Scott Martin, Saint Louis University
January 2002 – June 2004

- Investigation of vasodilation mechanisms using electrochemical and chemiluminescence detection
- Fabrication of carbon ink microelectrodes
- Amperometry and capillary electrophoresis on poly(dimethylsiloxane) chips

Research Experience for Undergraduates, Prof. Michael Jay, University of Kentucky
June – July 2003

- Preparation and optimization of aqueous-based nanosuspensions for liquid scintillation counting

TEACHING EXPERIENCE

Tutor, Indiana University Upward Bound Project, Bloomington, IN
June – July 2007

- Algebra tutor during 5-wk on-campus program for at-risk high school students

- Responsibilities: attended class meetings and helped with in-class activities, graded homework assignments, held tutoring sessions Monday-Thursday to meet daily with each student one-on-one

Assistant Instructor, Indiana University, Department of Chemistry, Bloomington, IN
August 2004 – May 2005

- Taught undergraduate discussion sections of introductory general chemistry (C103)
- Responsibilities: introduced new material in discussion and reinforced older material, prepared and graded coursework including homework assignments and quizzes, held regular office hours and review sessions, corresponded with students via email, assisted students with computer-aided learning assignments

Laboratory Assistant, Saint Louis University, Department of Chemistry, St. Louis, MO
August 2001 – May 2004

- Taught undergraduate laboratory sections of general chemistry
- Responsibilities: led pre- and post-laboratory discussions, supervised and assisted with wet chemical, computer-, and paper-based laboratory assignments, held regular office hours and review sessions, graded examinations and lab reports, and corresponded with students via email

Preparatory Laboratory Assistant, Saint Louis University, Department of Physics, St. Louis, MO
August 2002 – May 2003

- Assisted with the general physics laboratory course
- Responsibilities: set up and took down equipment for the general physics labs, assisted the primary teaching assistant in leading the laboratory course

UNIVERSITY AND COMMUNITY SERVICE

Science Fair Judge

- March 7, 2009. Regional Science & Engineering Fair, Bloomington, IN

Volunteer Assistant Instructor, Indiana University, Department of Chemistry, Bloomington, IN
August– November 2007

- Acted as an unpaid assistant instructor for the Service Learning in Chemistry course (G201)
- Accompanied undergraduate students on weekly visits to the Boys' and Girls' Club of Bloomington to run Chemistry Club and perform experiments and demonstrations with the children
- Helped the primary instructor in assigning final grades for undergraduates enrolled in the course

Science Demonstrations Volunteer, Indiana University, Department of Chemistry, Bloomington, IN

- April 4, 2009. Nanoday at the Louisville Science Center. Louisville, KY.
  - Coordinated a demonstration on microcontact printing, including purchase and preparation of supplies, design and printing of two posters, and writing a handout
- February 23, 2009. Women in Science Program Workshop: How to Make a Research Poster. Bloomington, IN.
- November 22, 2008. Brownie Math and Science Day. Bloomington, IN.
- June 16, 2008. Boys' and Girls' Club Camp Rock. Lake Lemon, IN.
- April 24, 2008. Templeton Elementary School Science Night. Bloomington, IN.
- April 17, 2008. Fairview Elementary School Science Night. Bloomington, IN.
- February 8, 2007. Edgewood Elementary School Science Night. Bloomington, IN.

Science Mentor, Saint Louis University, Department of Chemistry, St. Louis, MO
August 2003 – May 2004

- Initiated and coordinated a mentoring program for incoming chemistry majors at SLU
- Introduced a freshman chemistry major to the chemistry department and assisted her in networking with others in the program

October 2002 – February 2003

- Mentored two students from Immaculate Heart High School on their science fair project by assisting them with laboratory experiments in SLU labs and in data analysis and presentation as part of a women in science program

October 2001 – February 2002

- Mentored two students from Gateway Middle School, an inner-city school for gifted children, on their science projects by assisting them with laboratory experiments in SLU labs and in data analysis and presentation

ACADEMIC HONORS, AWARDS AND FELLOWSHIPS

- SPIRE Postdoctoral Fellowship, University of North Carolina-Chapel Hill, 2009.
- Merck Research Laboratories Fellowship in Analytical/Physical Chemistry, 2008.
- 2nd Place Student Poster Presentation in materials science at the Indiana Microscopy Society Spring Meeting, 2008.
- 1st Place Outstanding Research Award in natural science at IU Women in Science Research Conference, 2008.
- Academic Travel Award for LabAutomation 2008 from the Association for Laboratory Automation, 2008.

- Felix Haurowitz Award for outstanding performance up to and including the candidacy exam, IU Chemistry Department, 2007.
- 1st Place Outstanding Research Award in math/technology at IU Women in Science Research Day, 2007.
- Merck Graduate Analytical/Physical Travel Award, 2005.
- Graduate Research Fellowship, National Science Foundation, 2005.
- Women in Science Fellowship, Indiana University, 2004.
- Outstanding Senior Chemistry Student, American Institute of Chemists, 2004.
- Coryell Award for Undergraduate Research, American Chemical Society Division of Nuclear Chemistry and Technology, 2004.
- I. M. Kolthoff Award for Undergraduate Research, American Chemical Society Division of Analytical Chemistry, 2004.
- Saint Louis Rubber Group Scholarship, 2003 and 2004.
- Outstanding Junior Chemistry Student, Saint Louis University, 2003.
- Alpha Sigma Nu (Jesuit Honor Society)
- Phi Beta Kappa

PEER-REVIEWED PUBLICATIONS

11. Kovarik, M.L., Brown, P.J.B., Kysela, D.T., Berne, C., Kinsella, A.C., Brun, Y.V., and Jacobson, S.C. "A microchannel-nanopore device for bacterial chemotaxis assays," in preparation.
10. Kovarik, M.L., Zhou, K., and Jacobson, S.C. "Effect of conical nanopore diameter on ion current rectification," *Journal of Physical Chemistry B*, in press.
9. Kovarik, M.L. and Jacobson, S.C. "Nanofluidics in lab-on-a-chip devices," *Analytical Chemistry*, **2009**, *81*, 7133-7140.
8. Zhou, K., Kovarik, M.L., and Jacobson, S.C. "Surface-charge-induced ion depletion and sample stacking near single nanopores in microfluidic devices," *Journal of the American Chemical Society*, **2008**, *130*, 8614-8616.
7. Kovarik, M.L. and Jacobson, S.C. "Integrated nanopore/microchannel devices for ac electrokinetic trapping of particles," *Analytical Chemistry*, **2008**, *80*, 657-664.
6. Kovarik, M.L. and Jacobson, S.C. "Attoliter-scale dispensing in nanofluidic channels," *Analytical Chemistry*, **2007**, *79*, 1655-1660.
5. Zhu, D., Mu, Z., Mooty, C., Kovarik, M., and Jay, M. "Suspensions of fluor-containing nanoparticles for quantifying β-emitting radionuclides in non-hazardous media," *Journal of Pharmaceutical Innovation*, **2006**, *Sept/Oct*, 76-82.

4. Kovarik, M.L. and Jacobson, S.C., "Fabrication of three-dimensional micro- and nanoscale features with single-exposure photolithography," *Analytical Chemistry*, **2006**, *78*, 5214-5217.

3. Kovarik, M.L., Li, M.W., and Martin, R.S., "Integration of a carbon microelectrode with a fabricated palladium decoupler for use in microchip capillary electrophoresis/electrochemistry," *Electrophoresis*, **2005**, *26*, 202-210.

2. Spence, D.M., Torrence, N.J., Kovarik, M.L., and Martin, R.S., "Amperometric determination of nitric oxide derived from pulmonary artery endothelial cells immobilized in a microchip channel," *Analyst*, **2004**, 995-1000.

1. Kovarik, M.L., Torrence, N.J., Spence, D.M., and Martin, R.S., "Fabrication of carbon microelectrodes with a micromolding technique and their use in microchip-based flow analyses," *Analyst,* **2004**, 400-405.

PROCEEDINGS

2. Kovarik, M.L., Zhou, K., and Jacobson, S.C., "Electrokinetic trapping at single nanopores integrated in microfluidic devices," *Proceedings of the Micro Total Analysis Systems 2008 Conference*; Eds. L.E. Locascio, M. Gaitan, B.M. Paegel, D.J. Ross, W.N. Vreeland; San Diego, CA, October **2008**, 850-852.

1. Kovarik, M.L. and Jacobson, S.C., "Nanopore devices for AC electrokinetic trapping," *Proceedings of the Micro Total Analysis Systems 2007 Conference*; Eds. J.-L. Voivy, P. Tabeling, S. Descroix, L. Malaquin; Paris, France, October **2007**, 1589-1591.

INVITED LECTURES

2. "Nanofluidic devices for bacterial chemotaxis assays," *DePauw University*, Greencastle, IN, October 15, 2009.

1. "Integrated micro- and nanofluidic systems for chemical analysis," *Saint Louis University*, St. Louis, MO, September 19, 2008.

PRESENTATIONS

18. "Fundamental and applied current studies on nanopore-microchannel devices" (Poster), *Indiana University Women in Science Research Conference*, Bloomington, IN, March 6, 2009.

17. "Resistive pulse sensing at single nanopores in microfluidic devices" (Poster), *Microscale Bioseparations*, Boston, MA, February 4, 2009.

16. "Trapping, sensing, and bioassays in multilayer microchannel-membrane devices" (Podium), *Microscale Bioseparations*, Boston, MA, February 2, 2009.

15. "Electrokinetic trapping at single nanopores integrated in microfluidic devices" (Poster), *Midwestern Universities Analytical Chemistry Conference*, Bloomington, IN, November 14, 2008.

14. "Electrokinetic trapping at single nanopores integrated in microfluidic devices" (Poster), *Micro Total Analysis Systems*, San Diego, CA, October 14, 2008.

13. "Particle concentration and sensing at single nanopores in microfluidic devices" (Podium), *Turkey Run Analytical Chemistry Conference*, Marshall, IN, October 4, 2008.

12. "Electrokinetic trapping and transport in individual nanopores in a microfluidic device" (Poster), *HPLC 2008*, Baltimore, MD, May 15, 2008.

11. "Sample concentration and characterization in integrated microchannel/nanopore devices" (Poster), *Indiana Microscopy Society Spring Meeting*, Bloomington, IN, April 18, 2008.

10. "Nanopores for concentrating and analyzing samples" (Poster), *Indiana University Women in Science Research Conference*, Bloomington, IN, March 2, 2008.

9. "An integrated nanopore/microchannel device for electrokinetic trapping" (Podium), *LabAutomation 2008*, Palm Springs, CA, January 29, 2008.

8. "Electrophoretic and dielectrophoretic trapping in an integrated nanopore/microchannel device" (Poster), *Turkey Run Analytical Chemistry Conference*, Marshall, IN, September 14, 2007.

7. "Sample injection methods for nanofluidics" (Poster), *Indiana University Women in Science Research Day*, Bloomington, IN, March 5, 2007.

6. "Nanofluidic devices for attoliter-scale sample handling" (Poster), *Microscale Bioseparations*, Vancouver, BC, January 15, 2007.

5. "Precise fluid control and dispensing in nanochannels" (Poster), *Turkey Run Analytical Chemistry Conference*, Indianapolis, IN, October 6, 2006.

4. "Three-dimensional micro- and nanoscale features produced in a single exposure" (Poster), *Turkey Run Analytical Chemistry Conference*, Marshall, IN, November 4, 2005.

3. "Development and application of a nanosuspension liquid scintillation counting fluid" (Poster), *American Chemical Society National Meeting*, Anaheim, CA, March 28-April 1, 2004.

2. "Development of a biomimetic circulatory resistance vessel using microchip-based flow analysis and a new method of patterning carbon microelectrodes" (Poster), *American Chemical Society National Meeting*, Anaheim, CA, March 28-April 1, 2004.

1. "A novel method for patterning carbon microelectrodes" (Podium), *St. Louis Rubber Group Annual Meeting*, St. Louis, MO, March 2004.